Yang-Hsiung Fan

# Optical Investigation on Hybrids of Nano-Ferromagnets and Diluted Magnetic Semiconductors

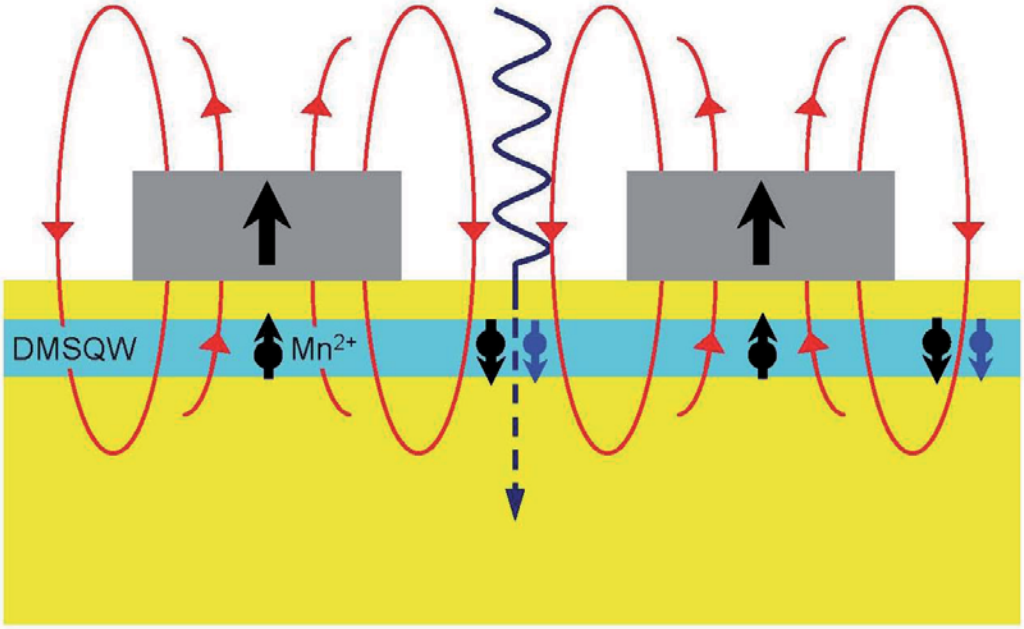


Cuvillier Verlag Göttingen
Internationaler wissenschaftlicher Fachverlag

Dieses Werk ist copyrightgeschützt und darf in keiner Form vervielfältigt werden noch an Dritte weitergegeben werden.
Es gilt nur für den persönlichen Gebrauch.

Dieses Werk ist copyrightgeschützt und darf in keiner Form vervielfältigt werden noch an Dritte weitergegeben werden.
Es gilt nur für den persönlichen Gebrauch.

# Optical Investigation on Hybrids of Nano-Ferromagnets and Diluted Magnetic Semiconductors

DISSERTATION

zur Erlangung des akademischen Grades
doctor rerum naturalium
(Dr. rer. nat.)
im Fach Physik

eingereicht an der
Mathematisch-Naturwissenschaftlichen Fakultät I
Humboldt-Universität zu Berlin

von
Dipl.-Physiker Yang-Hsiung Fan
geboren am 20.06.1968 in Taiwan

Präsident der Humboldt-Universität zu Berlin:
Prof. Dr. Jan-Hendrik Olbertz

Dekan der Mathematisch-Naturwissenschaftlichen Fakultät I:
Prof. Dr. Andreas Herrmann

Gutachter:

1. Prof. Dr. Fritz Henneberger
2. Prof. Dr. Gerd Bacher
3. Prof. Dr. Saskia F. Fischer

eingereicht am: 11.07.2011
Tag der mündlichen Prüfung: 09.01.2012

Dieses Werk ist copyrightgeschützt und darf in keiner Form vervielfältigt werden noch an Dritte weitergegeben werden.
Es gilt nur für den persönlichen Gebrauch.

**Bibliografische Information der Deutschen Nationalbibliothek**
Die Deutsche Nationalbibliothek verzeichnet diese Publikation in der Deutschen Nationalbibliografie; detaillierte bibliografische Daten sind im Internet über http://dnb.d-nb.de abrufbar.

1. Aufl. - Göttingen: Cuvillier, 2012
Zugl.: Berlin, Univ., Diss., 2012

978-3-95404-007-0

© CUVILLIER VERLAG, Göttingen 2012
Nonnenstieg 8, 37075 Göttingen
Telefon: 0551-54724-0
Telefax: 0551-54724-21
www.cuvillier.de

Alle Rechte vorbehalten. Ohne ausdrückliche Genehmigung des Verlages ist es nicht gestattet, das Buch oder Teile daraus auf fotomechanischem Weg (Fotokopie, Mikrokopie) zu vervielfältigen.
1. Auflage, 2012
Gedruckt auf säurefreiem Papier

978-3-95404-007-0

Dieses Werk ist copyrightgeschützt und darf in keiner Form vervielfältigt werden noch an Dritte weitergegeben werden.
Es gilt nur für den persönlichen Gebrauch.

## Zusammenfassung

Der Schwerpunkt dieser Arbeit ist die Untersuchung an Hybriden aus Halbleitern und ferromagnetischen Schichten (FM), um eine Spin-Kontrolle durch das Streufeld des FMs nachzuweisen.

Zur Erzielung einer hohen Empfindlichkeit wird ein Quantengraben (QW) mit verdünnten magnetischen II-VI-Halbleiter (DMSQW) verwendet, wobei der ZnCdMnSe QW das Streufeld in einem festen Abstand vom FM testet. Die s,p-d Austauschwechselwirkung zwischen den magnetischen Mn-Ionen und Bandelektronen bewirkt bei niedriger Temperatur ($T \approx 1,5$ K) den riesigen Zeeman Effekt mit $g$-Faktoren in der Größenordnung von 500. Im typischen DMSQW mit einer Zinkblende-Symmetrie und Druckspannung wird die Austauschwechselwirkung der Exzitonen im Grundzustand durch die p-d Kopplung des Schwerlochs beherrscht. Der Schwerloch hat ein vernachlässigendes magnetisches Moment entlang der QW-Ebene und daher wirkt nur die Streufeldkomponente entlang der Wachstumsrichtung des Quantengraben $z$.

Speziell wurde eine QW-Probe auf transparentem ZnSe-Substrat gezüchtet, um Photolumineszenz (PL) und Faraday-Rotation (FR) messen zu können. Die Mn-Konzentration im QW ist optimiert, um einen maximalen $g$-Faktor zu erhalten. Die Dicke der ZnSe-Deckschicht von 25 nm ist ein empirischer Wert bezüglich einer stabilen Bildung einer Typ-I-Quantengrabenstruktur sowie eines ausreichend starken magnetischen Streufeldes im Quantengraben. Als FM wurde eine Fe/Tb-Dünnschicht mit senkrechter magnetischer Anisotropie (PMA) gewählt. Die remanente out-of-plane Magnetisierung ergibt die erforderliche vertikale Komponente des magnetischen Streufeldes im DMSQW. Strukturierte FMs („wire“ und „anti-dot“-Anordnungen) sind in der Universität Duisburg-Essen durch Elektronenstrahl-Lithographie einer Maske, thermisches Verdampfen der FM-Bestandteile im Ultrahochvakuum und Lift-off-Technik hergestellt. Wire-Anordnungen bestehen aus 1200 nm schlanken Streifen, getrennt durch 800 nm breite Lücken, und Anti-dot-Anordnungen haben 1000 nm $\times$ 1000 nm quadratische Löcher im FM. Die Gesamthöhe des FMs ist kleiner als die lateralen Abmessungen.

Dieses Werk ist copyrightgeschützt und darf in keiner Form vervielfältigt werden noch an Dritte weitergegeben werden.
Es gilt nur für den persönlichen Gebrauch.

Das Verhältnis von FM-Höhe zu Dicke der ZnSe-Deckelschicht lässt die out-of-plane Komponente des magnetischen Streufeldes auf der DMS-Schicht optimieren. Daher erfüllt diese Hybridstruktur die erforderlichen Eigenschaften für die Untersuchung.

Zu Beginn dieser Arbeit werden die mittels Molekularstrahlepitaxie (MBE) gezüchteten ZnCdMnSe/ZnSe DMSQWs auf transparentem Substrat charakterisiert und die Eigenschaften mit denen von DMSQWs auf GaAs-Substrat verglichen. Die Abhängigkeit der riesigen Zeeman-Aufspaltung von Anregungsintensität zeigt, dass die Mn-Spin-Temperatur mit der Gitter-Temperatur mittels Spin-Gitter-Relaxation ausgeglichen wird.

Der FM wirkt als Lochmaske für die optischen Felder. Wenn vom geringen Beitrag der Beugung abgesehen wird, ist der optische Zugang nur für den unbedeckten Bereich gegeben. Für Photolumineszenz (PL)-Messungen wurde ein Anregungsfeld sorgfältig in der Mitte des strukturierten FMs mit einem Durchmesser kleiner als 100 $\mu$m justiert. Eine Photonenenergie von 2,75 eV und eine Anregungsintensität von $1W/cm^2$ garantieren eine vernachlässigbare Spin-Heizung. Die riesige Zeeman-Aufspaltung infolge des FM-Streufeldes wird durch die Verschiebung der PL Maximum in verschiedenen zirkularen Polarisationen aufgenommen. Ein Polarisationsgrad der Exziton-PL von $\mid \rho \mid \approx 30\%$ wurde gefunden. Ein angelegtes Magnetfeld von $B_{ext} \approx 40$ mT ist erforderlich, um das gleiche $\mid \rho \mid$ auf der Referenz DMSQW zu erzeugen.

Die Faraday-Rotation-Technik wird verwendet, um das Streufeld durch den Nachweis der Aufspaltung von Exzitonzuständen direkt zu überprüfen. Die resultierende Differenz der Phasengeschwindigkeit von rechts und links zirkular polarisiertem Licht ergibt die Drehung der Polarisationsebene des einfallenden linear polarisierten Lichts. Ein Drehwinkel $\Theta_{FR} \approx 0,3°$, die $B_{ext} \approx 40$ mT für Referenzprobe entspricht, wurde gefunden. Die Werte für FR sind vollständig in Übereinstimmung mit den erhaltenen Daten aus der Untersuchung für PL-Polarisationsgrad. Das entgegen gesetzte Vorzeichen der Signale sowohl für PL und auch für FR beweisen darauf, dass die FR in der Hybridstruktur tatsächlich durch das umgekehrte Streufeld in den Bereichen zwischen FMs verursacht ist.

Für Nachweis der Spin-Manipulation des FMs und DMSQWs durch einen optischen Impuls wird der Faraday-Rotation-Technik verwendet. Ein einzelner Laserpuls mit einer Photonenenergie von $E_{ex} \approx 2,1$ eV, die kleiner als der DMS Bandlücke ist, wird gewählt, um die Erhitzung des DMSQWs



Dieses Werk ist copyrightgeschützt und darf in keiner Form vervielfältigt werden noch an Dritte weitergegeben werden.
Es gilt nur für den persönlichen Gebrauch.

sowie Substrats zu vermeiden und die Wechselwirkung nur mit der metallischen FM zu sichern. FR-Spektren zeigen das komplette Löschen der durchschnittlichen Magnetisierung vom FM bei einem Laserpuls mit Energiedichte von $16mJ/cm^2$. Nachdem das Magnetfeld wieder auf $B_{ext} = +5$ T angelegt wurde, werden FM-und DMSQW-Magnetisierung vollständig wiederhergestellt. Die Impulse im Nanosekundenbereich bewirken in den vorliegenden Experimenten eine dominierende Entmagnetisierung durch Heizung. Für eine Ummagnetisierung mit optischem Impuls wird ein einzelner Laserpuls mit 16 $mJ/cm^2$ in einem umgekehrten externen Feld $B_{ext} = 0,5$ T verwendet. Der Heizimpuls erhöht die FM-Temperatur und reduziert die Koerzitivfeldstärke $B_c$ auf kleiner als $B_{ext}$. Die vorübergehende Verengung der magnetischen Hysterese durch Laserpuls erklärt die Umkehrung der FM-Magnetisierung unter dem Einfluss eines Laserpulses in einem Biasfeld.

Zum Schluss werden $Zn_{1-x}Mn_xO$-Epitaxieschichten mit $x \leq 0,01$ untersucht, um die s,p-d Austauschintegrale $N_o\alpha$ und $N_o\beta$ festzustellen. Die Daten sind aus der Aufspaltung der A- und B-Exziton-Resonanz in Reflektionsspektren entnommen. Zur Berechnung der Austauschkonstanten müssen die normale Zeeman-Aufspaltung und die Elektron-Loch-Austauschwechselwirkung berücksichtigt werden. Ein Wert $N_o\beta \approx 0,5$ eV wird für $\Delta_{so} < 0$ abgeleitet.



Dieses Werk ist copyrightgeschützt und darf in keiner Form vervielfältigt werden noch an Dritte weitergegeben werden.
Es gilt nur für den persönlichen Gebrauch.

Dieses Werk ist copyrightgeschützt und darf in keiner Form vervielfältigt werden noch an Dritte weitergegeben werden.
Es gilt nur für den persönlichen Gebrauch.

## Abstract

The main aspect of this work is to study a hybrid structure made of metallic ferromagnet (FM) on top of a semiconductor to prove possibilities of spin control via the stray field of a FM.

To achieve an effective sensitivity, a diluted magnetic II-VI semiconductor quantum well (DMSQW) is used, where a film ZnCdMnSe well is used to prove the stray field at a fixed distance from the FM. The s,p-d exchange interaction between magnetic Mn ions and band electrons leads to the giant Zeeman effect with $g$-factors in the order of 500 at low temperature ($T \approx$ 1.5 K). In typical DMSQW with zinc blende symmetry and compressive strain, the exchange interaction of the exciton ground-state is dominated by the p-d coupling of the heavy-hole which has a negligible in-plane magnetic moment and interacts thus mainly with a field component along the quantum well growth direction $z$.

The sample is especially designed with transparent ZnSe substrate to allow photoluminescence (PL) and Faraday rotation (FR) studies. Mn concentration is chosen to obtain an optimal $g$-factor. The thickness of the cap layer of 25 nm is an empirical value to ensure the stable formation of a type I quantum well structure as well as a strong enough magnetic fringe field in the well layer in the case of hybrid structure. Since the Fe/Tb thin film exhibits perpendicular magnetic anisotropy (PMA), it obeys a remanent out-of-plane magnetization which creates the necessary vertical magnetic fringe field component at the position of the DMS well. Patterned FMs ("wire" and "anti-dot" arrays) are fabricated at the Duisburg-Essen University by electron beam lithography of a mask, thermal evaporation of the FM constituents in ultrahigh vacuum and lift-off technique. Wire arrays consist of 1200 nm wide slender bands separated by 800 nm, anti-dot arrays have 1000 nm $\times$ 1000 nm square apertures in the FM. The total height of the FM is smaller than the lateral dimensions. The ratio of FM height to cap layer thickness is designed to optimize the out-of-plane component of magnetic fringe field at the DMS layer. Therefore, this hybrid structure satisfies well the necessary properties for the studies.



Dieses Werk ist copyrightgeschützt und darf in keiner Form vervielfältigt werden noch an Dritte weitergegeben werden.
Es gilt nur für den persönlichen Gebrauch.

At the beginning of this work, molecular beam epitaxy (MBE) grown ZnCdMnSe/ZnSe DMSQWs on transparent substrate are characterized and compared with properties of DMSQWs on GaAs substrate. The excitation intensity dependence of the giant Zeeman splitting shows that the Mn spin temperature is equalized with the lattice temperature via spin-lattice relaxation.

The FM acts as shadow mask for the optical fields and, apart from a minor diffraction contribution, only uncovered sample regions are optically accessed. For photoluminescence (PL), a laser spot with a diameter below 100 $\mu$m was carefully adjusted to the center of the patterned fields. A photon energy of 2.75 eV and an excitation intensity $1W/cm^2$ ensure negligible spin heating. The giant Zeeman splitting associated with the FM fringe field is documented by the shift of the PL maximum in different circular polarization detection. An polarization degree of exciton PL $\mid \rho \mid \approx 30\%$ is found. On the reference DMSQW, an external magnetic field of $B_{ext} \approx 40$ mT is required to achieve the same $\mid \rho \mid$.

The Faraday rotation (FR) technique is used to verify the fringe field by detecting the splitting of exciton states directly. The resulting difference of phase velocity of right and left circularly polarized light yields the rotation of polarization plane of incident linearly polarized light. A rotation angle $\Theta_{FR} \approx 0.3^\circ$ is found corresponding to $B_{ext} \approx 40$ mT for reference sample. The values for FR are fully in agreement with the data obtained from the PL polarization degree studied. Both for PL and FR, the opposite signal signs prove that the FR in the hybrid structure is indeed caused by the reversed fringe field in the regions between FMs.

To perform the spin manipulation of both FM and DMSQW by optical pulse, the Faraday rotation technique is used. A single laser pulse with a photon energy of $E_{ex} \approx 2.1$ eV below the DMS bandgap is chosen to avoid heating of DMSQW as well as substrate and ensures thus dominant interaction with the metallic FMs. FR spectra demonstrate the complete erasing of the average FM magnetization at a pulse energy density at $16mJ/cm^2$. After application of an external field of again $B_{ext} = +5$ T, both FM and DMSQW magnetization appear to be fully restored. Physically, the dominant role of heating in the present experiments is related to the pulses with nanosecond duration used. Nonthermal demagnetization of metallic FMs can be achieved only on a much shorter time scale. To reverse the FM magnetisation, a single laser pulse with again $16mJ/cm^2$ is applied at a reversed


Dieses Werk ist copyrightgeschützt und darf in keiner Form vervielfältigt werden noch an Dritte weitergegeben werden.
Es gilt nur für den persönlichen Gebrauch.

field $B_{ext} = 0.5$ T. The heating pulse enhances the FM temperature reducing coercive field strength $B_c$ below $B_{ext}$. The momentary narrowing of magnetic hysteresis by laser pulse results in the reversing of FM magnetization under the impact of a laser pulse at a biased field.

Finally, $Zn_{1-x}Mn_xO$-epilayers with $x \leq 0.01$ are studied to determine the s,p-d exchange integrals $N_o\alpha$ and $N_o\beta$. The data are extracted from the splitting of A- and B-exciton resonance in reflection spectra. To calculate the exchange interaction constants, the usual Zeeman splitting and the electron-hole exchange interaction should be considered. The likely value $N_o\beta$ is derived to be approximately 0.50 eV for $\Delta_{so} < 0$.



Dieses Werk ist copyrightgeschützt und darf in keiner Form vervielfältigt werden noch an Dritte weitergegeben werden.
Es gilt nur für den persönlichen Gebrauch.

Dieses Werk ist copyrightgeschützt und darf in keiner Form vervielfältigt werden noch an Dritte weitergegeben werden.
Es gilt nur für den persönlichen Gebrauch.

# Contents


**1 Introduction** **1**

**2 Theoretical Aspects of Diluted Magnetic Semiconductors** **5**

2.1 Crystal structure of ZnSe and ZnO . . . . . 5

2.2 Energy band structure of ZnSe and ZnO . . . . . 7

2.3 Heterostructures . . . . . 12

2.4 Magnetic effects . . . . . 15

2.4.1 Manganese in diluted magnetic semiconductor . . . . . 15

2.4.2 Kondo-like model for exchange interaction . . . . . 18

2.5 Excitons . . . . . 21

**3 Samples and Experimental Techniques** **23**

3.1 Sample design . . . . . 23

3.1.1 ZnSe-based diluted magnetic quantum well samples . . 23

3.1.2 ZnO-based epilayer samples . . . . . 26

3.2 Measurement techniques . . . . . 28

3.2.1 Standard requirement for transmittance and reflectivity 28

3.2.2 Photoluminescence technique . . . . . 29



Dieses Werk ist copyrightgeschützt und darf in keiner Form vervielfältigt werden noch an Dritte weitergegeben werden.
Es gilt nur für den persönlichen Gebrauch.

3.2.3 Reflectivity measurement . . . . . 30

3.2.4 Faraday rotation method . . . . . 31

**4 Experimental Results and Discussions 33**

4.1 Sample properties . . . . . 33

4.2 Heating of the Mn spin system by photo-excitation . . . . . 40

4.2.1 Heating by photo-excitation . . . . . 40

4.2.2 Debye model $\lambda \propto T^3$ as thermal transfer mechanism for heating magnetic ions . . . . . 42

4.3 Evidence of fringe field on DMSQW . . . . . 44

4.3.1 Experimental results of polarized PL . . . . . 44

4.3.2 Experimental results of Faraday rotation . . . . . 47

4.3.3 Calculation of fringe field on DMSQW . . . . . 50

4.4 Laser-induced manipulation of FM magnetization . . . . . 55

4.4.1 Erasure of FM magnetization . . . . . 55

4.4.2 Reversal of FM magnetization . . . . . 57

4.5 Exchange interaction in ZnMnO . . . . . 58

4.5.1 Reflection spectra of $Zn_{1-x}Mn_xO$ . . . . . 58

4.5.2 Determination of s,p-d exchange constants of $Zn_{1-x}Mn_xO$ . . . . . 61

**Bibliography 65**

**Danksagung 73**



Dieses Werk ist copyrightgeschützt und darf in keiner Form vervielfältigt werden noch an Dritte weitergegeben werden.
Es gilt nur für den persönlichen Gebrauch.

# Chapter 1

# Introduction

The conventional electronic devices are designed to control the charged carriers via electrical gates. Currently, innovative devices using spin for information processing are considered which offer one possibility for realizing Quantum Computing [1, 2]. Thanks to the molecular beam epitaxy (MBE) growth method, nowadays semiconductor can be designed precisely to meet the requirements of different devices. To control spin, micro magnet with controllable field direction should be used in analogy to the gates used to control charge.

Diluted magnetic semiconductor (DMS) offers an outstanding potential to study magneto-optical properties especially for excitons near band edge. The paramagnetic ions $Mn^{2+}$ in DMS reveal a strong giant Zeeman effect and giant Faraday effect via s,p-d exchange interaction between localized $Mn^{2+}$ 3d electrons and carriers of semiconductor [3]. Additional interactions such as crystal field, strain, and quantum confinement can be inspected more easier in external magnetic field.

There are already some interesting steps in the direction of spintronics [4] just like the spin injection into the Semiconductor (SC) [5–8] or the manipulation of the spin from resident and/or photo-excited carriers in the SC [9, 10]. Polarized photoluminescence (PL) and Faraday rotation (FR) techniques are applied to study these effects.

First goal of this study is the investigation of a hybrid structure made of a ferromagnetic layer (FM) on the top of a DMS to control the Mn and carrier spin in a gate-like way. To assure constant distance between FM and carriers



Dieses Werk ist copyrightgeschützt und darf in keiner Form vervielfältigt werden noch an Dritte weitergegeben werden.
Es gilt nur für den persönlichen Gebrauch.

a DMS quantum well with a cap layer of defined thickness is used. Quantum confinement and strain lead to a splitting of the sub-valence band in the Brillouin zone center with the heavy-hole subband as the uppermost one. Since this hole has only a magnetic moment along growth direction, a FM with out-of-plane magnetization has to be used. For the DMS, ZnSe-based heterostructures are used, the magneto-optical properties are well studied in literatures [11, 12].

In addition, ZnO-based DMS are chosen to study their s,p-d interaction according to promising theoretical predictions [13, 14]. ZnO has the band gap transitions in the UV region. So far, the s,p-d constants have been experimentally figured out on $Zn_{1-x}Co_xO$ epilayers [15] and $p$-type $Zn_{1-x}Mn_xO$ made by oxidation $Zn_{1-x}Mn_xTe$ layers [16]. Surprisingly, values of p-d interaction much smaller than those in ZnSe- and CdTe-based DMS are found.

After this introduction (Chapter 1), the main work is summarized in the following chapters. At the beginning, the theoretical aspects of studied ZnSe- and ZnO-based DMS are given. The crystal structure, the structure of conduction as well as valence band, and specific properties of heterostructures are described schematically. Interactions responsible for energy shifts of the excitons are classified thematically. The significant s,p-d exchange interaction is considered in detail. The circular polarization of the optical transitions is discussed.

Studied samples and applied experimental techniques are illustrated in Chapter 3. Sample designs are listed in tabular form. Different samples of quantum well (QW) and epilayer structures are drawn schematically for comparison. Measurement setups for PL, reflectivity, and Faraday rotation are sketched.

In Chapter 4, the studied samples are characterized at first to ensure the sample properties such as huge $g$-factor and distinct PL. The heating measurement shows the magnetic-field dependent and photo-excitation flux-dependent energy shifts of excitons. The fringe fields of FM nanostructures is studied both by polarization degree of PL as well as by Faraday rotation. Erasing and reversal of FM magnetization using a single laser pulse is demonstrated finally for the DMS-FM hybrid structure.

Finally, ZnO-based semiconductors are studied to determine the s,p-d exchange integrals $N_o\alpha$ and $N_o\beta$. Reflection spectra of non-magnetic ZnO- and semimagnetic $Zn_{1-x}Mn_xO$-epilayers ($x = 0.41\%$ and $0.78\%$) are mea-

Dieses Werk ist copyrightgeschützt und darf in keiner Form vervielfältigt werden noch an Dritte weitergegeben werden.
Es gilt nur für den persönlichen Gebrauch.

sured. The Mn-concentration dependence of exciton energies shows the constant splitting $\Delta_{so}$ between A- and B-exciton resonance. To estimate exchange integrals, the usual Zeeman splitting and the electron-hole exchange interaction should be included in the data analysis. The obtained modulus $N_o \mid \alpha - \beta \mid = 0.25$ eV is responsible for the splitting of the optical allowed $\sigma^{\pm}$ polarized exciton transitions. It shows that this material is much less appropriate for hybrid structure compared to (Zn,Cd,Mn)Se DMSQW with $N_o \mid \alpha - \beta \mid \approx 1.5$ eV.

Dieses Werk ist copyrightgeschützt und darf in keiner Form vervielfältigt werden noch an Dritte weitergegeben werden.
Es gilt nur für den persönlichen Gebrauch.

Dieses Werk ist copyrightgeschützt und darf in keiner Form vervielfältigt werden noch an Dritte weitergegeben werden.
Es gilt nur für den persönlichen Gebrauch.

# Chapter 2

# Theoretical Aspects of Diluted Magnetic Semiconductors

The studied samples are ZnSe- and ZnO-related diluted magnetic semiconductors (DMS), which include quantum well (QW) and epilayer (EP) structures. The magnetic ion $Mn^{2+}$ plays a central role in these DMS for the exchange interaction between Mn-3d electrons and the electrons in conduction and valence band. The giant Zeeman effect from such exchange interaction is the typical consequence of DMS. To understand the physical properties of these DMS, we have to consider the crystal structure, band structure, and the magneto-optical properties. We start the consideration from ZnSe and ZnO single crystals and proceed to DMSQW nanostructures stepwise. Finally, the excitonic transitions will be introduced to explain the aforementioned effects of DMS in magnetic field.

## 2.1 Crystal structure of ZnSe and ZnO

The physical properties are related to the crystal structure of the material. A symmetry operation is one which takes the crystal from initial configuration into an equivalent (indistinguishable) configuration [17]. It determines the symmetry of the Hamiltonian describing the electron states in the crystal. The symmetry operations such as translation, reflection across a plane, inversion through a center and rotation around an axis are the criteria to classify the crystals into different groups.



Dieses Werk ist copyrightgeschützt und darf in keiner Form vervielfältigt werden noch an Dritte weitergegeben werden.
Es gilt nur für den persönlichen Gebrauch.

The crystal families (i.e. groups) can be categorized according to the structure types of Bravais lattices in three dimensions. For the studied II-VI compound semiconductors, both ZnSe and ZnO are formed with tetrahedral $sp^3$ hybrid bonding, which involves the $ns^2$ ($n$ is the principal quantum number) electrons of outer orbitals of the group II elements (i.e. Zn) and $ns^2p^4$ electrons of the group VI elements (i.e. Se or O) [3, 18]. The crystal structures of these two semiconductors are however different. Two possibilities of tetrahedral alignment are realized. Following the group theory, the cubic zinc-blende crystal structure ZnSe (see figure 2.1) and the hexagonal wurtzite crystal ZnO (see figure 2.2) are classified into $T_d$ and $C_{6v}$ groups, respectively[1] [19].

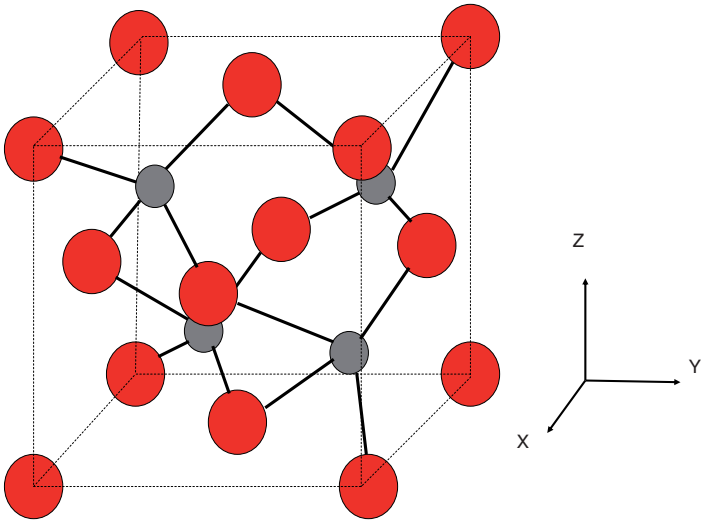


Figure 2.1: Crystal structure of zinc-blende ZnSe

As seen in figure 2.1, the zinc-blende ZnSe crystal structure consists of two fcc-sublattices of Zn (red balls) and Se (smaller grey balls) atoms. The lattice constant of ZnSe amounts to 5.67 $\AA$, which is identical for this cubic crystal in three different orthogonal planes. The black solid line denotes the $sp^3$ covalent bonding between Zn and Se atoms.

The ZnO crystal structure can be seen in the figure 2.2, which consists of two hexagonal-closed-packed (hcp) sublattices of Zn (red balls) and O (smaller grey balls) atoms. ZnO has a substantial ionic character and behaves as anisotropic crystal. This binary compound has hexagonal wurtzite

[1] In the group theory, two symbols of $T_d$ and $C_{6v}$ are used according to Schoenflies notation, which are equivalent to $\bar{4}3m$ and $6mm$ in the international (or Hermann-Mauguin) notation, respectively.

Dieses Werk ist copyrightgeschützt und darf in keiner Form vervielfältigt werden noch an Dritte weitergegeben werden.
Es gilt nur für den persönlichen Gebrauch.

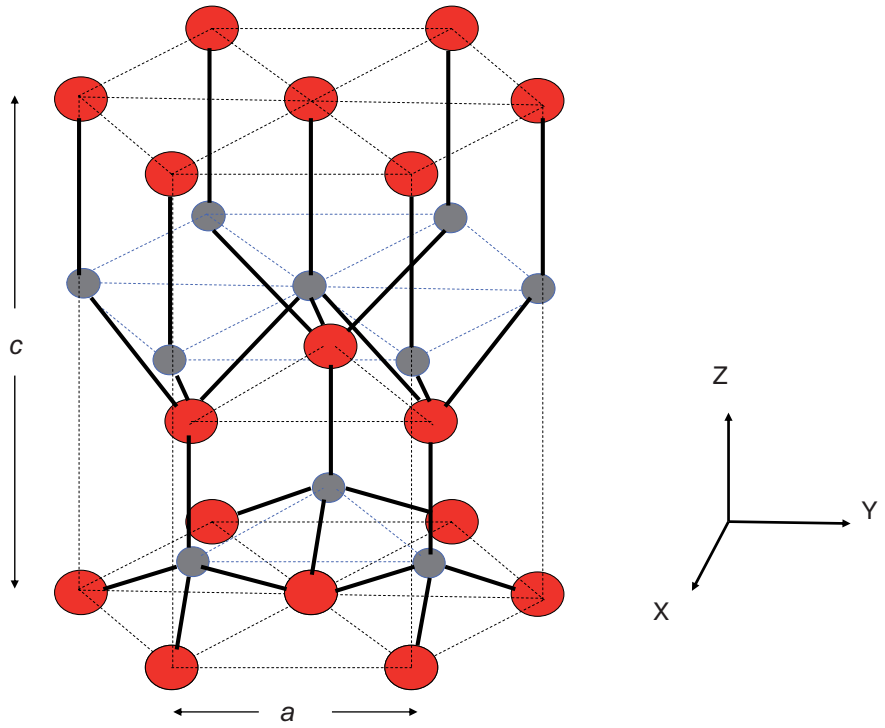


Figure 2.2: Crystal structure of wurtzite ZnO

structure and two different lattice constants[2]. The lattice constants are $a = 3.25$ $\mathring{A}$ between Zn-atoms in a coplane and $c = 5.20$ $\mathring{A}$ between Zn-atoms from two different nearest planes [20]. The black solid line denotes again the shared $sp^3$ covalent and ionic bonding between two different atoms.

## 2.2 Energy band structure of ZnSe and ZnO

In order to describe the allowed electronic states in a semiconductor, we can sketch a simple picture of band structure to express their energy levels. The band diagram can be separated into conduction bands (CB), which consist of unoccupied states; and valence bands (VB), which consist of occupied states.

The regions are called energy bands, where the electrons are allowed to exist and successively distribute; otherwise, the forbidden zones. The studied ZnSe- and ZnO-compounds belong to direct-bandgap semiconductors. The energy gap is equivalent to the distance between the extrema of two neigh-

[2]For cubic crystal, the lattice constant $a$ is identical in three coordinates. But a hexagonal crystal has two different lattice constants $a$ (in $X$-$Y$ plane) and $c$ (along hexagonal axis $Z$) with $c/a = \sqrt{8/3}$ for the ideal hcp structure.

Dieses Werk ist copyrightgeschützt und darf in keiner Form vervielfältigt werden noch an Dritte weitergegeben werden.
Es gilt nur für den persönlichen Gebrauch.

bouring electron energy bands. More precisely, the band gap is the energy difference between the CB minimum and the VB maximum each located at the Brillouin zone center ($\vec{k} = 0$) here.

As seen in the figures 2.3 and 2.4, the structures of CBs for ZnSe and ZnO, respectively, are similar with the symmetries $\Gamma_{6c}$ and $\Gamma_{7c}$. The VB structure is different due to the cubic and hexagonal crystal symmetry, respectively.

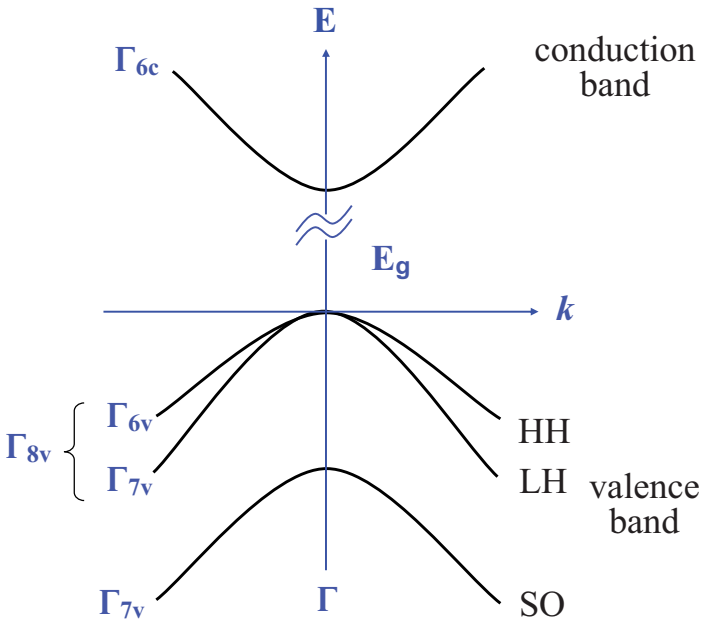


Figure 2.3: Energy band structure of ZnSe around Γ-point

The band diagram of ZnSe in figure 2.3 consists of a twofold degenerate conduction band $\Gamma_{6c}$ and three doubly degenerate sub-valence bands: $\Gamma_{6v}$ (HH: Heavy-Hole), $\Gamma_{7v}$ (LH: Light-Hole), and $\Gamma_{7v}$ (SO: Split-Off). The symbols $\Gamma_{6c}$, $\Gamma_{6v}$, and $\Gamma_{7v}$ are the notations for the cubic crystals corresponding to $T_d$ group. The HH and LH bands are degenerate at the Γ-point ($\vec{k} = 0$). The energy splitting between HH/LH and SO is a consequence of the spin-orbit coupling. The maximum of SO band is about 430 meV away from the maximum of HH/LH subbands. In most cases, it is not necessary to consider the SO band for optical transitions at the band edge region of ZnSe.

For the ZnO crystal, the notations $\Gamma_{7c}$, $\Gamma_{7v}$, and $\Gamma_{9v}$ are used for the $C_{6v}$ group as shown in figure 2.4. The band structure has been studied by Thomas [21] by reflection and absorption spectroscopy in order to assign the energy levels of the lowest *s-like* electrons in conduction band and the topmost three doubly degenerate *p-like* electrons in valence band near the zone center, while the theoretical calculation was completed within the quasi-cubic model by

Dieses Werk ist copyrightgeschützt und darf in keiner Form vervielfältigt werden noch an Dritte weitergegeben werden.
Es gilt nur für den persönlichen Gebrauch.

Hopfield [22]. According to this model, the anisotropy in wurtzite compounds yields formally the field splitting $\Delta_{cf}$ produced by a trigonal uniaxial stress applied to a zinc-blende compound. It amounts to $\Delta_{cf} = +41$ meV in ZnO [23].

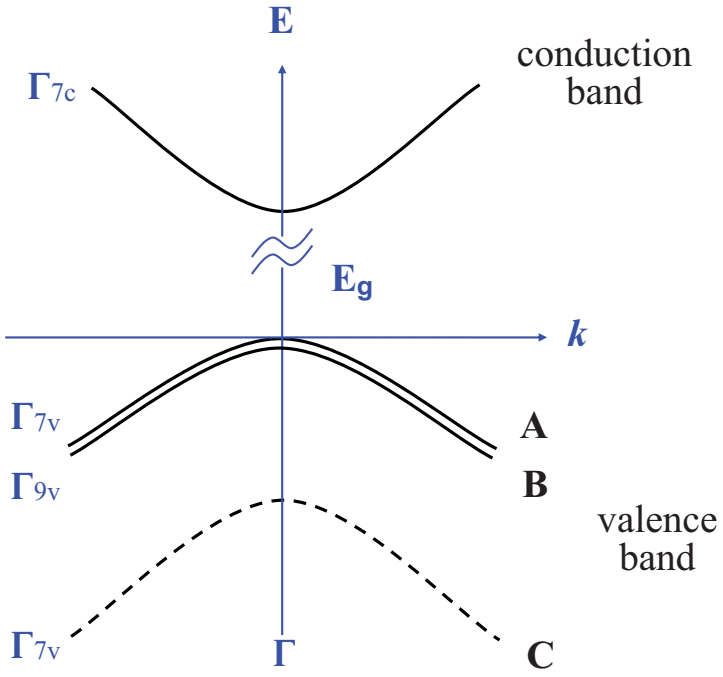


Figure 2.4: Energy band structure of ZnO around Γ-point

The spin-orbit coupling ($\Delta_{so}$) arising from O atom is expected to be smaller than $\Delta_{cf}$. Really, a negative $\Delta_{so}$ = -3 ... -6 meV is found [24, 25], where the negative sign is attributed to the interaction with Zn 3d-electrons [26–29]. Positive values are also reported [30, 31].

The valence band structure is a consequences of $\Delta_{cf}$ and $\Delta_{so}$. Two *p-like* ($p_x$-, $p_y$-*like* states) bands A and B (solid parabolic curves in figure 2.4) near the valence band extreme have a small energy separation with the negative $\Delta_{so}$ . The *p-like* band C (dashed parabolic curve, $p_z$-*like* state) is separated away by crystal field.

The contributions from $\Delta_{cf}$ and $\Delta_{so}$ to valence bands are illustrated in figure 2.5 [32].

Here, the second column shows the splitting due to crystal field $\Delta_{cf}$ ($\Gamma_5$ for the state with $X$-$Y$ component and $\Gamma_1$ for the state with $Z$ component). The third column includes additionally the contribution from spin-orbit coupling $\Delta_{so}$. The dashed lines marked by a star indicate the mutual weak admixture of $\Gamma_5$ and $\Gamma_1$ bands by spin-orbit interaction.

Dieses Werk ist copyrightgeschützt und darf in keiner Form vervielfältigt werden noch an Dritte weitergegeben werden.
Es gilt nur für den persönlichen Gebrauch.

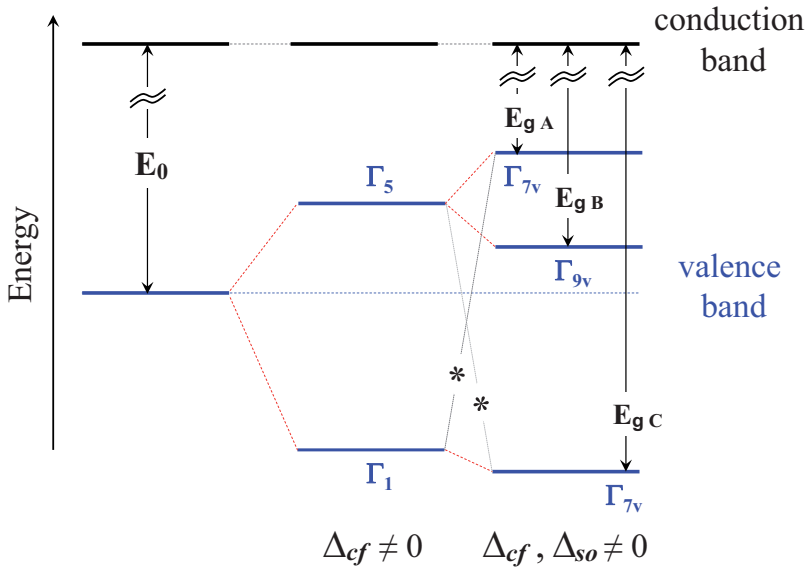


Figure 2.5: Schematic valence band levels of ZnO resulting from $\Delta_{cf}$ and $\Delta_{so}$

Using the above results, we can list the basis eigenvectors of an *s-like* conduction band and three topmost *p-like* valence bands. For ZnSe, they are determined by the Clebsch-Gordan coefficients $\mid J, J_z >$. $J$ is the total angular momentum with the $z$-component $J_z$ ($J_z = \hbar m_J$). We define the spin-up state as $\alpha$ (spin quantum number 1/2, spin vector $\mid 1/2 >$). In a similar way, the spin-down state is defined as $\beta$ (-1/2, spin vector $\mid -1/2 >$).

The eigenfunctions of electron states of the conduction band (CB), the heavy-hole (HH), the light-hole (LH), and the spilt-off hole (SO) in the valence band (VB) can be expressed in linear combinations of eigenfunctions of orbital angular momentum and spin for ZnSe as following

$$\text{CB}: \quad \mid \frac{1}{2}, \frac{1}{2} > \; = S\alpha \tag{2.1a}$$

$$\mid \frac{1}{2}, -\frac{1}{2} > \; = S\beta \tag{2.1b}$$

$$\text{HH}: \quad \mid \frac{3}{2}, \frac{3}{2} > \; = -\frac{1}{\sqrt{2}}(X + iY)\alpha \tag{2.2a}$$

$$\mid \frac{3}{2}, -\frac{3}{2} > \; = \frac{1}{\sqrt{2}}(X - iY)\beta \tag{2.2b}$$

Dieses Werk ist copyrightgeschützt und darf in keiner Form vervielfältigt werden noch an Dritte weitergegeben werden.
Es gilt nur für den persönlichen Gebrauch.

$$\text{LH}: \quad |\frac{3}{2},\frac{1}{2}> = \frac{1}{\sqrt{3}}\left(-\frac{1}{\sqrt{2}}(X+iY)\beta+\sqrt{2}Z\alpha\right) \tag{2.3a}$$

$$|\frac{3}{2},-\frac{1}{2}> = \frac{1}{\sqrt{3}}\left(\frac{1}{\sqrt{2}}(X-iY)\alpha+\sqrt{2}Z\beta\right) \tag{2.3b}$$

$$\text{SO}: \quad |\frac{1}{2},\frac{1}{2}> = \frac{1}{\sqrt{3}}\left(Z\alpha+(X+iY)\beta\right) \tag{2.4a}$$

$$|\frac{1}{2},-\frac{1}{2}> = \frac{1}{\sqrt{3}}\left(Z\beta-(X-iY)\alpha\right)\ , \tag{2.4b}$$

where $S$ stands for *s-like* Bloch function. X, Y, and Z are the Kohn-Luttinger amplitudes with $P_x$, $P_y$, and $P_z$ symmetry, respectively [33].

Due to the uniaxial symmetry of ZnO, there is no defined total angular momentum $J$. Considering the limit of $\Delta_{cf} \gg |\Delta_{so}|$, $\Delta_{so} < 0$ (see figure 2.5), the eigenfunctions for ZnO according to Hopfield's conclusion can be approximately given by

$$\text{CB}: \quad |\frac{1}{2},\frac{1}{2}> = S\alpha \tag{2.5a}$$

$$|\frac{1}{2},-\frac{1}{2}> = S\beta \tag{2.5b}$$

$$\text{A}: \quad \frac{1}{\sqrt{2}}(X+iY)\beta - wZ\alpha \tag{2.6a}$$

$$-\frac{1}{\sqrt{2}}(X-iY)\alpha + wZ\beta \tag{2.6b}$$

$$\text{B}: \quad |\frac{3}{2},\frac{3}{2}> = -\frac{1}{\sqrt{2}}(X+iY)\alpha \tag{2.7a}$$

$$|\frac{3}{2},-\frac{3}{2}> = \frac{1}{\sqrt{2}}(X-iY)\beta \tag{2.7b}$$

$$\text{C}: \quad Z\alpha - w(X+iY)\beta \tag{2.8a}$$

$$Z\beta + w(X-iY)\alpha\ , \tag{2.8b}$$

Dieses Werk ist copyrightgeschützt und darf in keiner Form vervielfältigt werden noch an Dritte weitergegeben werden.
Es gilt nur für den persönlichen Gebrauch.

where $S$ stands again for *s-like* state in the conduction band (CB) ($\Gamma_{7c}$ in figure 2.4). X, Y, and Z have the same meanings as in equations 2.1 to 2.4. $w$ stands for the weak admixing ($|w| \ll 1$) due to finite $\Delta_{so}$ from the associated X-Y or Z component. The A, B, and C represent the double states of $\Gamma_{7v}$, $\Gamma_{9v}$, and lowest $\Gamma_{7v}$ in figure 2.4, respectively.

## 2.3 Heterostructures

The studied heterostructures are made from mixed crystals based on ZnSe or ZnO (see section 3.1). These mixed crystals can be treated by using the virtual crystal approximation (VCA) to hold the translation invariance for the electronic behaviour in the lattice. Introducing of a low fraction of admixture during the growth by molecular beam epitaxy (MBE) (i.e. Cd, Mn into ZnSe or Mn, Mg, Cd into ZnO) should not change the crystal structure of host semiconductor [3], but the lattice constant $a$ and the band gap energy $E_g$ will be modified.

Vegard's law describes a linear relation between the lattice constant of mixed crystal and the concentrations of the constituent elements [34]. E.g. in the case of Mn as admixture in ternary semiconductor yields

$$a(x) = (1 - x) \cdot a_{II-VI} + x \cdot a_{Mn-VI} \ , \tag{2.9}$$

where $a$ represents the lattice constant, $x$ the Mn fraction, *II-VI* for the host *II-VI* group semiconductor, *Mn-VI* for the *Mn-VI* compound. In contrast, the band gap energy is usually not linearly dependent on the concentration $x$. The relation

$$E_g(x) = (1 - x) \cdot E_{g,II-VI} + x \cdot E_{g,Mn-VI} + x \cdot (1 - x) \cdot b \tag{2.10}$$

includes a charge-transfer induced bowing term. Here $E_g$ are the respective band gap energies, $b$ is the bowing parameter. These formulas for ternary semiconductor can be extended to quaternary compounds, e.g. for $Zn_{1-x-y}Cd_yMn_xSe$.

In addition to the variation of energy levels caused by admixture, the growth of heterostructures will influence band energies by strain effect.

Dieses Werk ist copyrightgeschützt und darf in keiner Form vervielfältigt werden noch an Dritte weitergegeben werden.
Es gilt nur für den persönlichen Gebrauch.

The growth induced strain will lead to deformation potential, which varies the band energy levels. The figure 2.6 shows the uniaxial strain effects on the conduction band CB and the two topmost valence subbands HH (J = 3/2, $m_J = \pm 3/2$) and LH (J = 3/2, $m_J = \pm 1/2$) in a zinc-blende structure [23, 35].

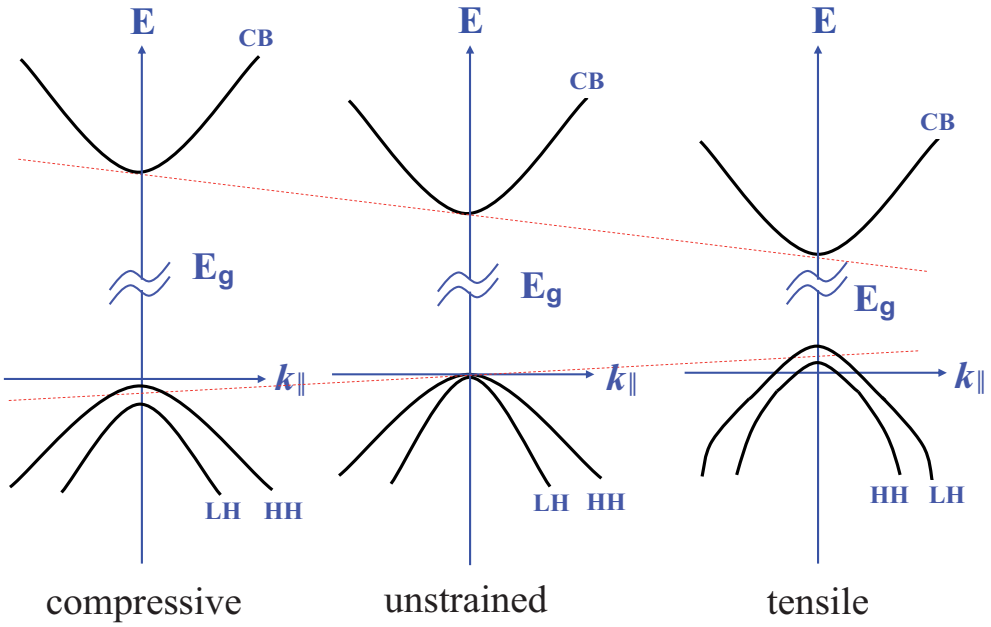


Figure 2.6: Strain effects on band structures for ZnSe zinc-blende structure

As expressed in the figure 2.6, the HH and LH are degenerate at Γ-point ($\vec{k} = 0$) in unstrained material. A compressive strain shifts the HH and LH energetically downwards and the CB upwards. The energy level of HH lies above that of LH, which is the case for our studied QWs. The band gap energy $E_g$ is larger than that of unstrained materials. A tensile strain has the inverse effect on HH and LH. It shifts both subbands upwards which is again opposite to the CB. The LH exceeds HH that leads to an increased band mixing between HH and LH at finite $\vec{k}$. The band gap energy becomes smaller by tensile strain [36].

If a small strain $\delta$ in $z$-direction is considered for a hexagonal ZnO heterostructures ($\delta \ll E_g$), the strain-induced energy shift can be attributed, in principle, to a small modification of $\Delta_{cf}$. So the order of the energy levels should not be affected.

QW structure can be realized by two different semiconductors in the form of a double heterostructure as illustrated in figure 2.7. The studied samples are designed as type I QW which are fabricated with the relaxed barriers and a pseudomorphic growth for the well layer.

Dieses Werk ist copyrightgeschützt und darf in keiner Form vervielfältigt werden noch an Dritte weitergegeben werden.
Es gilt nur für den persönlichen Gebrauch.

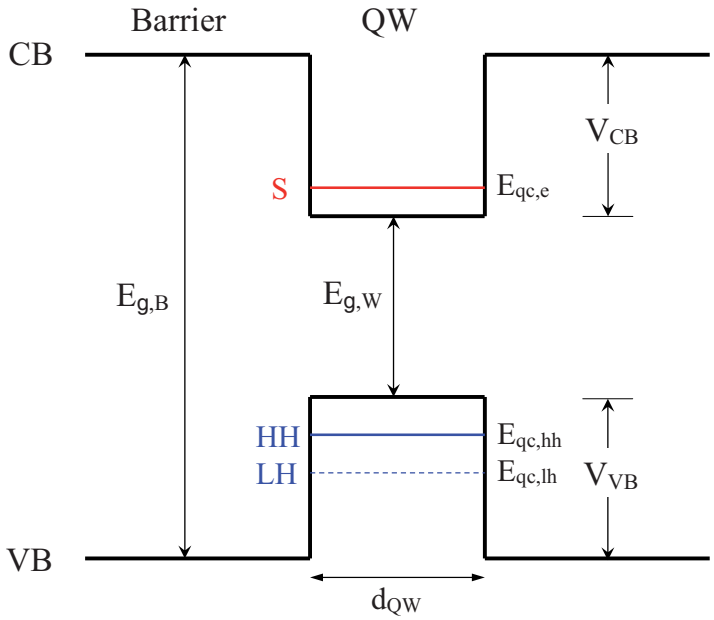


Figure 2.7: Schematic energy levels in QW structure

The schematic picture 2.7 describes the energy levels in QW structure with well thickness $d_{QW}$. Two different band gaps of barrier and the well material are denoted by $E_{g,B}$ and $E_{g,W}$, respectively. The ratio of band offsets $V_{CB}$ for CB and $V_{VB}$ for VB relates to the material composition in barrier and well. The energies for the first confined level can be written as

$$E_{CB} = E_{g,W} + E_{qc,e} + \frac{\hbar^2 k_{e,\parallel,CB}^2}{2m_{e,\parallel,CB}}, \tag{2.11a}$$

$$E_{VB} = -E_{qc,h} - \frac{\hbar^2 k_{e,\parallel,VB}^2}{2m_{e,\parallel,VB}}, \tag{2.11b}$$

where the subscript CB and VB represents conduction band and valence band, respectively. $E_{qc,e}$ and $E_{qc,h}$ stand for the confinement energies of electrons in the CB (shifted to higher energies) and VB (shifted to lower energies, $h$: $hh$ and $lh$), $m_{e,\parallel,CB}$ and $m_{e,\parallel,VB}$ are the effective in-plane masses, $\overrightarrow{k}_{e,\parallel,CB}$ and $\overrightarrow{k}_{e,\parallel,VB}$ are the in-plane wavevectors.
Depending on the QW structure, both $E_{q,B}$ and $E_{q,W}$ as well as the relative band offset are modified by strain and s,p-d exchange interaction (see section 2.4).

Dieses Werk ist copyrightgeschützt und darf in keiner Form vervielfältigt werden noch an Dritte weitergegeben werden.
Es gilt nur für den persönlichen Gebrauch.

## 2.4 Magnetic effects

Magnetic interactions influence the electron energies for semiconductors. The magnetic energy $U(B)$ can be stored in a system with three well-known forms given by

$$U(B) = \begin{cases} (n+\frac{1}{2})\hbar\omega_c,\ \omega_c = eB/m_e & \text{Landau levels,} \\ \frac{1}{2}g_e\mu_B B & \text{usual Zeeman effect,} \\ \frac{1}{2}\tilde{g}\mu_B B & \text{giant Zeeman effect,} \end{cases} \tag{2.12}$$

where $B$ is the magnetic field, $\omega_c$ a cyclotron frequency, $n$ an integer denoting the level order, $g_e$ or $\tilde{g}$ an effective $g$-factor for electron (with spin $\frac{1}{2}$) in semiconductor or in DMS, $\mu_B$ is the Bohr magneton. The topmost equation is related to the orbital angular momentum for free electrons. $g_e$ in the middle equation depends on the semiconductor and can differ remarkable from the free electron value. The lowest equation has an huge effective electron $g$-factor for DMS from s,p-d exchange interaction.

### 2.4.1 Manganese in diluted magnetic semiconductor

Manganese (Mn) belongs to the group of transition metal (TM) and has the electron configuration [Ar]$3d^5 4s^2$. It has been utilized as magnetic element in the studied diluted magnetic semiconductors. Due to its two valence electrons in outer shell, it can replace a cation, namely divalent element Zn or Cd, to form an undoped DMS. According to the Hund's rule, a free $Mn^{2+}$-ion in the ground state has the total spin S = 5/2 and zero orbital momentum from the five 3d electrons. In magnetic field, the system of the five Mn 3d electrons splits into six different levels ($m_S = -5/2\ , \ldots , 5/2$).

The interaction between 3d electrons of two neighbouring $Mn^{2+}$-ions is known as d-d exchange interaction which can be given by spin-5/2 Heisenberg Hamiltonian

$$\mathcal{H}_{d-d} = -\sum_{i \neq j} \mathcal{J}^{d-d}(R_{ij}) \vec{S}_i \cdot \vec{S}_j\ , \tag{2.13}$$

where the $\mathcal{J}^{d-d}(R_{ij})$ stands for the exchange integral between 3d electrons from two different $Mn^{2+}$-ions located at the positions i and j (with spin

Dieses Werk ist copyrightgeschützt und darf in keiner Form vervielfältigt werden noch an Dritte weitergegeben werden.
Es gilt nur für den persönlichen Gebrauch.

$\vec{S}_i$ and $\vec{S}_j$, the distance $R_{ij} = |\overrightarrow{R_{ij}}|$) [37]. This pair can be two nearest-neighbouring $Mn^{2+}$-ions (denoted as *NN* with exchange integral $\mathcal{J}_{NN}^{d-d}$), the two next-nearest-neighbouring $Mn^{2+}$-ions (denoted as *NNN* with exchange integral $\mathcal{J}_{NNN}^{d-d}$), and so on.

Both $\mathcal{J}_{NN}^{d-d}$ and $\mathcal{J}_{NNN}^{d-d}$ are negative, which reveal the antiferromagnetic (AF) coupling of d-d exchange interaction. $\mathcal{J}_{NN}^{d-d}$, e.g. is dominated by superexchange mechanism coming from two neighbouring $Mn^{2+}$-ions through a non-magnetic anion (e.g. $Se^{2-}$) by virtual hopping processes [38, 39]. A antisymmetric p-d hybridization can be formed between $Se^{2-}$ p-shell and $Mn^{2+}$ d-shell. The two $Se^{2-}$ p-electrons with antiparallel spins lead to the antiferromagnetic coupling. The $Mn^{2+}$-$Mn^{2+}$ *NN* coupling leads to the formation of Mn pairs with the total spin $\vec{S}_i + \vec{S}_j = 0$ and higher clusters. Experimental values determined by neutron scattering for $Zn_{(1-x)}Mn_xSe$ are $\mathcal{J}_{NN}^{d-d}/k_B \approx$ -12.2 K and $\mathcal{J}_{NNN}^{d-d}/k_B \approx$ -3.0 K ($k_B$ Boltzmann constant) [39, 40]. The pair and higher cluster formation by d-d interactions will reduce the thermal expectation of $Mn^{2+}$ spins in magnetic field. For the experimental temperatures of interest between 2 to 20 K, the *NNN* contribution is smaller than or equal to the thermal energy ($\mathcal{J}_{NNN}^{d-d} \lessapprox k_BT$) and alignment of $Mn^{2+}$ spins via $\mathcal{J}_{NNN}^{d-d}$ can be neglected.

A magnetic semiconductor based from II-VI group can be given by the chemical formula $A^{II}_{(1-x-y)}B^{II}_{y}Mn_xC^{VI}$ with Mn fraction $x$. The magnetic states of $Mn^{2+}$ spin system in the semiconductor can be classified into the following phases [11]

$$\text{Mn fraction } x \begin{cases} x < 0.01 & \text{paramagnetic phase,} \\ 0.01 < x < 0.15 & \text{quasi-paramagnetic phase,} \\ 0.2 < x & \text{spin-glass phase.} \end{cases} \tag{2.14}$$

For our investigation, only the (quasi-)paramagnetic phase of $Mn^{2+}$-ions is of interest. The thermal expectation of $z$-component of the spins $\langle S_z \rangle$ from an isolated $Mn^{2+}$-ion depends on the temperature and the applied magnetic field $B = (0, 0, B_z)$ [41]. $\langle S_z \rangle$ can be given by

$$\langle S_z \rangle = -S\mathcal{B}_S\left(\frac{\mu_B g_{Mn} SB}{k_B T_s}\right), \tag{2.15}$$

where $\mathcal{B}_S$ is the Brillouin function with $S = 5/2$, $g_{Mn} \approx 2$ the effective Landé $g$-factor for $Mn^{2+}$ 3d electrons and $T_s$ the $Mn^{2+}$ spin temperature.

Dieses Werk ist copyrightgeschützt und darf in keiner Form vervielfältigt werden noch an Dritte weitergegeben werden.
Es gilt nur für den persönlichen Gebrauch.

The Brillouin function $\mathcal{B}_S$ with $S = 5/2$ can be expressed by [41]

$$\mathcal{B}_{5/2}(\xi) = \frac{6}{5}\coth\frac{6\xi}{5} - \frac{1}{5}\coth\frac{\xi}{5}\,. \tag{2.16}$$

For quasi-paramagnetic phase of Mn, we have to use an effective concentration $x_{eff}$ of single $Mn^{2+}$-ion instead of total Mn concentration $x$ [42, 43]. For the relevant range $x < 0.1$, only the above mentioned *NN* Mn pair formation must be considered and the relation between $x_{eff}$ and $x$ for the zinc-blende structure with $Mn^{2+}$ substituting $Zn^{2+}$ can be given by

$$x_{eff} \approx x \cdot (1-x)^{12}\,. \tag{2.17}$$

The power of 12 stems from the number of neighbours in the fcc lattice. The concentration of single $Mn^{2+}$-ion $x_{eff}$ is equivalent to the product of $x$ (existing $Mn^{2+}$-ion) and $(1-x)^{12}$ (the probability to find no $Mn^{2+}$-ion on the neighbouring cation sites).
The magnetization of $Mn^{2+}$-ions *M(T,B)* is directly related to the average spin of all single $Mn^{2+}$-ions $x_{eff}N_0\langle S_z\rangle$ and can be expressed by

$$\begin{aligned} M(T,B) &= -x_{eff}N_0 g_{Mn}\mu_B S\mathcal{B}_{5/2}\left(\frac{\mu_B g_{Mn} SB}{k_B(T_s+T_0)}\right) \\ &= x_{eff}N_0 g_{Mn}\mu_B\langle S_z\rangle\,. \end{aligned} \tag{2.18}$$

Here $N_0$ is the number of cations per unit volume. The introduction of a phenomenological temperature $T_0$ (i.e. Curie-Weiss temperature from the coupling of pairs of *NN* $Mn^{2+}$-ions) accounts phenomenologically, besides $x_{eff}$, for the d-d antiferromagnetic exchange interaction.

In the low field region, the magnetization $M$ is proportional to magnetic field $B$, i.e. the magnetic susceptibility $\chi = M/B$ is constant. At low temperatures, $\chi$ obeys the Curie-Weiss law with $\chi = C(x)/(T_s + T_0)$.

Since the magnetization of $Mn^{2+}$-ion has a strong dependence on the Mn spin temperature $T_s$, any heating of the spin system is a critical issue for magneto-optical studies. As shown in figure 2.8, the heat transfer from photocarriers to the $Mn^{2+}$-ion system can be either straightforwardly or phonon-participated [44, 45].

Dieses Werk ist copyrightgeschützt und darf in keiner Form vervielfältigt werden noch an Dritte weitergegeben werden.
Es gilt nur für den persönlichen Gebrauch.

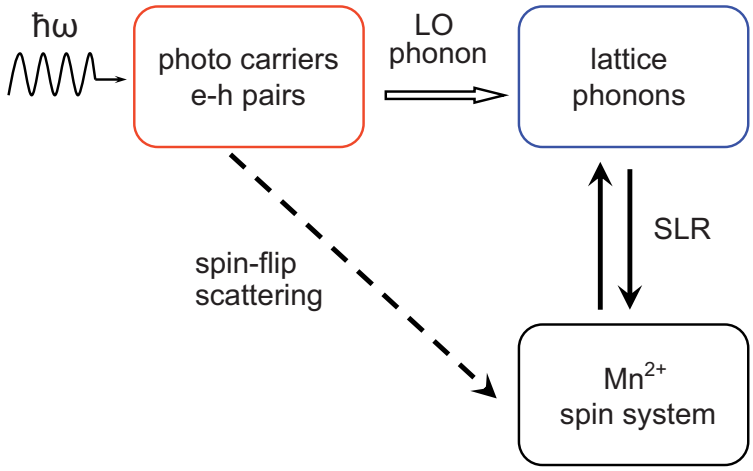


Figure 2.8: Two main heating mechanisms of $Mn^{2+}$ spin system

### 2.4.2 Kondo-like model for exchange interaction

Now, we come back to comprehend the s-d coupling ($s$-electron in CB with d electrons of $Mn^{2+}$) and p-d coupling ($p$-*like* electron in VB with d electrons of $Mn^{2+}$), namely, s,p-d exchange interaction, which leads to the giant Zeeman effect of the related electrons. The coupling between localized magnetic moment and mobile carrier spin in semiconductor can be represented by a Kondo-like Hamiltonian [3, 37, 46]

$$\mathcal{H}_{s,p-d}(\vec{r}) = -\sum_m \mathcal{J}^{s,p-d}(\vec{r} - \overrightarrow{R_m})\overrightarrow{S_m} \cdot \vec{\sigma} \tag{2.19a}$$

$$= -\sigma_z \langle S_z \rangle x_{eff} \sum_n \mathcal{J}^{s,p-d}(\vec{r} - \overrightarrow{R_n}) \,, \tag{2.19b}$$

where $\mathcal{J}^{s,p-d}(\vec{r} - \overrightarrow{R_m})$ is the exchange integral, $\overrightarrow{S_m}$ and $\vec{\sigma}$ the spin operators for the m's $Mn^{2+}$-ion at the position $\overrightarrow{R_m}$ and band electron at $\vec{r}$, respectively. The equation 2.19a can be rewritten as 2.19b for the following reasons. Since the electron wave function is extended over many lattice sites, the $\overrightarrow{S_m}$ can be replaced by the thermal average $\langle S_z \rangle$ using mean-field approximation (MFA). For a magnetic field applied along $z$, only the $z$-component of spin for band electron $\sigma_z$ is requested. Since the electron wave function reaches numerous lattice sites, $\mathcal{J}^{s,p-d}(\vec{r} - \overrightarrow{R_m})$ can be substituted by $\mathcal{J}^{s,p-d}(\vec{r} - \overrightarrow{R_n}) \cdot x_{eff}$ for each cation site with an effective $Mn^{2+}$ concentration $x_{eff}$ under the assumption of VCA.

Dieses Werk ist copyrightgeschützt und darf in keiner Form vervielfältigt werden noch an Dritte weitergegeben werden.
Es gilt nur für den persönlichen Gebrauch.

**s-d exchange interaction:** The *s-like* electrons in CB perform a direct interaction with localized $Mn^{2+}$ magnetic moments. The coupling can be regarded as the first perturbation of Coulomb direct exchange that leads to a ferromagnetic Kondo Hamiltonian with the total magnetic moments of $Mn^{2+}$ [47]. A s-d hybridization is forbidden by symmetry at the Γ-point. Consequently, this exchange interaction exhibits ferromagnetic coupling and with positive exchange constant $\alpha > 0$ ($\alpha \equiv < s_e \; |\mathcal{J}^{s-d}| \; s_e >$ in a unit volume, where $|s_e>$ is the Kohn-Luttinger amplitude for *s*-electrons in CB). From the perturbation theory for the first order approximation at the Γ-point, the energy shift of *s*-electron through s-d exchange interaction can be expressed approximately by [11, 41]

$$\Delta E^{e}_{s-d} = x_{eff}\, N_0\, \alpha \langle S_z \rangle \, \langle \sigma_z \rangle \,; \quad \langle \sigma_z \rangle = \pm \frac{1}{2} \,. \tag{2.20}$$

$\langle \sigma_z \rangle$ is the expectation value of *z*-component of spin for *s*-electron in the conduction band.

**p-d exchange interaction:** The *p-like* electrons in VB are from anions (e.g. $Se^{2-}$). The interaction between *p-like* electrons and the localized $Mn^{2+}$ magnetic ions is known as p-d exchange interaction. A antisymmetric p-d hybridization can be formed between $Se^{2-}$ p-shell and $Mn^{2+}$ d-shell. This hybridization leads to a very strong antiferromagnetic coupling with negative exchange constant $\beta < 0$ ($\beta \equiv < J_h \; |\mathcal{J}^{p-d}| \; J_h >$ in a unit volume, where $|J_h>$ is a Kohn-Luttinger amplitude for *p*-electrons in VB [41]). In fact, $\beta$ has a larger magnitude than $\alpha$ (e.g. $Zn_{1-x}Mn_xSe$: $N_0\alpha$ = 260 meV, $N_0\beta$ = -1310 meV [48]). According to the perturbation theory again, the p-d exchange interaction induced energy splitting at the Γ-point can be given by

$$\Delta E^{h}_{p-d} = x_{eff}\, N_0\, \beta \langle S_z \rangle \, \langle \sigma_{z,VB} \rangle \,; \quad \langle \sigma_{z,VB} \rangle = \pm \frac{1}{2} \text{ for HH}, \pm \frac{1}{6} \text{ for LH}. \tag{2.21}$$

Here $\langle \sigma_{z,VB} \rangle$ is the expectation value of *z*-component of spin for *p*-electrons in valence band.

The equations 2.20 and 2.21 are valid for the cubic crystal (e.g. ZnCdMnSe) with defined Clebsch-Gordan coefficients $\mid J, J_z >$ ($J_z = \hbar m_J$) and for hexagonal crystal with $\Delta_{so} \gg \Delta_{cf}$. With help of the equations 2.5 to 2.8 for the ZnO-based DMS, it follows

Dieses Werk ist copyrightgeschützt und darf in keiner Form vervielfältigt werden noch an Dritte weitergegeben werden.
Es gilt nur für den persönlichen Gebrauch.

$$\Delta E^{e}_{s-d} = x_{eff}\, N_0\, \alpha_{ZnO} \langle S_z \rangle \langle \sigma_z \rangle\,;\ \langle \sigma_z \rangle = \pm\frac{1}{2} \text{ for CB,} \tag{2.22a}$$

$$\Delta E^{A}_{p-d} \approx x_{eff}\, N_0\, \beta_{ZnO} \langle S_z \rangle \langle \sigma_{z,VB,A} \rangle\,;\ \langle \sigma_{z,VB,A} \rangle = \pm\frac{1}{2} \text{ for A band,} \tag{2.22b}$$

$$\Delta E^{B}_{p-d} = x_{eff}\, N_0\, \beta_{ZnO} \langle S_z \rangle \langle \sigma_{z,VB,B} \rangle\,;\ \langle \sigma_{z,VB,B} \rangle = \pm\frac{1}{2} \text{ for B band.} \tag{2.22c}$$

$\langle \sigma_{z,VB} \rangle$ is the expectation value of electron spin for $z$-component in valence band, $\alpha_{ZnO}$ and $\beta_{ZnO}$ are the exchange constants for s-d and p-d in ZnO, respectively. The A band is assumed to have negligible mixing with C band.

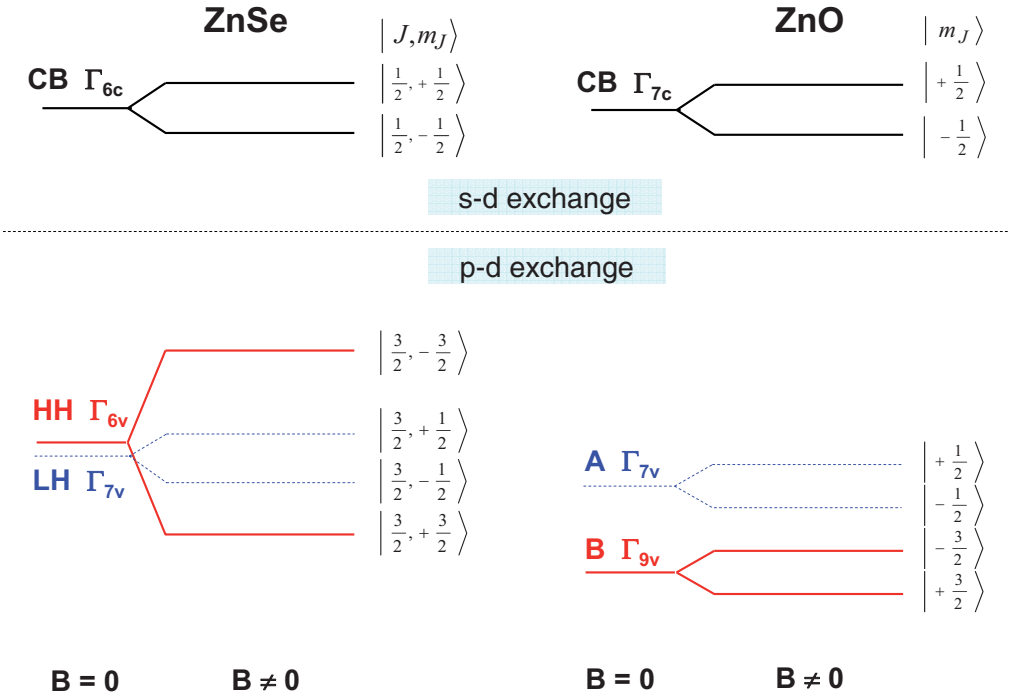


Figure 2.9: Schematic representation of energy splitting from s,p-d exchange interaction in Faraday configuration for ZnSe (left) and ZnO (right) with $\beta < 0$, $m_J$ is the projection of total angular momentum in $z$-direction for electron (or hole) in CB (or VB).

In figure 2.9, the giant Zeeman effect is summarized for ZnSe and ZnO. In the left side for ZnSe, the two subbands $\Gamma_{6v}$ (HH) and $\Gamma_{7v}$ (LH dashed drawing) are assumed to be separated by confinement in a QW and/or a compressive strain (as for the studied samples). A strong magnetic-field induced splitting from s,p-d exchange interaction for $\Gamma_{6c}$ in conduction band (CB) as well as $\Gamma_{6v}$ (HH) and $\Gamma_{7v}$ (LH) in valence band (VB) can be seen, respectively. On the right hand side for ZnO, the separation between A

Dieses Werk ist copyrightgeschützt und darf in keiner Form vervielfältigt werden noch an Dritte weitergegeben werden.
Es gilt nur für den persönlichen Gebrauch.

(dashed drawing) and B at $B = 0$ stems mainly from $\Delta_{so}$ (see figure 2.5). For ZnO, the magnetic quantum numbers $m_J$ are given.

## 2.5 Excitons

Exciton effects dominate the optical transitions of wide band gap semiconductors at the band edge. A valence electron excited into CB leaves a hole (vacant electron) in VB. The in-plane wavevector $\overrightarrow{k_h}$, $z$-component of spin $j_{h,z}$ and the energy $E_h$ of a hole can be derived from the VB electron values in the VB as

$$\begin{cases} \overrightarrow{k_{h,\parallel}} = -\overrightarrow{k_{e,\parallel,VB}} \,, \\ j_{h,z} = -j_{e,z,VB} \,, \\ E_h = -E_{e,VB} \,. \end{cases} \tag{2.23}$$

The bound state of an electron-hole pair is known as exciton, which is hold through attractive Coulomb interaction. The Hamiltonian for exciton in a QW can be generalized by

$$\begin{aligned} \mathcal{H} = E_{g,W} + V_e(z_e) + V_h(z_h) + \frac{\hbar^2}{2m_{e,\parallel}} \frac{\partial^2}{\partial^2_{\vec{\rho_e}}} + \frac{\hbar^2}{2m_{h,\parallel}} \frac{\partial^2}{\partial^2_{\vec{\rho_h}}} \\ + \frac{\hbar^2}{2m_{e,\perp}} \frac{\partial^2}{\partial^2_{z_e}} + \frac{\hbar^2}{2m_{h,\perp}} \frac{\partial^2}{\partial^2_{z_h}} - \frac{e^2}{4\pi\varepsilon_0\varepsilon|\vec{r_e} - \vec{r_h}|} \,. \end{aligned} \tag{2.24}$$

Here the subscript $e$ ($h$) denotes the electron (hole). At the right hand side, the first term $E_{g,W}$ is the modified band gap energy for QW layer, which includes the contributions from admixture, strain, and s,p-d exchange interaction as described in former sections. $V_{e,h}$ are the confining potentials. The position vector, containing in-plane and vertical parts, is expressed by $\vec{r} = (\vec{\rho}, z)$. $\varepsilon$ is the static permittivity for the Coulomb attractive potential. $m_{e(h),\parallel}$ and $m_{e(h),\perp}$ are the in-plane and vertical effective masses for electron (hole), respectively, which are derived from diagonal approximation of Kohn-Luttinger Hamiltonian.

For the studied DMS heterostructures of type I, the exciton energy can be formally expressed by $E_X = E_{g,W} + E_{qc,e} + E_{qc,h} - E^b_X$, where $E^b_X$ is the exciton binding energy. $E_X$ can only be calculated by numerical method [49–

Dieses Werk ist copyrightgeschützt und darf in keiner Form vervielfältigt werden noch an Dritte weitergegeben werden.
Es gilt nur für den persönlichen Gebrauch.

51]. For the case, where magnetic ions are only placed in the QW region, the energy shift of the exciton in a magnetic field is often directly related to the shift of the energy bands yielding $\Delta E_X(B) = \gamma[\Delta E_{CB,W}(B) - \Delta E_{VB,W}(B)]$, where $\gamma$ is the probability to find the electron-hole pair in the well [52]. The energy splitting of the optically allowed exciton states can be derived from schematic picture 2.9 using equations 2.20 and 2.21. For a setup in Faraday geometry (light vector parallel to magnetic field and QW growth direction here, $\vec{k} \parallel \vec{B}$ in $z$-direction), one gets figure 2.10. Here, only $\sigma$ polarization has to be considered.

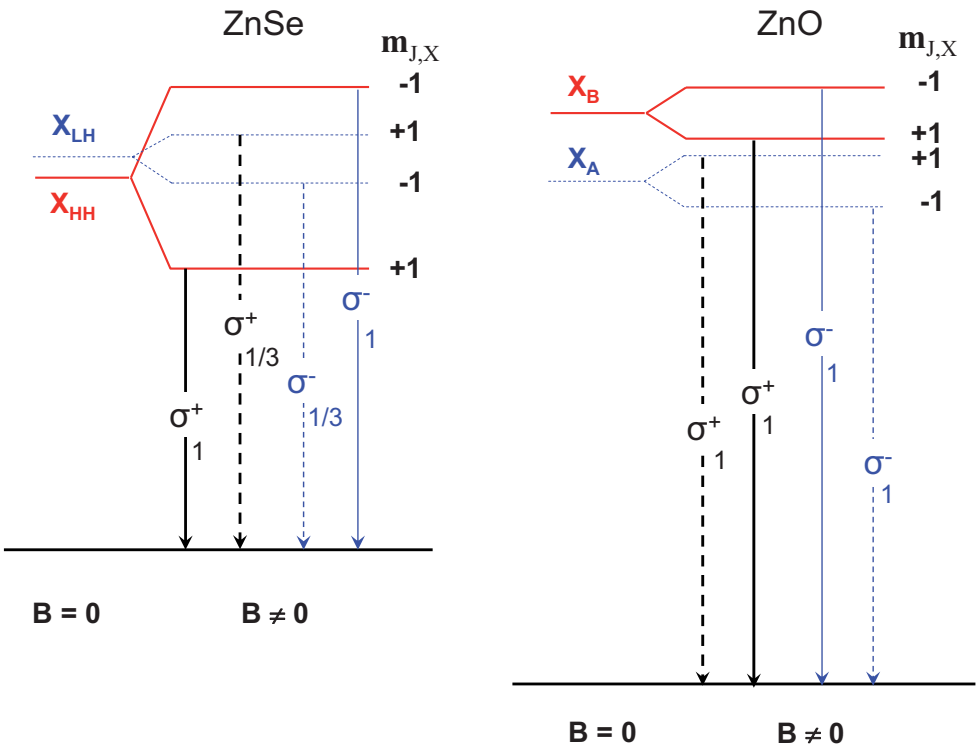


Figure 2.10: Schematic representation of the optically allowed exciton transitions for ZnSe and ZnO in magnetic field in Faraday geometry with $\beta < 0$ and $|\beta| > \alpha$, $\sigma^+$ and $\sigma^-$ are circular polarizations of the light. The numbers represent the relative transition intensities as follows from the CB and VB states (see equations 2.1 to 2.7) [41].

In figure 2.10, $m_{J,X}$ is equal to $m_{J,e} + m_{J,h}$, which is the projection of the total angular momentum for exciton. Following the selection rule, $m_{J,X} = \pm 1$ stands for $\sigma^{\pm}$-exciton transition. $\pi$-exciton transitions (linear polarized light not seen in Faraday geometry) can occur for $m_{J,X} = 0$.

Dieses Werk ist copyrightgeschützt und darf in keiner Form vervielfältigt werden noch an Dritte weitergegeben werden.
Es gilt nur für den persönlichen Gebrauch.

# Chapter 3

# Samples and Experimental Techniques

The studied ZnSe- and ZnO-based samples will be described with respect to the growth methods and layer sequence in the beginning of this chapter. A description of the different experimental techniques and the respective analytic methods follows, which have been applied to investigate the samples.

## 3.1 Sample design

### 3.1.1 ZnSe-based diluted magnetic quantum well samples

The ZnSe-based semiconductors have been grown by MBE. To prepare diluted magnetic quantum well (DMSQW) structures, ZnSe layers are used as barriers and $Zn_{1-x-y}Cd_yMn_xSe$ thin film as the well layer. The energy band gap of ZnSe bulk material amounts to 2.82 eV at low temperature (T $\leq$ 10 K) [53–55]. Just as described in section 2.3, increasing Mn fraction will raise the energy gap. Thus we have to introduce additionally cadmium to reduce the band gap of the well layer in order to accomplish a type I quantum well. The energy band gaps of CdSe [36] and MnSe [41] crystal are 1.84 eV and 3.20 eV at low temperature (T $\leq$ 10 K), respectively. A ratio of $x/y \leqq 0.5$ and $y \approx 0.15$ has been chosen to ensure a robust carrier confinement in the DMS well. Samples were grown either on a gallium arsenide (GaAs) or a zinc


Dieses Werk ist copyrightgeschützt und darf in keiner Form vervielfältigt werden noch an Dritte weitergegeben werden.
Es gilt nur für den persönlichen Gebrauch.

selenide (ZnSe) substrate, which have opaque or transparent properties, respectively. The samples with ZnSe substrate can be applied for transmission and Faraday rotation measurements. Table 3.1 describes the growth design for the studied ZnSe-based DMSQW samples and figure 3.1 illustrates the growing sequence of these DMSQW samples schematically.

Table 3.1: Specification of ZnSe-based DMSQW samples

| Serial number of sample | Substrate | Buffer | Well layer ZnCdMnSe | Cap layer |
|---|---|---|---|---|
| ZCMS 431B | ZnSe (001) 8 x 8 x 1.7 mm | ZnSe: 0.85 $\mu$ m | 17 ML Mn $\approx$ 7.8-8% | ZnSe: 25 nm |
| ZCMS 432B | ZnSe (001) 8 x 4 x 1.7 mm | ZnSe: 0.9 $\mu$ m | 17.5 ML Mn $\approx$ 7.3% | ZnSe: 25 nm |
| ZCS 925 | GaAs (001) 20 x 20 x 0.5 mm | ZnSe: 1.1 $\mu$ m | 16 ML Mn = 0% | ZnSe: 25 nm |
| ZCMS 926 | GaAs (001) 30 x 20 x 0.5 mm | ZnSe: 1.0 $\mu$ m | 16 ML Mn $\approx$ 8.0% | ZnSe: 85 nm |

The thickness of the buffer ($d_{buff}$) is chosen clearly above the critical thickness ($d_{crit}$) to achieve relaxed barrier with no strain in it. ML is the abbreviation of mono-atomic layer. A ML equals to 0.281 nm for this epitaxy. The well layer embedded between buffer and cap layer is grown pseudomorphically and has compressive strain. Mn concentration has been calibrated by energy-dispersive X-ray spectroscopy (EDX) on ZnMnSe-epilayers grown with the same partial pressures. The chosen thickness of the cap layer of 25 nm is a least empirical value that ensures the stable formation of a type I quantum well structure as well as a strong enough magnetic fringe field in the well layer in the case of hybrid structure.

The sample ZCMS 431B (see figure 3.1) with transparent ZnSe substrate is used to make the DMSQW-FM hybrid structure, which allows us to perform both photoluminescence (PL) and transmission studies (see section 3.2). On top of the sample, an iron/terbium (Fe/Tb) ferromagnet (FM) consisting of 30 bilayers of 3.5 nm Fe and 1.9 nm Tb was deposited yielding a total height of 162.0 nm. To prevent oxidation of the FMs, the Fe/Tb multilayers were covered by 5 nm chromium (Cr). The patterned FMs are fabricated by electron beam lithography of a mask, thermal evaporation of the FM constituents in ultrahigh vacuum and lift-off technique. Both wire and antidot areas with a total size of 200 $\mu$m $\times$ 200 $\mu$m are made. Figures 3.2 and 3.3 show the scanning electron microscope (SEM) images for wire and

Dieses Werk ist copyrightgeschützt und darf in keiner Form vervielfältigt werden noch an Dritte weitergegeben werden.
Es gilt nur für den persönlichen Gebrauch.

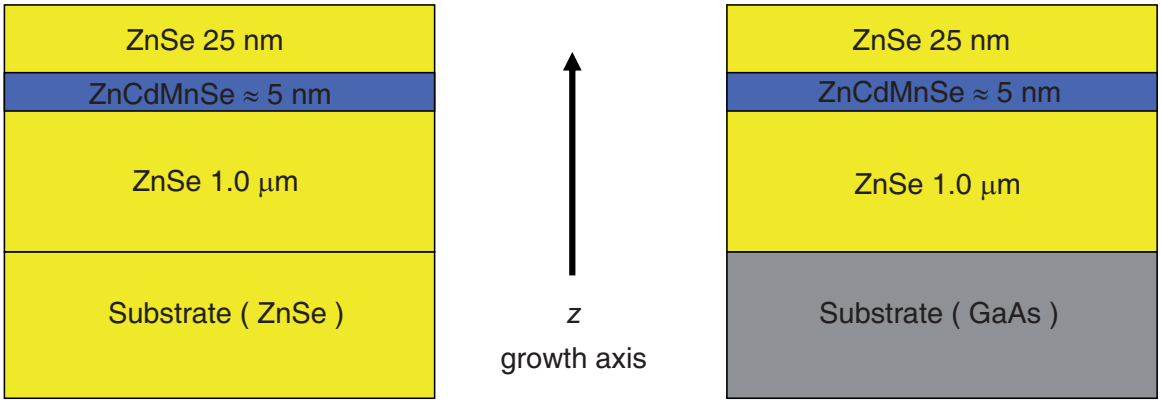


Figure 3.1: ZnSe-based DMSQW sample stacks on ZnSe or GaAs substrate
Samples of both series have the same epitaxial ordering. The relevant substrate and approximate thickness of each layer are displayed along the growth direction in the illustrations.

anti-dot structures, respectively. Wire arrays consist of slender bands with a width of 1200 nm and a period of 2000 nm in sample plane. Anti-dot arrays have 1000 nm × 1000 nm square apertures in the FM with a period of 2000 nm in row and column directions. The structured part of sample surface is partly covered by FM, whose fraction is 60% for wires and 75% for anti-dots, respectively. The total height of the FM is smaller than the lateral dimensions. The ratio of FM height to cap layer thickness is designed to optimize the out-of-plane component of magnetic fringe field at the DMS layer [56].

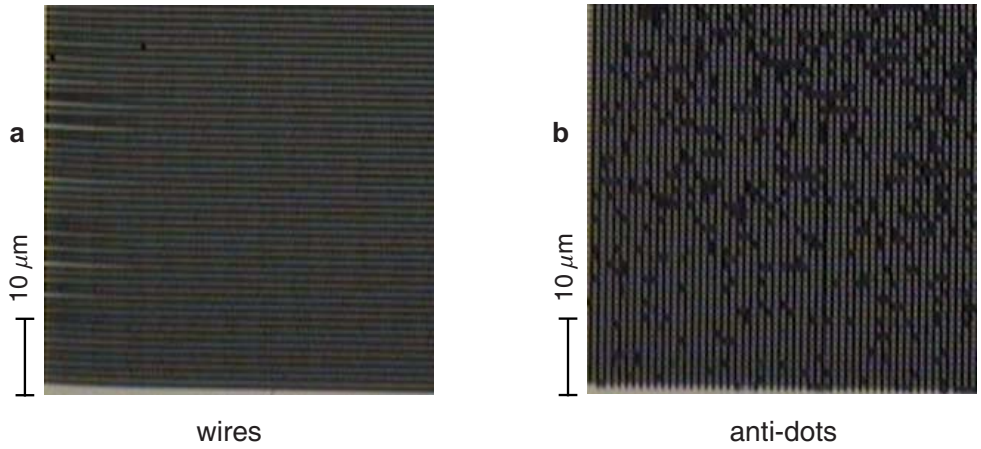


Figure 3.2: SEM images of a part of a patterned field
The white stripes and apertures indicate the places where no FM covers the DMS in the case of wires and anti-dots, respectively. Only 1/4 of the total area of the real square feature of 200 $\mu$m × 200 $\mu$m is shown here.

Dieses Werk ist copyrightgeschützt und darf in keiner Form vervielfältigt werden noch an Dritte weitergegeben werden.
Es gilt nur für den persönlichen Gebrauch.

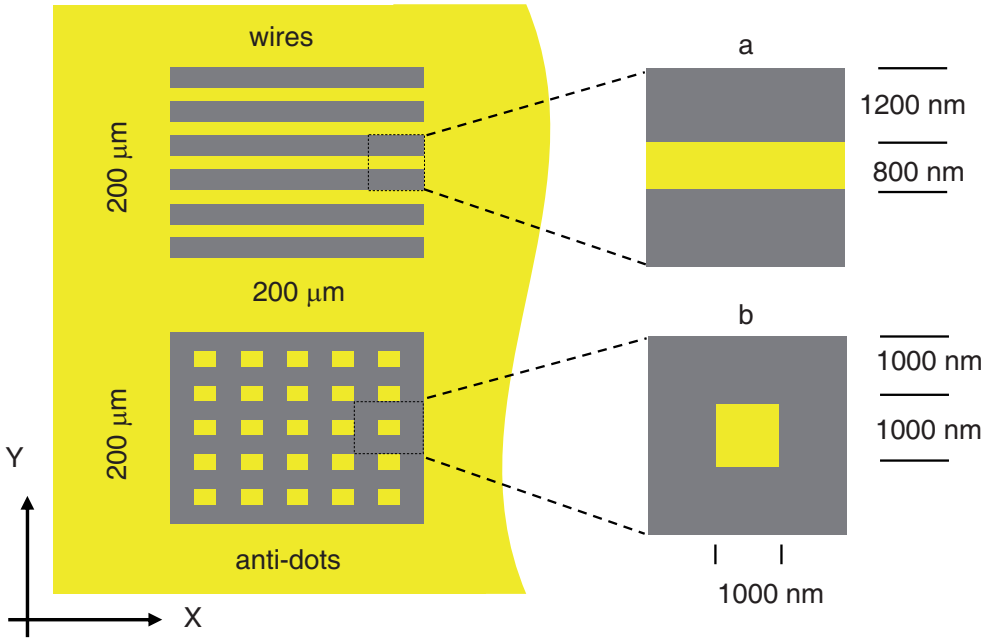


Figure 3.3: Schematic wire and anti-dot patterns on DMS
The DMSQW sample has been patterned by two types of 200 $\mu$m $\times$ 200 $\mu$m square masks, namely wires (a) and anti-dots (b) arrays. A set of enlarged array placed at the right panel illustrates the nanoscaled pattern in a macroscopic view.

Since the Fe/Tb thin films exhibit perpendicular magnetic anisotropy (PMA) [57–59], it obeys a remanent out-of-plane magnetization which creates a vertical magnetic fringe field component at the position of the DMS well (see figure 3.4).

After applying an external magnetic field $\vec{B}_{ext}$ along sample growth direction $z$, the FM is magnetized and $\vec{M}_{FM}$ is parallel to $\vec{B}_{ext}$. Optical access beneath the FMs is only possible for ZnSe substrate or after removing of the GaAs substrate [60]. On the other hand, access is always possible for regions not covered by FM material (i.e. apertures). As illustrated in figure 3.4, the vertical component of $\vec{B}_{fr}$ from FM is always anti-parallel to $\vec{M}_{FM}$ here.

### 3.1.2 ZnO-based epilayer samples

Due to the transparent sapphire ($Al_2O_3$) substrate, all samples can be studied in transmission geometry, too. Sample designs can be seen in table 3.2 and the growing sequences are illustrated in figure 3.5 schematically.

Dieses Werk ist copyrightgeschützt und darf in keiner Form vervielfältigt werden noch an Dritte weitergegeben werden.
Es gilt nur für den persönlichen Gebrauch.

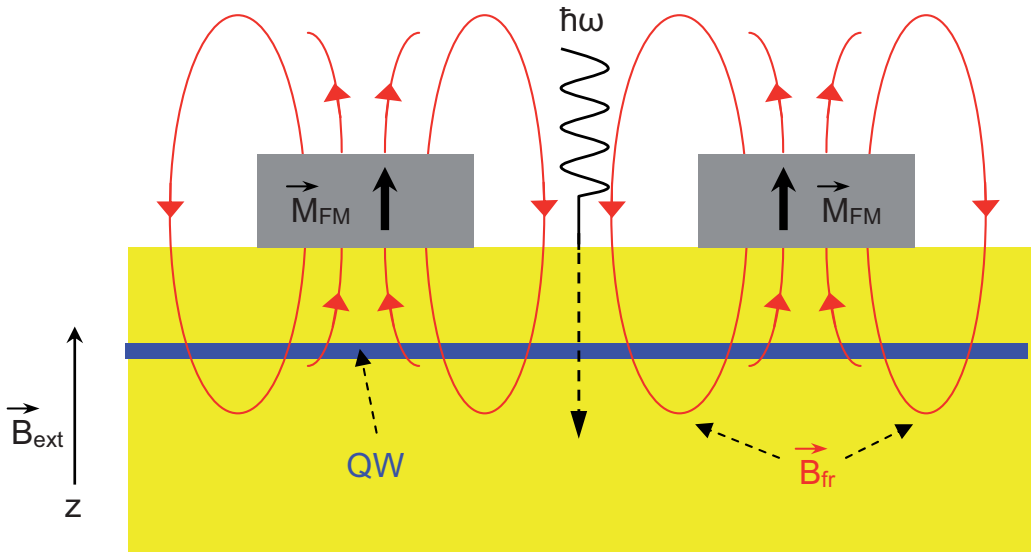


Figure 3.4: Schematic illustration of the magnetic fringe field ($\vec{B}_{fr}$: red curves) stemming from out-of-plane magnetization of FM ($\vec{M}_{FM}$)

Table 3.2: Specification of ZnO-based epilayer samples

| **DMS epilayer samples (epilayer: ZnMnO)** | | | |
|---|---|---|---|
| Serial number of sample | Buffer layer | Thickness of Epilayers (approximation) | Mn concentration (approximation) |
| ZMO 09 | ZnMgO | 600 nm | 0% |
| ZMO 141 | ZnMgO | 600 nm | 0.41% |
| ZMO 142 | ZnMgO | 650 nm | 0.78% |

All $Zn_{1-x}Mn_xO$ epilayer samples are grown on *a*-plane sapphire by MBE. Mn concentration can be determined by analysis of EDX spectra. $Zn_{1-x}Mn_xO$ is also used here to study the exchange interaction of *bulk-like* material in reflectivity.

In figure 3.5, the sample design for epilayer is shown. The sample growth direction is along the *c*-axis of ZnO crystal. ZnMnO is grown homogeneously on thin layer ZnMgO. Without Mn in the epilayer, this structure forms a non-magnetic epilayer sample.

Dieses Werk ist copyrightgeschützt und darf in keiner Form vervielfältigt werden noch an Dritte weitergegeben werden.
Es gilt nur für den persönlichen Gebrauch.

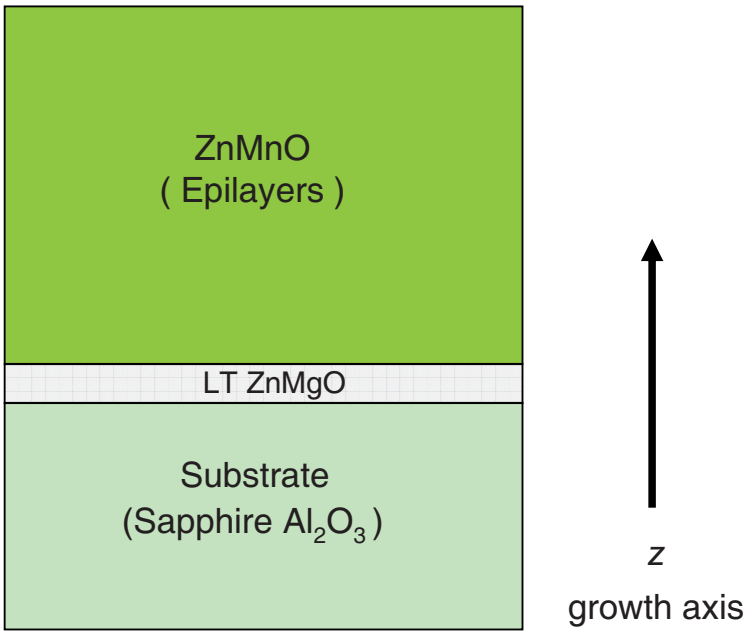


Figure 3.5: Sample stacks for ZnO-based epilayer nanostructures

## 3.2 Measurement techniques

To investigate the magneto-optical properties of the above described DMS samples, we applied the standard experimental techniques: PL, reflectivity measurement, and transmission method. The external magnetic field is produced by a split coil superconducting electromagnet, which is immersed inside a liquid helium bath in a cryostat (magnet cryostat of Oxford Research System) with optionally longitudinal (Faraday geometry) or transverse (Voigt geometry) magnetic field operating from 0 to 12 Tesla.

### 3.2.1 Standard requirement for transmittance and reflectivity

The equipments of measurements for reflectivity and transmittance can be seen in figures 3.7 and 3.8. Due to a particular UV spectral range for ZnO-based samples, optical components made from quartz are strictly demanded. In addition, a strong light source (Tungsten lamp) is required in order to have sufficient probing intensity. An UG-11 filter is applied to block the visible range in order to reduce stray light from this range.

Dieses Werk ist copyrightgeschützt und darf in keiner Form vervielfältigt werden noch an Dritte weitergegeben werden.
Es gilt nur für den persönlichen Gebrauch.

### 3.2.2 Photoluminescence technique

For obtaining the PL, samples are conventionally excited with a photon energy above the energy of the ground state exciton or even above the barrier band gap in the case of QW samples. The PL signal is separated into $\sigma^+$- and $\sigma^-$-component by a combination of $\lambda/4$ retarder and linear polarizer in Faraday configuration [61]. The orientation of applied magnetic field is parallel to the sample growth direction and also to the observation (see figure 3.6).

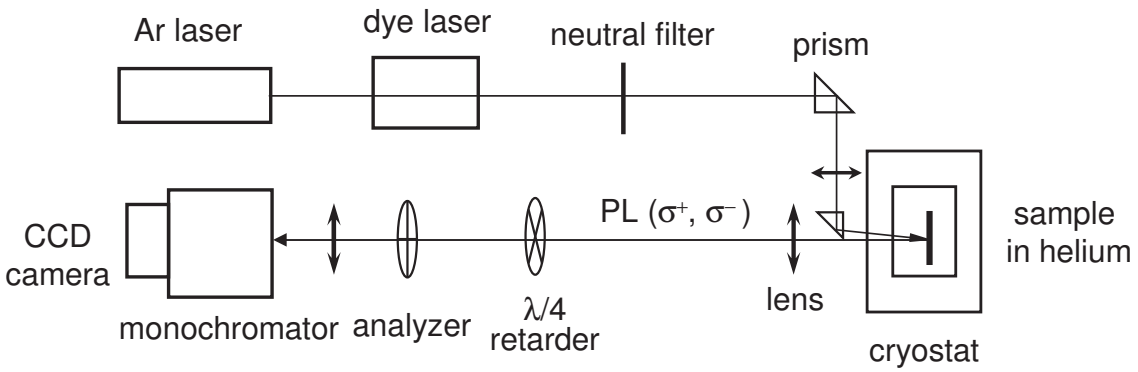


Figure 3.6: Experimental setup for photoluminescence measurement

As shown in figure 3.6, a DMS sample is mounted in helium bath in the sample chamber of the magnet cryostat. An external pump connected to sample chamber keeps evacuating helium vapour (i.e. reducing the vapour pressure) during the measurement to reduce the temperature to 1.5 K, which is below the $\lambda$ point of helium. A tunable cw dye laser with Stilbene 3 pumped by a UV multi-line output of a Ar-ion laser is used to excite the ZnSe-based samples below or above the ZnSe barrier band gap. For measurements with excitation above barrier band gap, a semiconductor laser diode ($\hbar\omega_{ex} = 2.824$ eV) is alternatively used, which provides higher intensity stability than the dye laser.

Since no tunable cw laser is available in the UV spectral range of interest for ZnO, more effort was necessary to produce excitation light for the ZnO-based structures. The 2nd harmonic of the mode-locked Nd:YVO4 laser at 532 nm is used to pump synchronously a mode-locked dye laser with DCM and Pyridine 2, respectively. The output pulses with a width of some ps and a repetition rate of 80 MHz are then frequency-doubled in a BBO crystal to get tunable excitation from 310 ... 365 nm (4.00 ... 3.40 eV).

Dieses Werk ist copyrightgeschützt und darf in keiner Form vervielfältigt werden noch an Dritte weitergegeben werden.
Es gilt nur für den persönlichen Gebrauch.

Two right-angle prisms and a focusing lens are inserted in the optical path of incidence. Neutral filters are used to vary the excitation intensity in a range of four orders of magnitude. The maxima intensity $I_0$ is adjusted to 15W/cm$^2$ by a chosen spot diameter of 300 $\mu$m. For the measurement of the sample ZCMS 431B, the semiconductor laser is used. The laser spot on this sample should not exceed 200 $\mu$m (see figure 3.3). The patterned side of the sample faces to the laser beam to collect the PL only from the apertures in the FM. The PL is collected by a lens. Signals are measured by a liquid nitrogen cooled charge coupled device (CCD) camera connected to a monochromator which disperses the signals by a grating. Data acquisition is carried out by personal computer linked to CCD camera permanently.

### 3.2.3 Reflectivity measurement

To determine the magnetic field dependence of the A and B excitonic resonances, reflectivity measurements (see figure 3.7) are carried out on $Zn_{1-x}Mn_xO$-epilayer samples.

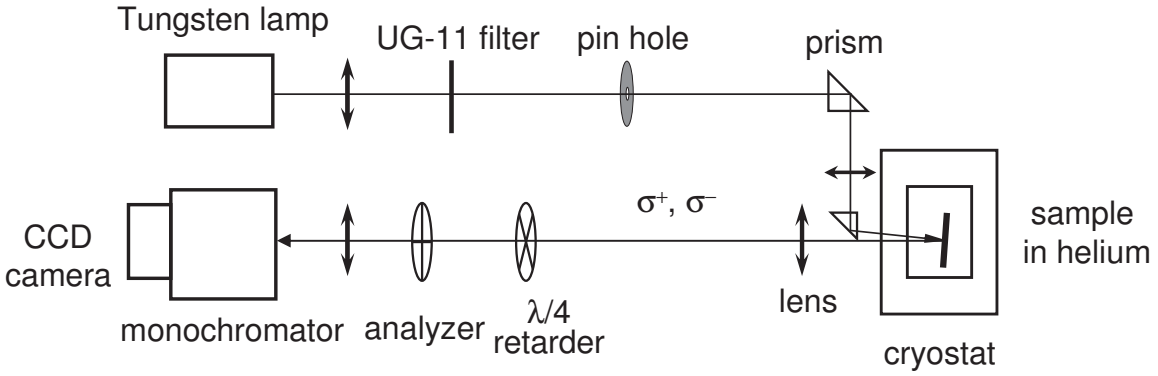


Figure 3.7: Experimental setup for reflection measurement

The sample is fixed vertically on the sample holder in the cryostat that the incident light beam from Tungsten lamp is nearly parallel (tilt angle $\approx 2^\circ$ ) to the sample growth direction ($\vec{k} \perp \vec{z}$). Since the polarization $\vec{E}$ is perpendicular to $\vec{z}$, only a very small contribution ($\approx w^2$ in equation 2.6) from C-exciton is expected in this geometry. For a stronger tilted incidence, an increased contribution to the reflectivity spectrum is expected [21]. The UV part of the spectrally broad white light from Tungsten lamp is extracted by using a colour filter UG-11 that allows the light with photon energy from 3.2 to 3.8 eV to pass. To get the homogeneous light profile, a small pin

Dieses Werk ist copyrightgeschützt und darf in keiner Form vervielfältigt werden noch an Dritte weitergegeben werden.
Es gilt nur für den persönlichen Gebrauch.

hole is fixed behind the UG-11 filter. The detection of the reflected signal is the same as in the case of PL measurement. The signals of $\sigma^+$ and $\sigma^-$ are measured at 1.5 K with an applied magnetic field from 0 to 6 T.

Using Maxwell's equations as boundary conditions for normal incidence at the interface [53], we get the Fresnel's formulae for reflection coefficient $r$ and transmission coefficient $t$ at the interface between two materials

$$\begin{aligned} r &= \frac{\widetilde{n_I} - \widetilde{n_{II}}}{\widetilde{n_I} + \widetilde{n_{II}}} \qquad & t &= \frac{2\,\widetilde{n_I}}{\widetilde{n_I} + \widetilde{n_{II}}} \\ R &= |r|^2 & T &= \frac{\widetilde{n_{II}}}{\widetilde{n_I}}|t|^2 \qquad \text{with} \quad R + T = 1 \end{aligned} \tag{3.1}$$

where $\widetilde{n_I}$ ($\widetilde{n_{II}}$ ) is the complex refractive index of medium I (II), $R$ and $T$ the reflectivity and transmittance, respectively.

The epilayer samples have a thickness of about 600 nm and a second interface between $Zn_{1-x}Mn_xO$ and sapphire substrate. Therefore, the apparent attenuation due to light absorption by propagation and the Fabry-Perot-like interference from the reflection of the first and the second interfaces has to be taken into account.

### 3.2.4 Faraday rotation method

The transmission measurement is a standard technique to determine the absorption coefficient of a transparent medium from solid states or liquids. Neglecting Fabry-Perot effects, the change of light intensity can be represented by $I = I_0\, e^{-\alpha\,(\omega)\,d}$. The absorption maximum occurs normally around the resonance frequency of an oscillator (i.e. excitons for our situation). Thus, the exciton resonances of semiconductor can be determined from ordinary transmission spectra. However, this is not sufficient to cover the magneto-optical properties in detail for weak absorption and damping large compared to the energy shift of excitons. Faraday rotation method can reveal the magneto-optical characters for DMS samples more precisely [62, 63]. The plane of a linear polarized light will be rotated by the different resonance energies of $\sigma^-$ and $\sigma^+$ polarized excitons under the influence of magnetic

Dieses Werk ist copyrightgeschützt und darf in keiner Form vervielfältigt werden noch an Dritte weitergegeben werden.
Es gilt nur für den persönlichen Gebrauch.

field. The rotation is due to the phase difference between the transmitted $\sigma^-$- and $\sigma^+$-components and can be expressed by

$$\Theta_{FR}(w) = \frac{c\,l}{\omega} \cdot \mathrm{Re}[n_-(w) - n_+(w)]\,, \tag{3.2}$$

where $\Theta_{FR}$ is the rotation angle, $\omega$ angular frequency, $l$ thickness of medium, Re the real part, $n_\pm$ complex refraction index of $\sigma_\pm$. The signals can be detected with the setup shown in figure 3.8.

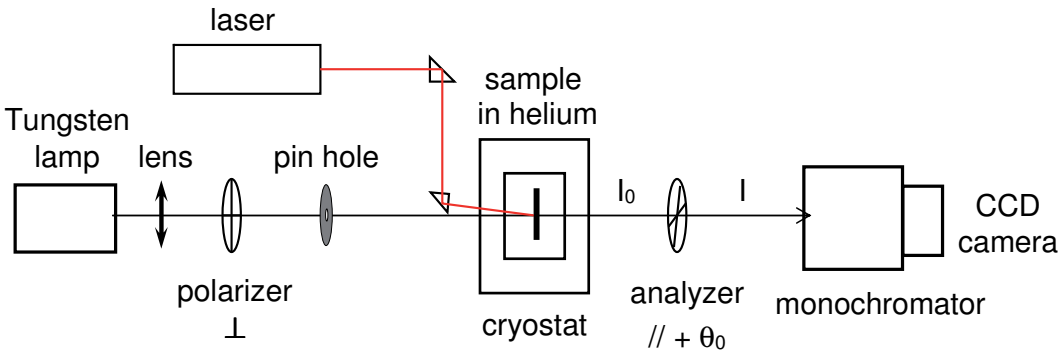


Figure 3.8: Experimental setup for Faraday rotation method

The linearly polarized light from Tungsten lamp propagates through the transparent DMS samples. For the sample with patterns, the light spot should be again smaller than 200 $\mu$m. The pin hole is used here for making a spot diameter of $< 200$ $\mu$m on structured sample surface. The analyzer is settled in crossed direction to the polarizer with a small offset angle $\theta_0 \approx 2.4°$. Any magnetic-field induced rotation results in a change of the detected signal *I:*

$$I = I_0 \cdot \sin^2(\theta_0 + \Theta_{FR}), \tag{3.3}$$

where $\Theta_{FR}$ is the angle of Faraday rotation and $I_0$ the incident intensity.

For the experiments with a short intense heating of FMs, a pulsed dye laser with a photon energy $E_{ex} \approx 2.1$ eV is applied additionally as seen in the higher part of the sketch.

Dieses Werk ist copyrightgeschützt und darf in keiner Form vervielfältigt werden noch an Dritte weitergegeben werden.
Es gilt nur für den persönlichen Gebrauch.

# Chapter 4

# Experimental Results and Discussions

A characterization of the studied ZnSe-based samples by PL at low temperature in magnetic fields is given in the first part of this chapter. Varying the excitation intensities on Zn(Cd,Mn)Se QW samples, the heating of the Mn spin system via photo-excitation has been studied. The spin temperature $T_s$ is determined by fitting the magnetic field dependence of the exciton energy with the Brillouin 5/2 functions (see section 2.4.1).

For the hybrid structures, i.e. patterned FMs on (Zn,Cd,Mn)Se QWs, the FM stray field (fringe field) is derived from PL and FR measurement in external magnetic field and compared to calculated fields. In the center of interest is the manipulation of the remanent FM magnetization by a single laser pulse. The change of FM magnetization is detected by the FR caused by the FM stray field.

$Zn_{1-x}Mn_xO$-epilayers with $x \leq 0.01$ are studied by reflectivity spectra to determine the s,p-d exchange integrals $N_o\alpha$ and $N_o\beta$.

## 4.1 Sample properties

PL properties of $(Zn_{1-x-y}Cd_yMn_x)Se$ QWs are characterized by magneto-optical data such as energy shift $\Delta E$ of the exciton ground state, polarization degree $\rho$, and quantum yield $\eta$ as defined by



Dieses Werk ist copyrightgeschützt und darf in keiner Form vervielfältigt werden noch an Dritte weitergegeben werden.
Es gilt nur für den persönlichen Gebrauch.

$$\begin{cases} \rho = (I_{\sigma^+} - I_{\sigma^-})/(I_{\sigma^+} + I_{\sigma^-}) \,, \\ \eta = I_{\sigma^+} + I_{\sigma^-} \,. \end{cases} \tag{4.1}$$

$I_{\sigma^+}$ and $I_{\sigma^-}$ are the intensities of $\sigma^+$- and $\sigma^-$-polarized PL, respectively.

To optimize the effective $g$-factor of excitons in DMS, the Mn concentration $x$ is chosen close to the maximum of $x_{eff}$ as shown in figure 4.1.

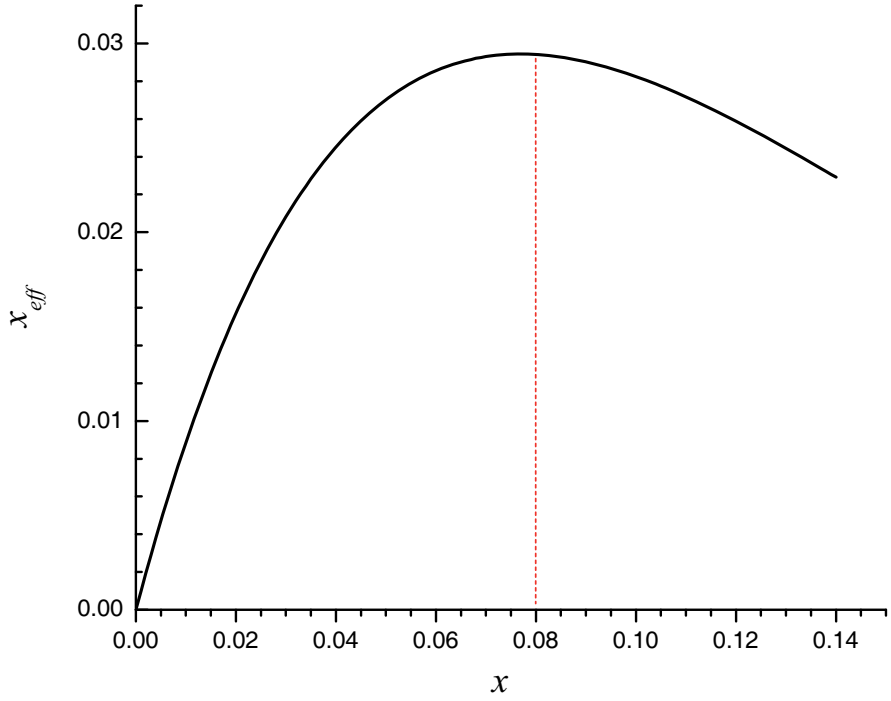


Figure 4.1: Effective concentration of single Mn ions $x_{eff}$ versus Mn total concentration $x$ (equation 2.17). The dash line corresponds to $x = 0.08$.

In figure 4.2, PL spectra in the range of the heavy-hole exciton are represented for a sample on GaAs substrate with a nominal $x = 0.08$. The PL is excited by a GaInN laser diode. The excitation photon energy $E_{ex}$ and the intensity $I_{ex}$ of laser are chosen properly for the DMSQW sample. The intensity of PL for $\sigma^+$-component raises rapidly while that for $\sigma^-$-component attenuates very quickly by increasing magnetic field. This leads to a highly circularly polarized PL. A small difference between $I_{\sigma^+}$ and $I_{\sigma^-}$ at zero magnetic field resulting in a non-vanished polarization degree stems from a small remanence of the magnet cryostat (see section 4.3.1). The $\sigma^-$ part completely disappears at magnetic fields above 0.5 T. For comparison, the PL

Dieses Werk ist copyrightgeschützt und darf in keiner Form vervielfältigt werden noch an Dritte weitergegeben werden.
Es gilt nur für den persönlichen Gebrauch.

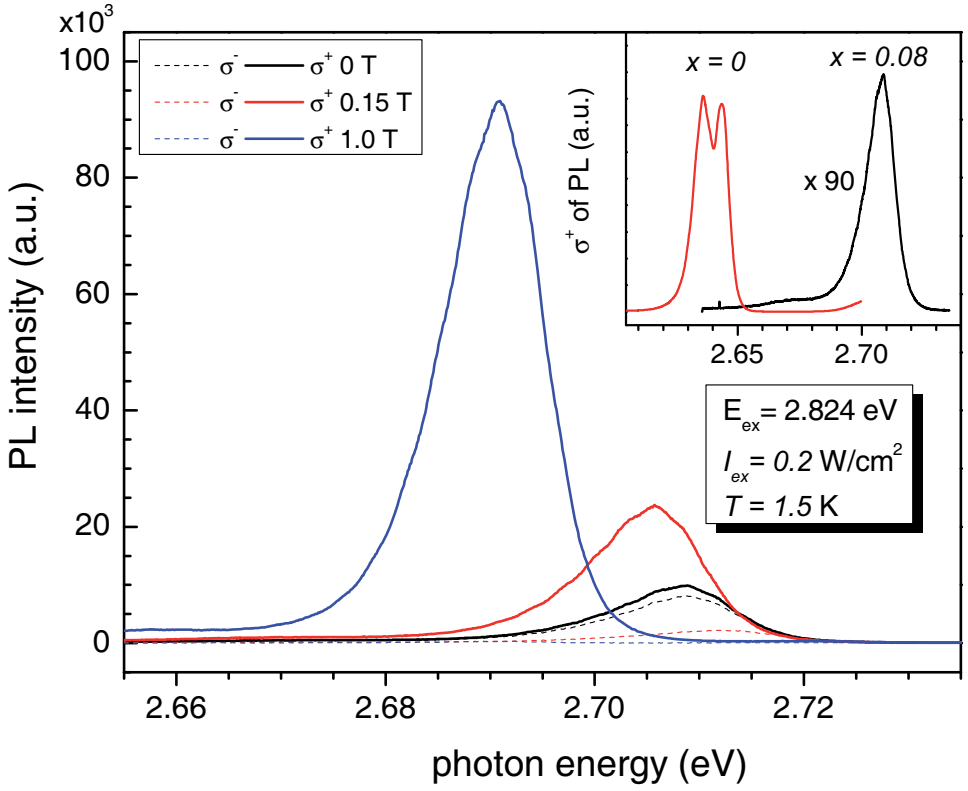


Figure 4.2: Circularly polarized light intensities at 0 T, 0.15 T, and 1.0 T for ZCMS 926 on GaAs substrate. Inset is the $\sigma^+$ signals for ZCS 925 ($x = 0$, left) and ZCMS 926 ($x = 0.08$, right) measured at 0 T, respectively.

spectra of a sample without Mn ($x = 0$) and practically the same Cd content $y = 0.15$ is shown in the inset. The PL intensity is approximately 100 times stronger under the same measuring condition. An effective $g$-factor $\tilde{g}$ can be determined from the energy shift of $\sigma^+$-component (i.e. $\Delta E_{\sigma^+}$) with

$$\tilde{g}\mu_B B = 2\Delta E_{\sigma^+}. \tag{4.2}$$

In figure 4.3, the exciton energy shift due to giant Zeeman effect is given in the uppermost panel. The applied magnetic field induces the down and up energy shift for $|+1>$ and $|-1>$ excitons which are coupled to $\sigma^+$ and $\sigma^-$ polarized light, respectively [64] (see section 2.5). A large $\tilde{g} \approx 600$ is deduced at low magnetic fields ($B < 1$ T). For $B > 1$ T, only the $\sigma^+$-component is seen as shown in figure 4.2. The degree of polarization in middle panel increases quickly in the low magnetic field and reaches saturation with $\rho = 1$ at $B = 1$ T. As mentioned before, a finite $\rho \approx 0.08$ for $B = 0$ T due to remanence of the external magnet is found. In the lower panel, the quantum

Dieses Werk ist copyrightgeschützt und darf in keiner Form vervielfältigt werden noch an Dritte weitergegeben werden.
Es gilt nur für den persönlichen Gebrauch.

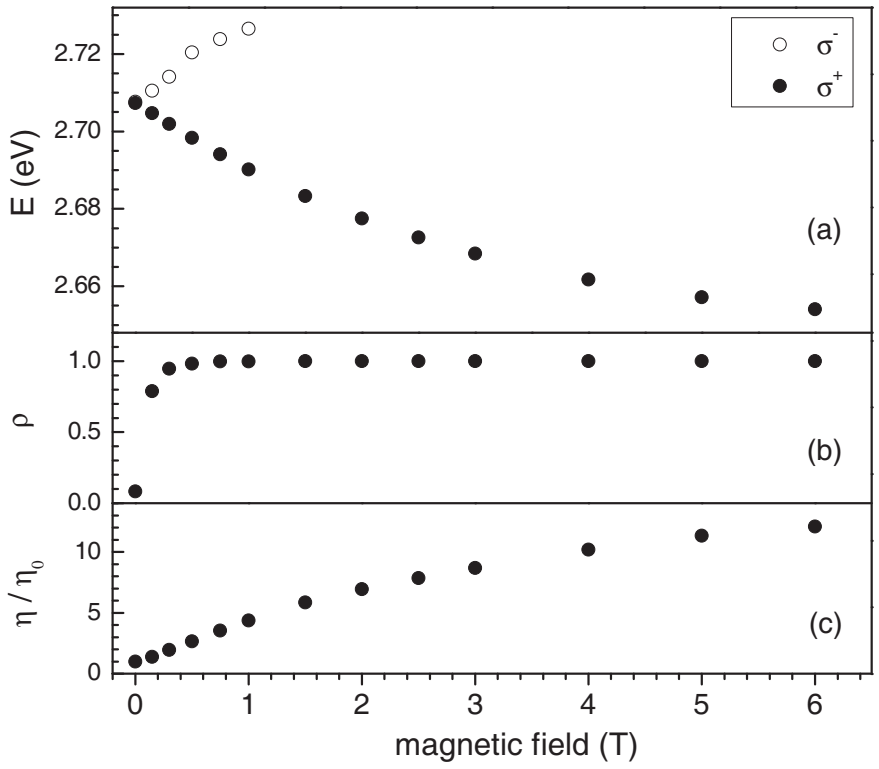


Figure 4.3: Magneto-optical data for $Zn_{1-x-y}Cd_yMn_xSe/ZnSe$ DMSQW sample with $x = 0.08$. The magnetic-field dependent Zeeman splitting (a), polarization degree (b), and the quantum yield related to zero field (c) are shown.

yield normalized to the value at $B = 0$ T is shown. It grows with increasing magnetic field. At $B = 6$ T, $\eta/\eta_0 \approx 12$ is reached, which means that the yield is still eight times smaller than the yield of the non-magnetic QW sample. The data in figure 4.3 prove that the polarization degree $\rho$ is the most sensitive PL feature to detect magnetic fields in mT range.

The thermal population of the split exciton spin sublevels prefers $\sigma^+$ PL component. The polarization degree can be given by [44]

$$\rho(B) = \frac{\tau_d}{\tau_d + \tau_s} \tanh\left(\frac{\Delta E(B, T_{Mn})}{2k_B T_X}\right), \tag{4.3}$$

where $T_{Mn}$ is the Mn temperature, $T_X$ the temperature of thermalized excitons, and $\Delta E$ the energy splitting. From $\rho \approx 1$ at $B > 1$ T, it follows that the exciton spin relaxation time $\tau_s$ is much shorter than the exciton lifetime $\tau_d$.

Dieses Werk ist copyrightgeschützt und darf in keiner Form vervielfältigt werden noch an Dritte weitergegeben werden.
Es gilt nur für den persönlichen Gebrauch.

$\Delta E/2k_BT_X$ reaches values much larger than unity already in the 100 mT range ($k_B$T = 0.13 meV at T = 1.5 K), which explains the strong $\rho(B)$ dependence in the mT range.

The time resolved PL in figure 4.4 is helpful to explain the magnetic field dependence of PL intensity of $Zn_{1-x-y}Cd_yMn_xSe$/ZnSe QW samples. The upper panel describes a non-magnetic QW. Typical lifetime of II-VI exciton at 1.5 K is $\tau_d \approx 100$ ps, which is dominated by the radiative process [65]. The lower panel represents the PL decay of the exciton for DMSQW with $\tau_d < 3$ ps and $\approx 10$ ps at $B = 0$ T and 3 T, respectively. For DMS samples, the exciton decays via Auger process by exciting inner Mn transition, which is well studied in the literature [66, 67]. The resulting quantum yield is low at small magnetic fields. For increasing $B$, Auger transfer becomes partly blocked by spin selection rules. The resulting exciton lifetime ($\tau_d \approx 10$ ps) is still too short to allow for magnetic polaron formation. In PL studies, the optically excited heavy-hole exciton samples directly the Mn spin in the present DMSQW samples.

Dieses Werk ist copyrightgeschützt und darf in keiner Form vervielfältigt werden noch an Dritte weitergegeben werden.
Es gilt nur für den persönlichen Gebrauch.

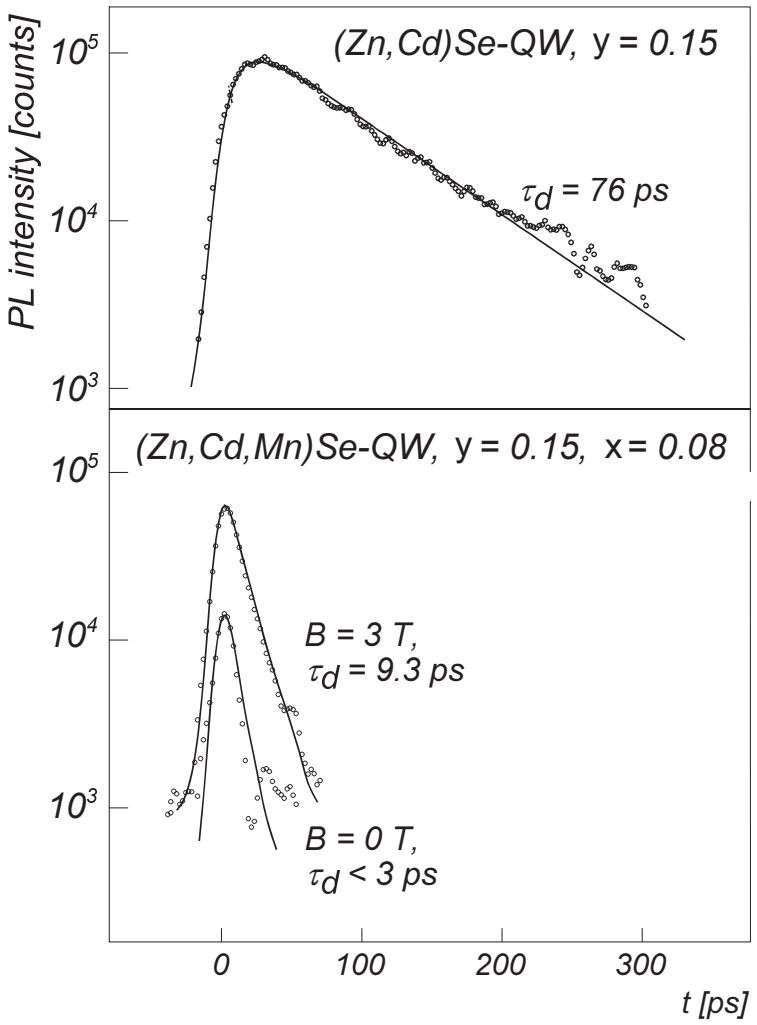


Figure 4.4: Time-resolved PL for non-magnetic and diluted magnetic QW samples. The derived exciton lifetimes $\tau_d$ are given.

The magneto-optical properties of DMSQWs on GaAs substrate will now be compared with the data of two samples (ZCMS 431B, 432B) grown on ZnSe substrate for application in the hybrid structures. The nominal Mn content is again $x = 0.08$. The panels in figure 4.5 show the magnetic-field dependent circularly polarized PL measured at 1.5 K. The dashed line at the bottom indicates the zero level. The $\sigma^-$ PL at $B = 0.5$ T shows a contribution which does not obey the giant Zeeman shift. This background is therefore not related to the DMSQW but stems, according to the spectral range [68], from donor-acceptor pair recombination in the ZnSe barriers. The effective $g$-factor $\tilde{g}$ and polarization degree $\rho$ are listed in table 4.1 for both samples.

The data prove that the DMSQWs on ZnSe have comparable magneto-optical properties as DMSQW grown on GaAs substrate. The sample ZCMS

Dieses Werk ist copyrightgeschützt und darf in keiner Form vervielfältigt werden noch an Dritte weitergegeben werden.
Es gilt nur für den persönlichen Gebrauch.

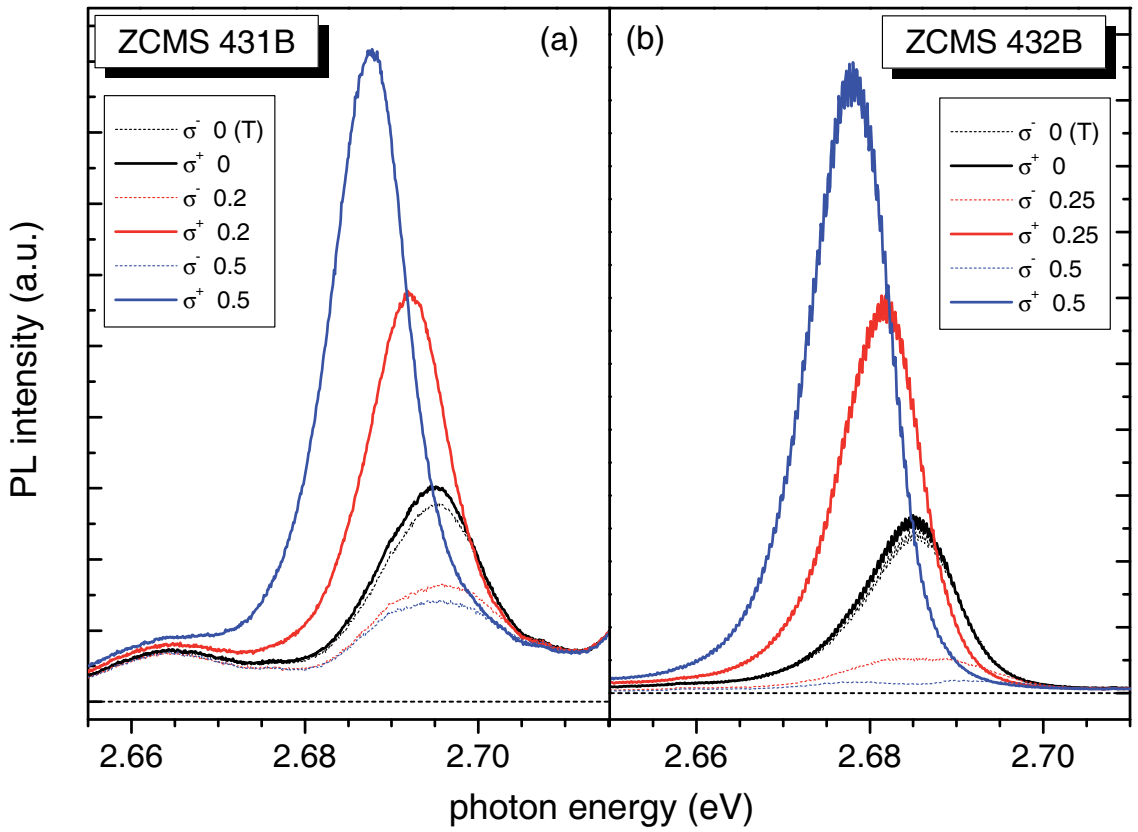


Figure 4.5: Circularly polarized PL intensity for sample ZCMS 431B (a) and ZCMS 432B (b), respectively. Spectra are measured at different magnetic fields denoted in black, red, and blue colours.

Table 4.1: $\tilde{g}$ and $\rho$ for ZCMS 431B and 432B measured at 1.5 K at different magnetic fields

| ZCMS 431B | | | ZCMS 432B | | |
|---|---|---|---|---|---|
| B (T) | $\tilde{g}$ | $\rho$ | B (T) | $\tilde{g}$ | $\rho$ |
| 0.5 | 520 | 85% | 0.5 | 460 | 84% |
| 1.0 | 520 | 98% | 1.0 | 460 | 1 |

431B with larger $\tilde{g}$ is used for the hybrid structure. The sample ZCMS 432B, with much less contribution from donor-acceptor pairs in the ZnSe barrier, is used here to examine the heating mechanism of the Mn spin system.

Dieses Werk ist copyrightgeschützt und darf in keiner Form vervielfältigt werden noch an Dritte weitergegeben werden.
Es gilt nur für den persönlichen Gebrauch.

## 4.2 Heating of the Mn spin system by photo-excitation

### 4.2.1 Heating by photo-excitation

The sample ZCMS 432B is used to study Mn spin heating by photo-excitation using variable excitation intensities $I_{ex}$. The excitation energies are 2.803 eV and 2.756 eV ($E_{ex} < E_{g,ZnSe} \approx 2.820$ eV). Since ZCMS 432B is grown on transparent ZnSe substrate, the transmitted excitation light in the latter case will not be absorbed by substrate and only photons absorbed in the QW contribute to the heating. The sample is mounted in the superfluid helium bath with temperature of $T_b = 1.5$ K and the measurement is carried out in magnetic fields from 0 to 6 Tesla in Faraday geometry. The magnetic-field induced energy shift of $\sigma^+$ PL maximum is given in figures 4.6 and 4.7.

In figure 4.6, the sample is excited with five different excitation intensities $I_{ex}$ with $E_{ex} = 2.803$ eV. This is close to the barrier exciton energy $E_{X,b}$, which yields practically total absorption in barrier and QW. The field-induced energy shift decreases with increasing $I_{ex}$ due to heating of Mn spin.

For figure 4.7, four curves $\Delta E(B)$ are given for excitation photon energy $E_{ex} < E_{X,b}$. The heating is obviously reduced. From the marginal changes between the data for $0.01I_0$ and $0.001I_0$, it can be concluded that the heating becomes negligible at $I_{ex} \leq 0.01$ W/cm$^2$, where $T_s = T_b = 1.5$ K holds.

The low-energy shift of the $|+1>$ excitons caused by the s,p-d interaction can be described by equations 2.20 and 2.21 to derive the temperature $T_s + T_0$ as listed in table 4.2. It should be noted that the fits in figures 4.6 and 4.7 are done with the nominal Mn content $x$, which describes the observed Zeeman splitting correctly. No further fitting parameter is used.

From $T_s \approx T_b$ at the lowest $I_{ex}$ in figure 4.7, the value of the phenomenological $T_0 \approx 1.6$ K is obtained for the present sample. The value is marginally smaller than a $T_0 \approx 1.9$ K found for a (Zn,Mn)Se/(Zn,Be)Se QW with about $x = 0.06$ Mn concentration [44] and a $T_0 = 2.5$ K for a (Zn,Mn)Se epilayer with $x = 0.08$ [69].

Dieses Werk ist copyrightgeschützt und darf in keiner Form vervielfältigt werden noch an Dritte weitergegeben werden.
Es gilt nur für den persönlichen Gebrauch.

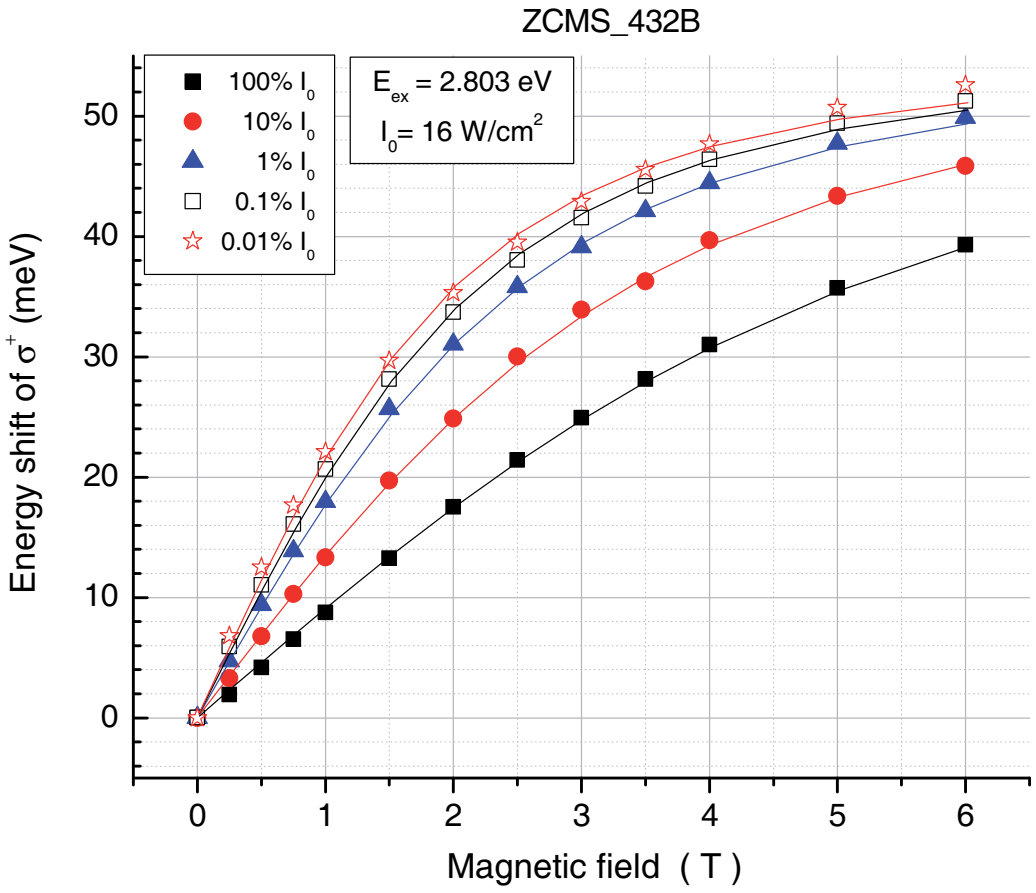


Figure 4.6: Magnetic-field induced energy red shift of $\sigma^+$ PL for different excitation intensities with $E_{ex} = 2.803$ eV. Solid curves are fits of data for induced energy shift by using modified Brillouin 5/2 function (see equations 2.20 and 2.21).

Table 4.2: The deduced temperature $(T_s + T_0)$ for two different excitation energies and varied $I_{ex}$ for sample ZCMS 432B.

| $E_{ex} = 2.803$ eV $I_0 = 16$ W/cm$^2$ | $100\%I_0$ | $10\%I_0$ | $1\%I_0$ | $0.1\%I_0$ | $0.01\%I_0$ |
|---|---|---|---|---|---|
| $T_s + T_0$ ( K ) | 9.1559 | 6.06284 | 4.51582 | 3.94782 | 3.60991 |
| | | | | | |
| $E_{ex} = 2.756$ eV $I_0 = 13$ W/cm$^2$ | $100\%I_0$ | $10\%I_0$ | $1\%I_0$ | $0.1\%I_0$ | |
| $T_s + T_0$ ( K ) | 4.91715 | 3.74161 | 3.33454 | 3.1415 | |

Dieses Werk ist copyrightgeschützt und darf in keiner Form vervielfältigt werden noch an Dritte weitergegeben werden.
Es gilt nur für den persönlichen Gebrauch.

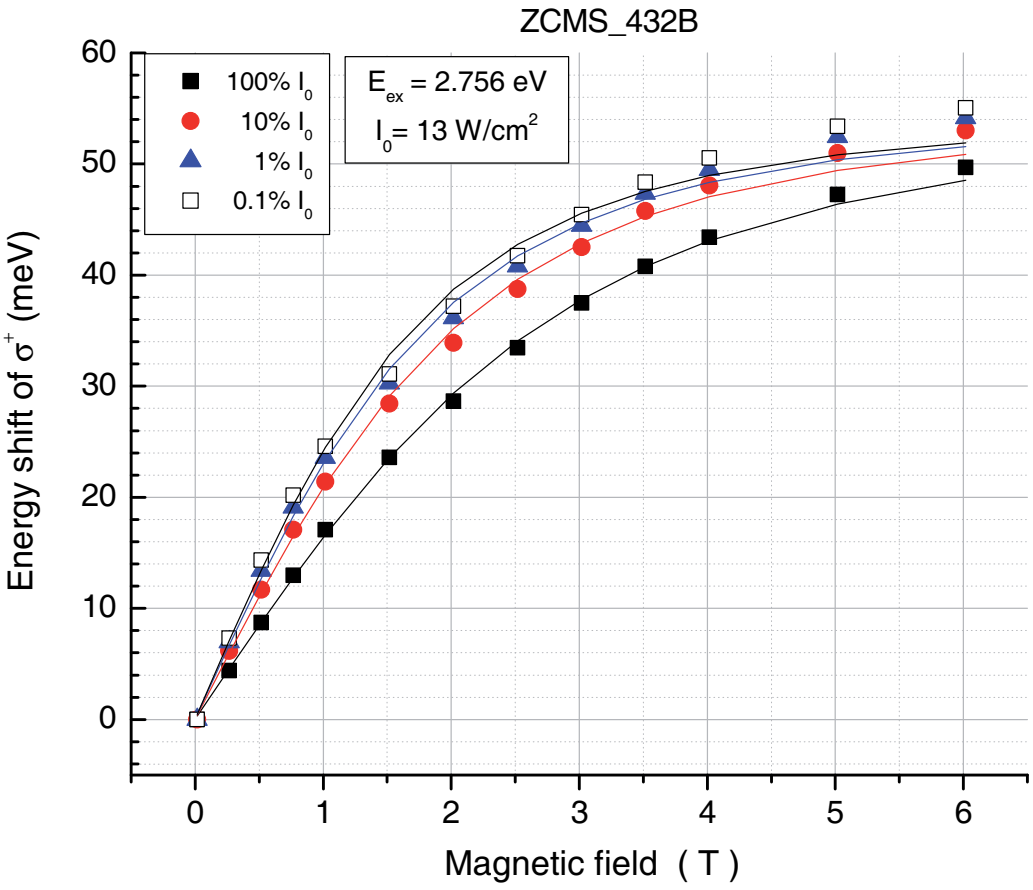


Figure 4.7: Magnetic-field induced energy decrease of $\sigma^+$ PL with $E_{ex} = 2.756$ eV. Four solid curves are fits of data again.

### 4.2.2 Debye model $\lambda \propto T^3$ as thermal transfer mechanism for heating magnetic ions

To decide about the heating mechanism of $Mn^{2+}$ spins from photocarriers, directly or via phonon participation, the Mn spin temperature $T_s$ is drawn versus $I_{ex}$ in a semi-logarithmic plot in figure 4.8. The lattice temperature (i.e. phonon temperature $T_p$) at the position of the DMSQW can be obtained from a one-dimensionally stationary heat transfer problem in the Debye limit [70, 71]:

$$\frac{\partial}{\partial z}\lambda(T)\frac{\partial T}{\partial z} \propto I_{ex}, \tag{4.4}$$

where $\lambda(T)$ is the thermal conductivity.

Dieses Werk ist copyrightgeschützt und darf in keiner Form vervielfältigt werden noch an Dritte weitergegeben werden.
Es gilt nur für den persönlichen Gebrauch.

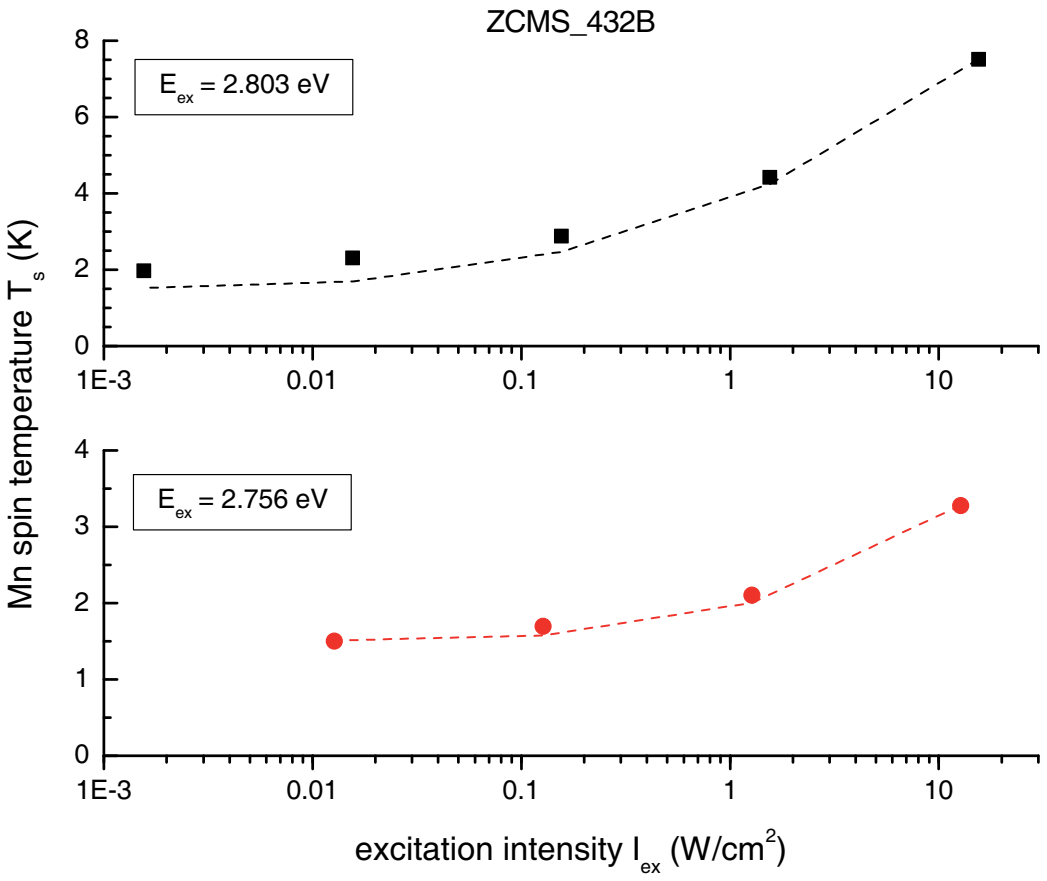


Figure 4.8: Deduced spin temperature $T_s$ for steady photo-excitation for $x \approx 8\%$ versus excitation intensity ($I_{ex}$ in logarithmic scale). Dashed lines are fits of the experimental data by equation 4.5.

Obviously, in figure 4.8, $T_s$ is not linearly dependent on $I_{ex}$, as expected for a spin heating via a direct spin transfer [44]. As seen by the fits, the relation is rather a feature described by

$$T_s^4 - T_b^4 = c \cdot I_{ex} \tag{4.5}$$

with a factor $c$.

This holds for $E_{ex} = 2.803$ and $E_{ex} = 2.756$ eV. The line in the upper panel of figure 4.8 presents a fit with $c_B = 250$ K$^4$cm$^2$/W for barrier excitation ($E_{ex} = 2.803$ eV). The line in the lower panel is the fit for well excitation ($E_{ex} = 2.756$ eV) yielding $c_W = 8.7$ K$^4$cm$^2$/W. The much stronger barrier absorption explains the relationship $c_B > c_W$.

The $T_s^4 - T_b^4 \propto I_{ex}$ relations point to the dominant phonon mediated spin heating in both cases. $T_p$ is established by photo-excitation and heat flow to the substrate. Since the thermal conductivity $\lambda$ is proportional to the heat

Dieses Werk ist copyrightgeschützt und darf in keiner Form vervielfältigt werden noch an Dritte weitergegeben werden.
Es gilt nur für den persönlichen Gebrauch.

capacity $C_V$, which is $\propto T_p^3$ in the Debye limit, the relation (4.5) follows [70]. $T_s$ and $T_p$ are equalized via spin-lattice relaxation.

## 4.3 Evidence of fringe field on DMSQW

The effect of fringe field from the deposited FM structures (wires and anti-dots) are studied on ZnSe-based DMSQW by PL polarization degree and FR. The results are compared with calculated fields in subsection 4.3.3.

### 4.3.1 Experimental results of polarized PL

The FMs are out-of-plane magnetized reaching a saturated magnetization at $B_{ext,z} = +5$ T and -5 T, respectively. After that, the field dependence of $\rho$ is measured in a range -300 mT $\leq B_{ext,z} \leq$ +300 mT. The resulting magnetic field at QW layer is the sum of applied magnetic field $\vec{B}_{ext}$, fringe field $\vec{B}_{fr}$, and a small remanent field $\vec{B}_r$[1].

To prove that the effects stem really from the FMs, measurements are performed also on a reference area without FM patterns. For that pure DMSQW (figure 4.9), $\rho$ reaches $\pm$ 100% at about $\pm$ 300 mT. Correcting the data for the finite $B_r$, the $\rho(B)$ dependence becomes independent on the magnetization history. This shows that there is, as expected, no hysteresis for the pure (Zn,Cd,Mn)Se QW.

[1] A weak $B_r \approx \pm 8$ mT stemming from magnet cryostat is always found after running the magnet at $\pm 5$ T independent on the studied sample.

Dieses Werk ist copyrightgeschützt und darf in keiner Form vervielfältigt werden noch an Dritte weitergegeben werden.
Es gilt nur für den persönlichen Gebrauch.

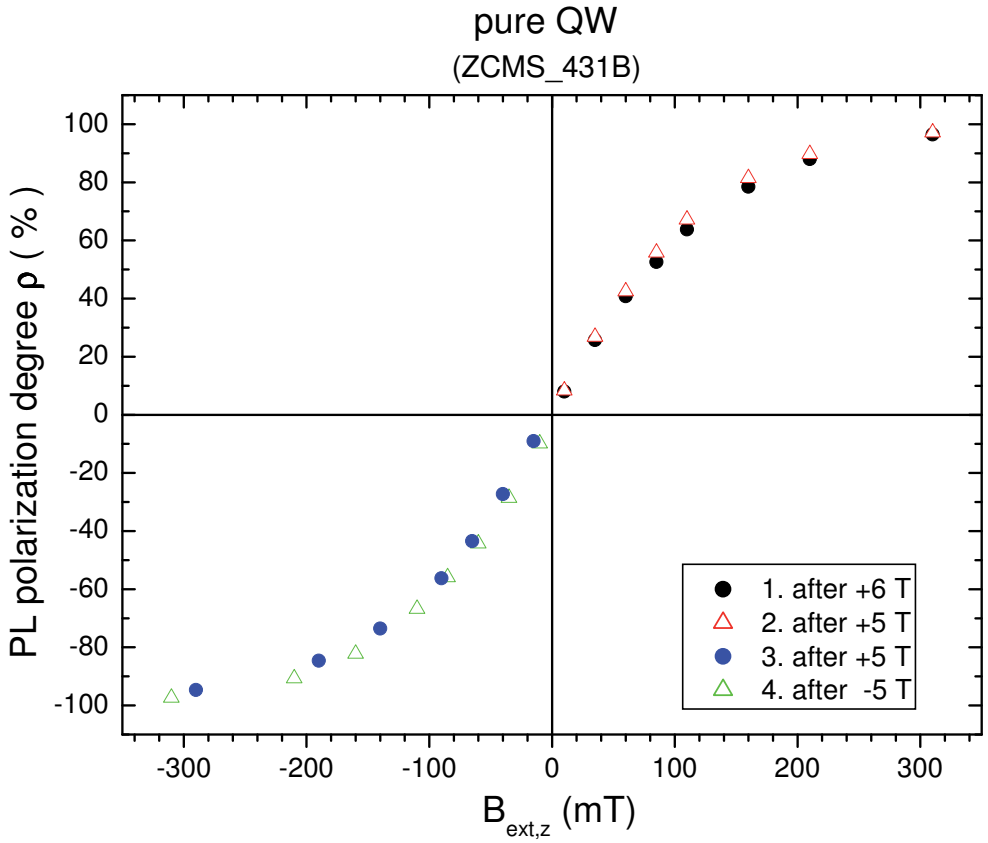


Figure 4.9: The PL polarization degree of pure QW in magnetic field. The number from 1 to 4 represents the sequence of the applied magnetic field. Data are corrected for $\vec{B}_{fr}$.

The data both for the FM wire structure (figure 4.10) and anti-dot structure (figure 4.11) show a clear hysteresis in the $\rho(B)$ dependence stemming from the FM fringe field. At zero $B_{ext,z}$, the remaining value of $\rho$ has an opposite sign to the applied magnetization field, e.g. $\rho < 0$ after $B_{ext,z} = +5$ T, fully in accord with a fringe field oppositely directed to the magnetization of the FM structures in the uncovered, optically accessible sample regions.

In figure 4.10 and 4.11, the zero-field value $\rho_0$ is obtained from interception with ordinate. Values of -28% and -35% are found, which are about two times larger than the value previously measured on such hybrid structures with DMSQW on GaAs substrate [72]. This is a result of a markedly smaller spin temperature realized by the excitation conditions used here. On the reference DMSQW, an external magnetic field of $B_{ext,z} = 35 \ldots 45$ mT is required to achieve the same modulus of $\rho$. In the range of $B_{ext,z} \leq \pm 300$ mT, the remanent magnetization of the FMs $\vec{M}_0$ remains constant. In this case, the interceptions with abscissa yield directly the $z$-component of $B_{fr,z}$ of

Dieses Werk ist copyrightgeschützt und darf in keiner Form vervielfältigt werden noch an Dritte weitergegeben werden.
Es gilt nur für den persönlichen Gebrauch.

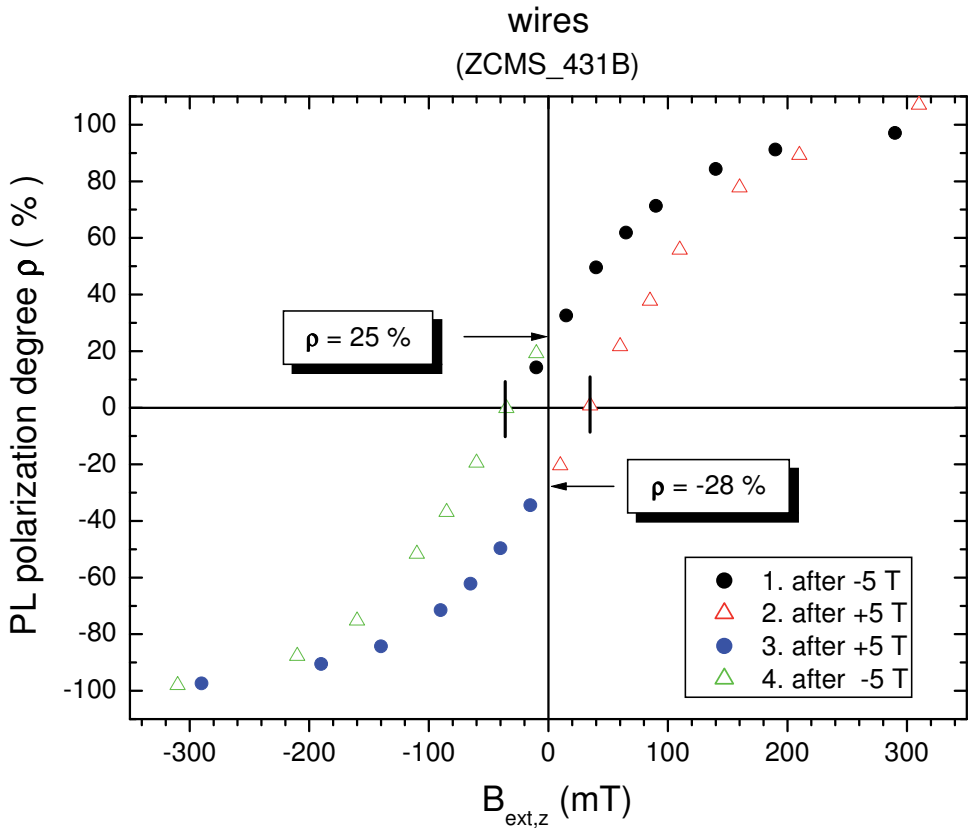


Figure 4.10: The PL polarization degree $\rho$ of wires in magnetic field. The number from 1 to 4 represents the sequence of the applied magnetic field. Data are corrected for $\vec{B}_{fr}$.

approximately 36 and 42 mT for wires and anti-dots, respectively. These values agree fairly well with the above derived values.

Energies of $\sigma^-$- and $\sigma^+$-excitons measured at 0 T for reference DMS, wires, and anti-dots are listed in in table 4.3. The energy shifts found are in accord with the existing $B_{fr,z}$ for the hybrid and the non-existing $B_{fr,z}$ in the reference area. As already discussed, these data are less appropriate than $\rho$ to detect fringe fields in the mT range.

Table 4.3: The energies of $\sigma^-$ and $\sigma^+$ measured at 0 T after applying $\pm$5 T.

| pattern | $E_{\sigma-}$ at 0 mT (after +5 T) | $E_{\sigma-}$ at 0 mT (after -5 T) | $E_{\sigma+}$ at 0 mT (after +5 T) | $E_{\sigma+}$ at 0 mT (after -5 T) |
|---|---|---|---|---|
| pure QW | 2.6952 eV | 2.6952 eV | 2.6952 eV | 2.6952 eV |
| wires | 2.6951 eV | 2.6962 eV | 2.6961 eV | 2.6951 eV |
| anti-dots | 2.6946 eV | 2.6958 eV | 2.6960 eV | 2.6947 eV |

Dieses Werk ist copyrightgeschützt und darf in keiner Form vervielfältigt werden noch an Dritte weitergegeben werden.
Es gilt nur für den persönlichen Gebrauch.

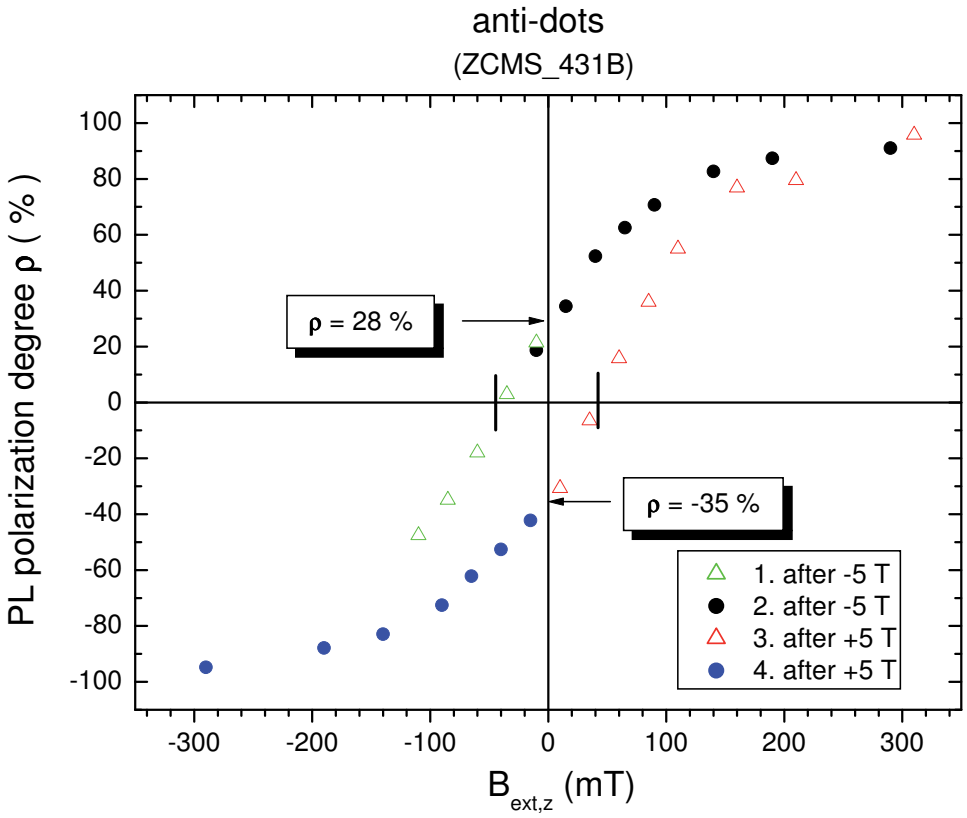


Figure 4.11: The PL polarization degree $\rho$ of anti-dots in magnetic field. The number from 1 to 4 represents the sequence of the applied magnetic field. Data are corrected for $\vec{B}_{fr}$.

### 4.3.2 Experimental results of Faraday rotation

Thanks to the homoepitaxy of the transparent ZnSe-based DMS sample [73], transmission measurement can be applied to the hybrid DMSQW sample. Just as the fringe field of FMs is demonstrated by PL for excitons aligned by Mn spin via s,p-d interaction in section 4.3.1, the Faraday rotation technique is used to verify the fringe field by detecting the splitting of exciton states directly [74]. The resulting difference of phase velocity of right and left circularly polarized light yields the rotation of polarization plane of incident linearly polarized light as described by equation 3.2. Figure 4.12 shows the Faraday rotation angle resulting from the different refraction indices of $\sigma^-$ and $\sigma^+$ polarization schematically. The FR is measured at 1.5 K with experimental setup in Faraday configuration (see section 3.2.4). To increase the sensitivity, the FR is recorded not only for a single photon energy, but in the spectral range of the heavy-hole exciton.

Dieses Werk ist copyrightgeschützt und darf in keiner Form vervielfältigt werden noch an Dritte weitergegeben werden.
Es gilt nur für den persönlichen Gebrauch.

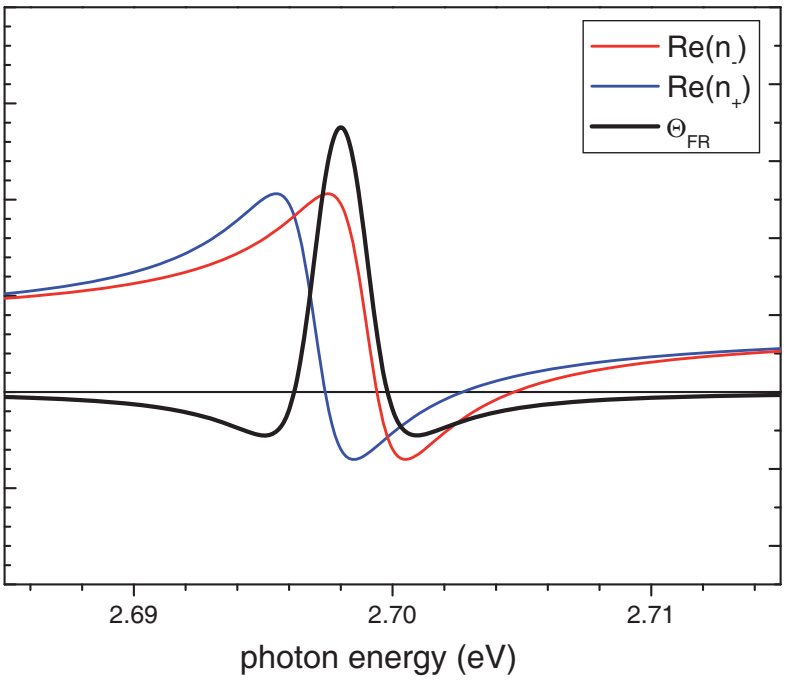


Figure 4.12: Faraday rotation angle $\Theta_{FR}$ (black line) described by equation 3.2 with refraction indices of $\sigma^-$ and $\sigma^+$ polarization, respectively. The horizontal line indicates the zero level for FR signal.

In panel (a) of figure 4.13 , two uppermost curves taken at the reference area exhibit no Faraday rotation as expected. For both curves, a small exciton absorption feature around 2.695 eV is indicated. The FR signals are seen obviously at $B_{ext,z}$ equal to +30 and -30 mT with the typical shape. In panel (b) for wires, significant FR signals are, as expected, found at $B_{ext,z} = 0$ after magnetization of the FM by $B_{ext} = +5$ T and $-5$ T, respectively. Comparing with reference DMSQW area, shape and magnitude of the signal prove to arise from the induced fringe field, oppositely directed to FM magnetization.

A slight asymmetry of the FR curves in figure 4.13 can be attributed to stray light, diffraction effects on the FM patterns, as well as contribution from energetically higher exciton transitions. The stray light value $I_{sc}$ is obtained from the fit in figure 4.14, where $I(\theta)$ is measured for pure QW with vertically polarized incident light. The FR angle $\Theta_{FR}$ is than determined using

$$I(\theta) = I_{sc} + I_0 \cdot \sin^2(\theta_0 + \Theta_{FR}). \tag{4.6}$$

The fit yields $I_{sc} = 0.04$ and $I_0 = 8.84$ for the chosen arbitrary units.

Using equation 4.6 and the known angle of analyzer $\theta_0$, $\Theta_{FR}$ at the maxima of the FR feature are extracted and drawn in 4.15-4.17.

Dieses Werk ist copyrightgeschützt und darf in keiner Form vervielfältigt werden noch an Dritte weitergegeben werden.
Es gilt nur für den persönlichen Gebrauch.

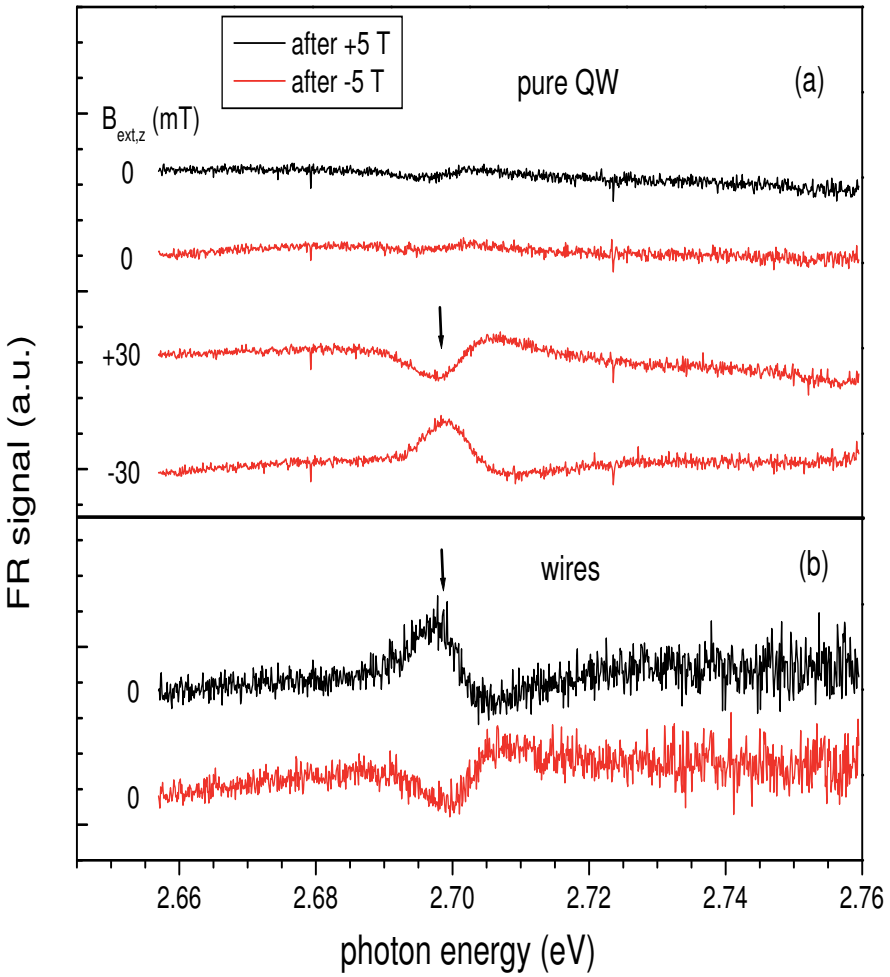


Figure 4.13: FR signals after applying external magnetic field of +5 T (black curves) and -5 T (red curves) for pure QW (a) and wires (b). The arrows show the small absorption of heavy-hole excitons. Arrows mark the spectral position where $\Theta_{FR}$ is extracted for the $\Theta_{FR}(B_{ext})$ relations in figures 4.15 and 4.12.

Figure 4.15 shows the rotation angle measured for the pure QW. Since no $B_{fr,z}$ is present in this area, the rotation angle is determined only by the external magnetic field. This yields a nearly linear dependence $\Theta_{FR}(B_{ext})$ with $\Theta_{FR}(0) = 0$.

As seen in figures 4.16 and 4.17, after applying +5 T, rotation angles of 0.37° for wires and 0.41° for anti-dots can be observed at $B_{ext,z} = 0$. The values of the fringe field follow again from the interception with the abscissa approximately at 40 and 45 mT for wires and anti-dots, respectively. The

Dieses Werk ist copyrightgeschützt und darf in keiner Form vervielfältigt werden noch an Dritte weitergegeben werden.
Es gilt nur für den persönlichen Gebrauch.

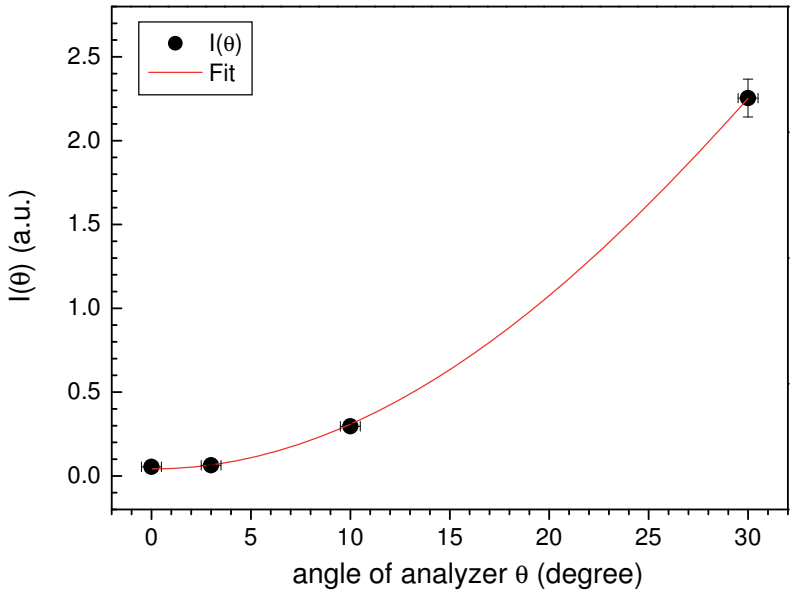


Figure 4.14: The angle-dependent light intensity of transmittance $I(\theta)$ for pure QW and the fit. The fitting curve illustrates the relationship between $I(\theta)$ and $I_{sc}$ described in equation 4.6.

values are fully in agreement with the data obtained from the PL polarization degree studies[2].

### 4.3.3 Calculation of fringe field on DMSQW

The calculation of stray field is according to time-independent Maxwell equation without net currents $\nabla \times \vec{H} = 0$ ($\vec{H}$ magnetic field strength). Thus, a scalar magnetic potential $\phi_{\vec{H}}$ can be defined by $\vec{H} = -\nabla\phi_{\vec{H}}$ [56]. The magnetic fringe field $\vec{B}_{fr}$ can be written as

$$\vec{B}_{fr}(\vec{r}) = \frac{\mu_0}{4\pi} \int \frac{\rho_M(\vec{r'})}{|\vec{r} - \vec{r'}|^3}(\vec{r} - \vec{r'})d^3\vec{r'}, \tag{4.7}$$

where $\rho_M = -\nabla \cdot \vec{M}_0$ is formally the magnetic charge density. $\vec{B}_{fr}(\vec{r})$ can be calculated analytically for a homogeneous magnetized rectangular block, here with $a \leq x \leq b$, $c \leq y \leq d$, and $e \leq z \leq f$.

The direction of magnetization of the present Fe/Tb FM is parallel to the applied magnetic field in Faraday configuration (out-of-plane). This out-of-

[2]The data for $B_{ext,z} > 45$ mT becomes questionable due to the finite accuracy of the determined $I_{sc}$.

Dieses Werk ist copyrightgeschützt und darf in keiner Form vervielfältigt werden noch an Dritte weitergegeben werden.
Es gilt nur für den persönlichen Gebrauch.

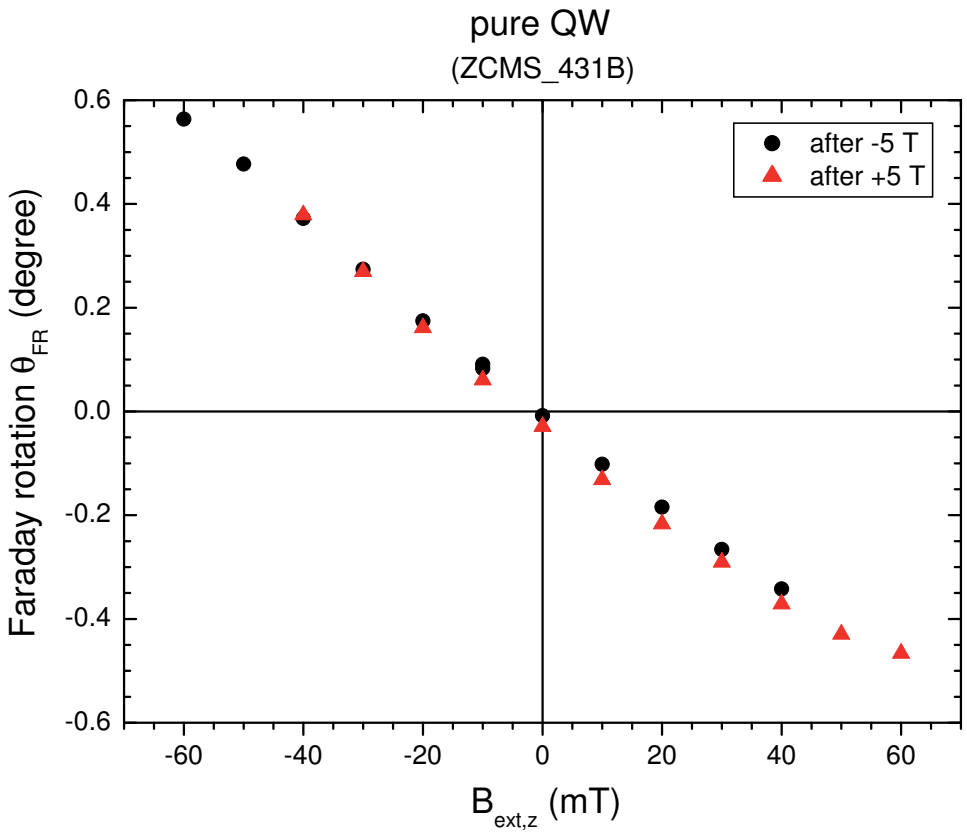


Figure 4.15: The Faraday rotation angle for pure QW derived at 2.6978 eV. Data are corrected for $\vec{B}_{fr}$.

Dieses Werk ist copyrightgeschützt und darf in keiner Form vervielfältigt werden noch an Dritte weitergegeben werden.
Es gilt nur für den persönlichen Gebrauch.

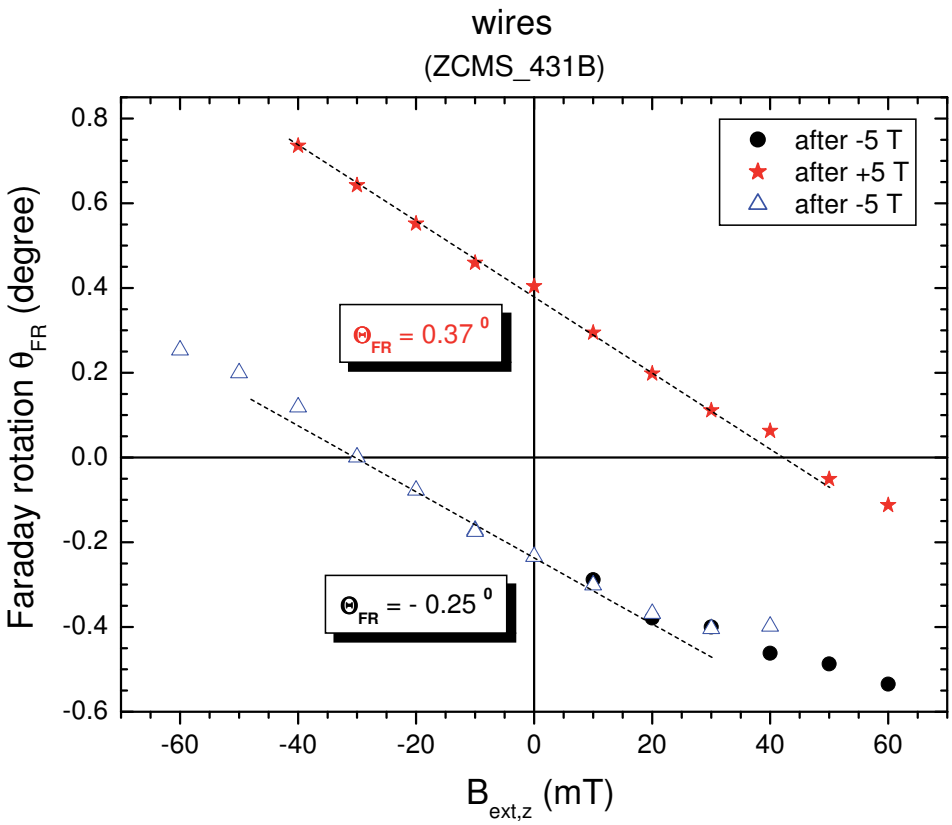


Figure 4.16: The Faraday rotation angle for wire structures derived at 2.6982 eV. Data are corrected for $\vec{B}_{fr}$.

Dieses Werk ist copyrightgeschützt und darf in keiner Form vervielfältigt werden noch an Dritte weitergegeben werden.
Es gilt nur für den persönlichen Gebrauch.

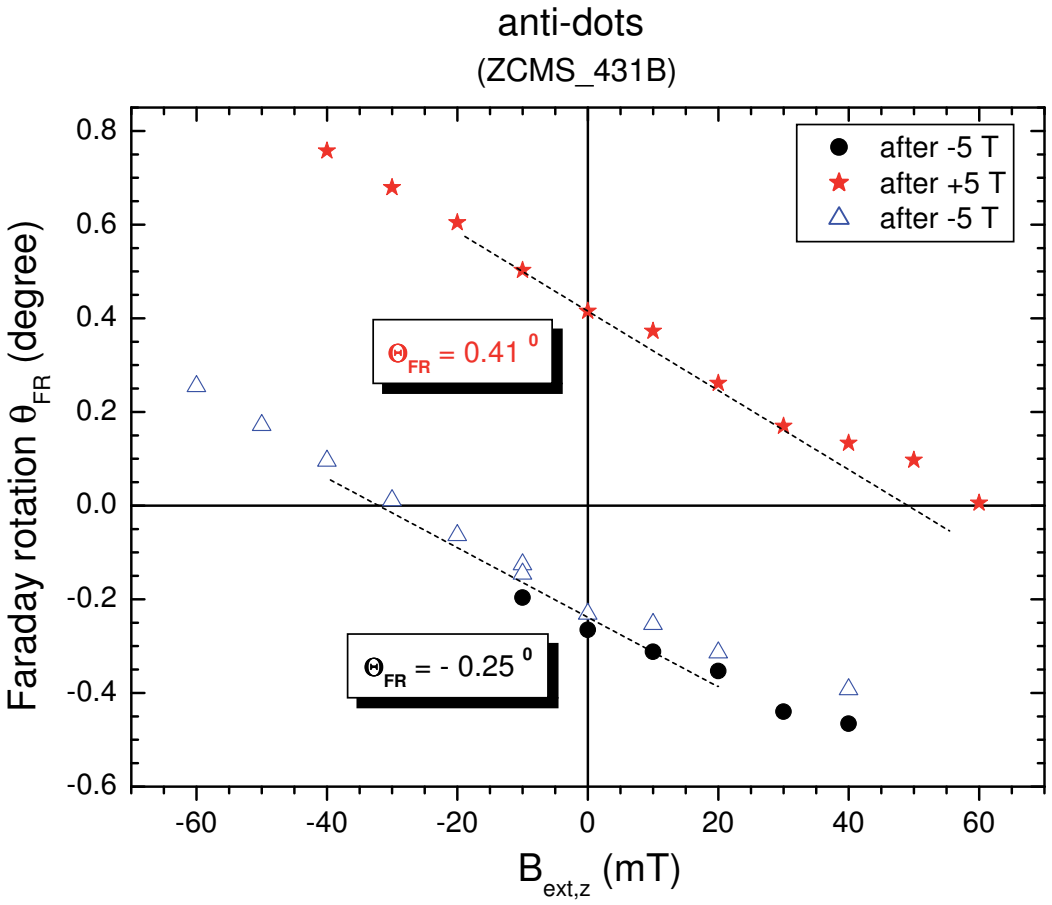


Figure 4.17: The Faraday rotation angle for anti-dot structures derived at 2.6963 eV. Data are corrected for $\vec{B}_{fr}$.

plane magnetization creates both in-plane ($x$-$y$ plane) and out-of-plane fringe fields [75]. $B_{fr,z}$ caused by magnetization $M_z$, can be given by

$$\begin{aligned} B_z(\vec{r}) = & \frac{1}{4\pi}\mu_0 M_z \\ & \cdot \{[f_{bde}(x,y,z) - f_{bdf}(x,y,z)] + [f_{bcf}(x,y,z) - f_{bce}(x,y,z)] \\ & + [f_{adf}(x,y,z) - f_{ade}(x,y,z)] + [f_{ace}(x,y,z) - f_{acf}(x,y,z)]\}, \end{aligned} \tag{4.8}$$

with $f_{\alpha\beta\gamma}(x,y,z) = \tan^{-1}[\frac{(\alpha-x)(\beta-y)}{(\gamma-z)\sqrt{(\alpha-x)^2+(\beta-y)^2+(\gamma-z)^2}}]$. $\mu_0$ is the permeability in vacuum, $M_z$ the magnetization in $z$-direction.

For the designed two patterns, the FM has to be composed of respective blocks, a single one for a wire, four pieces for the anti-dot structure. The periodical arrangement of wires along $x$-direction as well as anti-dot structure along $x$- and $y$-direction is taken into account. Since the fringe field of a single element decreases strongly with increasing $x$ and $y$ distance, only five neighboured elements at each side has to be included in the calculation.

Dieses Werk ist copyrightgeschützt und darf in keiner Form vervielfältigt werden noch an Dritte weitergegeben werden.
Es gilt nur für den persönlichen Gebrauch.

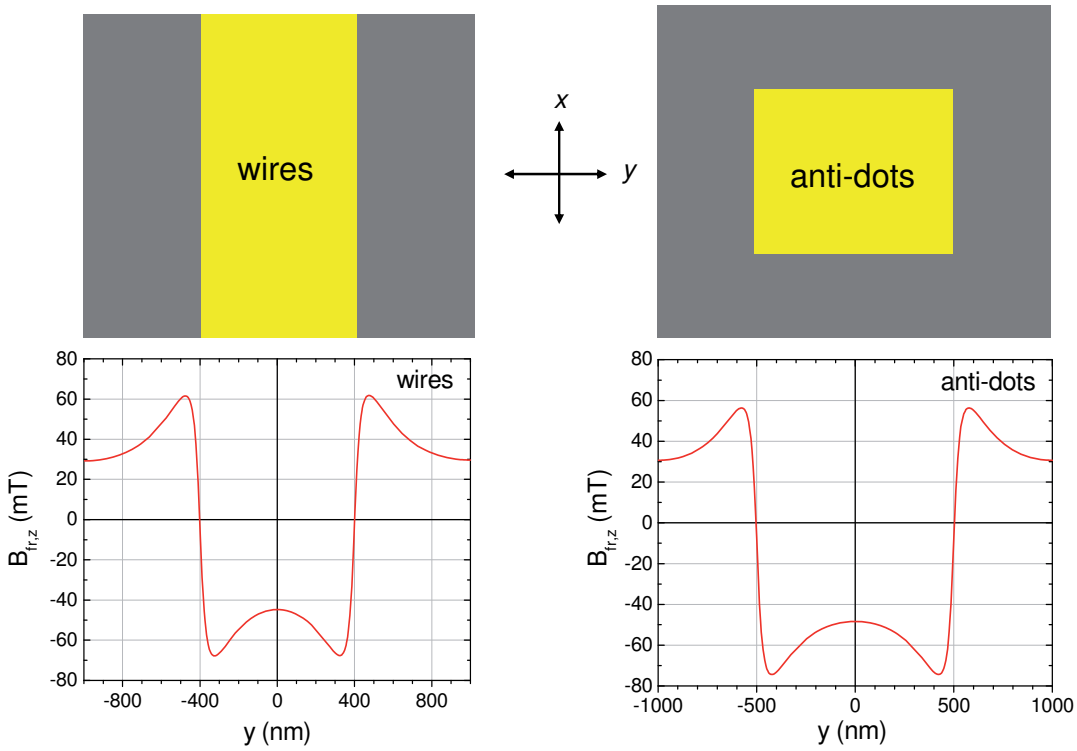


Figure 4.18: The strength variation of $z$-component magnetic fringe fields $B_{fr,z}$ for wires and anti-dots by the attitude $x = 0$ at QW layers.

The FMs induced resulting magnetic fringe field are shown in figure 4.18. The fringe fields between the wires and inside the hole of the anti-dots are negative for positively magnetized FM, i.e. the fringe field in the apertures is always oppositely directed to the magnetization of FMs. A value of $\mu_0 M_z = 470$ mT measured on a reference Fe/Tb film [75] has been used. $B_{fr,z}$ in the center of the apertures for wires and anti-dots are approximately 50 and 55 mT, respectively. These calculated values agree fairly well with the experimental values of $B_{fr,z} \approx 36 \ldots 40$ mT for wires and $\approx 40 \ldots 45$ mT for anti-dots, taking into account the additional patterning of the studied hybrid structures and that the measurements here represent on averaging over a region of 100 $\mu$m $\times$ 100 $\mu$m. The calculated fringe field of anti-dots is larger than that of wires which demonstrates the same tendency as seen in experiment.

Dieses Werk ist copyrightgeschützt und darf in keiner Form vervielfältigt werden noch an Dritte weitergegeben werden.
Es gilt nur für den persönlichen Gebrauch.

## 4.4 Laser-induced manipulation of FM magnetization

Up to now, the Mn spin manipulation via magnetic fringe field of Fe/Tb FMs with out-of-plane magnetization has been confirmed by PL and FR methods. The Faraday rotation technique is used in the following to trace changes of the Fe/Tb multilayer film magnetization.

For the manipulation of the FM magnetization, single pulses from a ns dye laser are applied as shown in figure 3.8. The laser is pumped by an pulsed Excimer laser yielding pulse energies upto 1 mJ at a pulse width of 15 ns. A photon energy of $E_{ex} \approx 2.1$ eV is chosen to avoid a heating in the DMSQW and ZnSe substrate and to apply it only to the FM. The FR for the wire hybrid structure is always measured at $B_{ext} = 0$ T and at $T = 1.5$ K after FM magnetization with $B_{ext}$ and/or application of a single laser pulse with adjustable flux density.

### 4.4.1 Erasure of FM magnetization

The resulting FR spectra are given in figure 4.19. For the uppermost curve, the FMs are completely magnetized at the beginning. For a single pulse with photon flux densities lower than 5mJ/cm$^2$ practical no change of the FR spectra is found. For more than 10mJ/cm$^2$, an increasing erasure of the FM magnetization can be concluded with a practically complete erasure at 16mJ/cm$^2$. After applying -5 T again, the magnetization of the FMs is refreshed resulting in the same fringe field as after first magnetization. This proves that the erasure can be completely reversed by an appropriate $B_{ext}$.

From this result, the thermal heating of the FM by the single laser pulses can be assumed as the origin of the magnetization erasure. To prove that, the expected temperature after the pulse is calculated in dependence on the pulse energy density.

The thermal energy per unit area of the metal stack is derived within the Debye model and plotted in figure 4.20. The Debye temperatures of Fe (470 K), Tb (174 K), and Cr (630 K) [76, 77] and thickness of the different layers in the stack are well known. The magnetic energy can be estimated from $M_o$ and $B_c$ to be $\approx 0.02$ mJ/cm$^2$, which can be safely neglected against the

Dieses Werk ist copyrightgeschützt und darf in keiner Form vervielfältigt werden noch an Dritte weitergegeben werden.
Es gilt nur für den persönlichen Gebrauch.

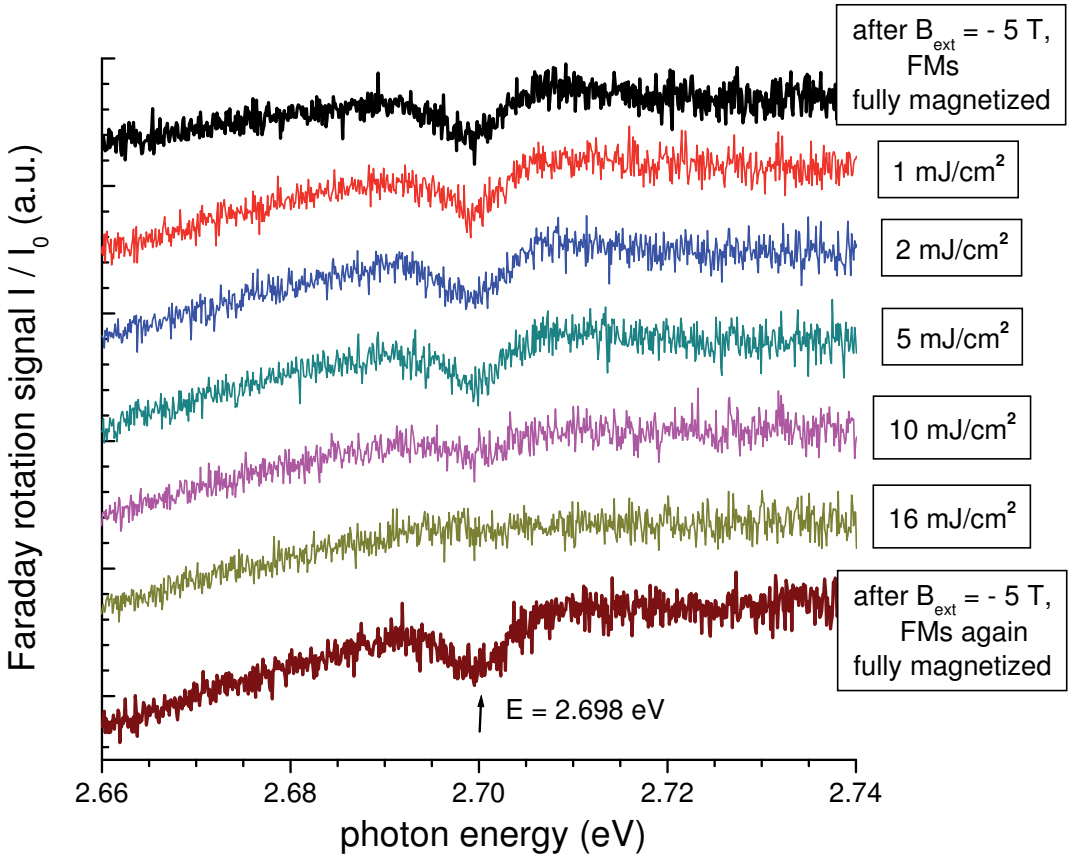


Figure 4.19: Erasure of FM magnetization via single laser pulse. The FR signals are shifted with distinguishable levels.

thermal energy at lattice temperatures $T > 100$ K. From the refraction index of Cr $\tilde{n} \approx 3.21 + 3.30i$ [78], a reflectivity of the stack surface of 0.44 follows. Considering the remaining pulse energy density of 7 mJ/cm$^2$ absorbed in the metal stack, a temperature of 270 K can be deduced. Heat diffusion out of the FM during the pulse duration is neglected in the calculation. This temperature compares well with the Curie temperature of Tb, $T_C = 218$ K, as well as the observed disappearance of the remanent PL polarization on a similar hybrid structure after stationary heating to temperature of 250 to 300 K [72]. Physically, the observed dominant role of heating in the present experiments is related to the pulse with nanosecond duration used. Nonthermal demagnetization of metallic FMs can be expected only on a much shorter time scale [79, 80].

Dieses Werk ist copyrightgeschützt und darf in keiner Form vervielfältigt werden noch an Dritte weitergegeben werden.
Es gilt nur für den persönlichen Gebrauch.

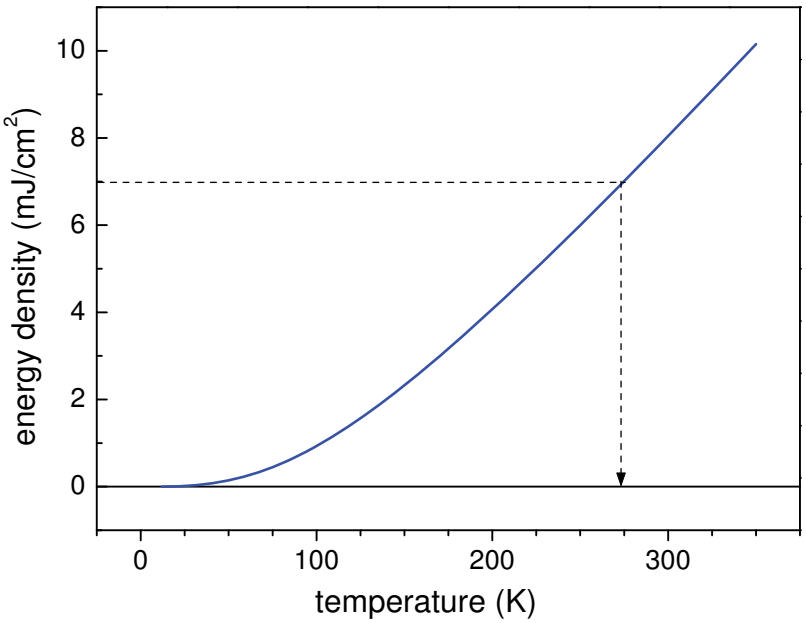


Figure 4.20: Calculated thermal energy per unit area of the FM multilayers vs temperature.

### 4.4.2 Reversal of FM magnetization

Besides the erasing, a reversal of the magnetizations by optical pulses is of special interest. To distinguish the impact of the external field and the optical pulses, a reversed field $B_{ext} = 0.5$ T has been applied at first after FMs fully magnetized. As seen in the next upper curve in figure 4.21, the unchanged heavy-hole exciton resonance feature in the FR spectrum proves the remanence still present since $|B_{ext}| < B_c$ is fulfilled at $T = 1.5$ K.

In the next step, a single laser pulse with again 16mJ/cm$^2$ is applied at $B_{ext} = 0.2$ and 0.5 T. This results in a partial and complete reversing of the FM magnetization of the hybrid structure as seen by the FR feature in the third and fourth curves. The heating pulse enhances the FM temperature reducing coercive field strength $B_c$ below $B_{ext}$. The momentary narrowing of magnetic hysteresis by laser pulse is illustrated in the inset. The trace a $\rightarrow$ b $\rightarrow$ c explains the reversing of FM magnetization under the impact of a laser pulse at a biased field.

This experiment open a way to control spins by optical pulses in a FM-DMSQW hybrid structure. The necessary magnetic bias field remains small against the coercive field strength of the FM and can be generated in principle by integrated microcoils [81].

Dieses Werk ist copyrightgeschützt und darf in keiner Form vervielfältigt werden noch an Dritte weitergegeben werden.
Es gilt nur für den persönlichen Gebrauch.

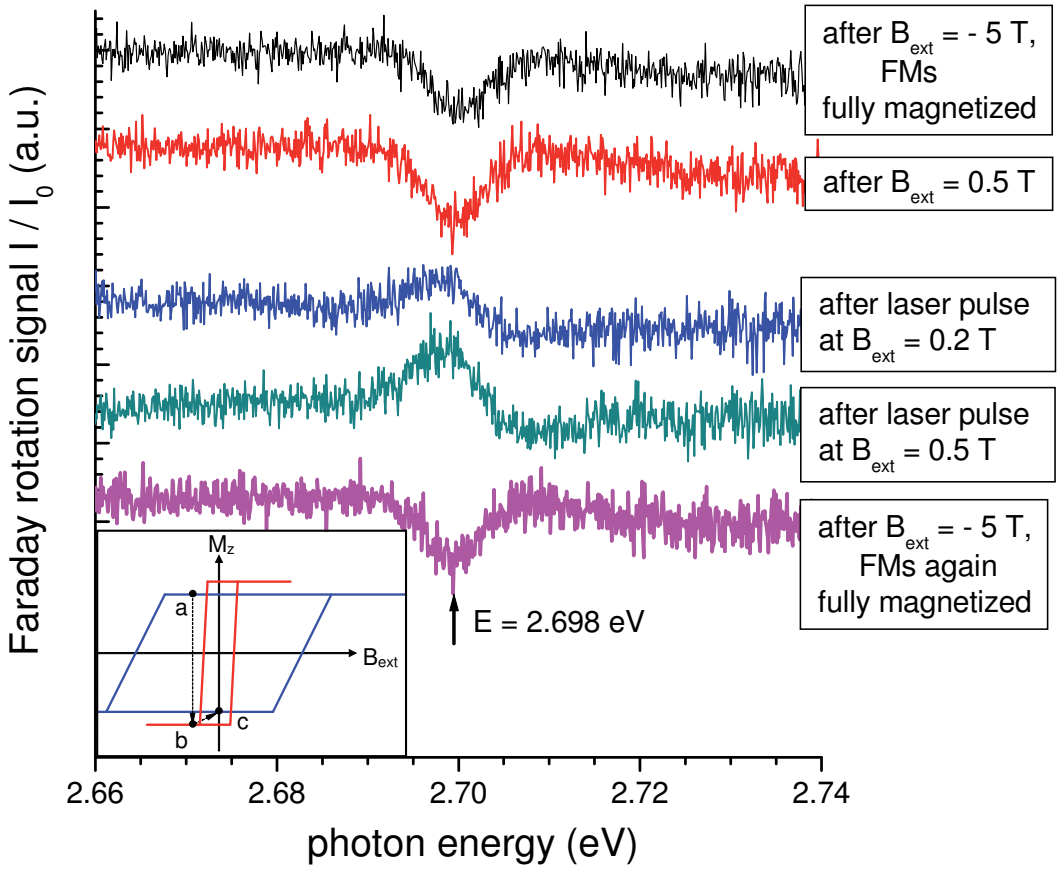


Figure 4.21: Reversal of FM magnetization via single laser pulse in biased field. The FR signals are shifted with distinguishable levels. The inset shows the narrowing magnetic hysteresis curve caused by single laser pulse.

## 4.5 Exchange interaction in ZnMnO

In this section, ZnO-based DMS epilayer samples are studied with respect to their magneto-optical properties, especially to determine the exchange integrals of $Zn_{1-x}Mn_xO$.

### 4.5.1 Reflection spectra of $Zn_{1-x}Mn_xO$

Reflectivity spectra for three epilayer samples with $x = 0$ (pure ZnO), 0.41%, and 0.78% are shown in figure 4.22(a) for zero magnetic field. To determine the exciton energies, the reflectivity spectra are fitted for the sample stack (see figure 3.5) with the expression

Dieses Werk ist copyrightgeschützt und darf in keiner Form vervielfältigt werden noch an Dritte weitergegeben werden.
Es gilt nur für den persönlichen Gebrauch.

$$
\begin{aligned}
r &= r_{01} + t_{01} \cdot t_{10} \cdot r_{12} \cdot \mathcal{A} \sum_{m=1}^{\infty} (r_{10} \cdot r_{12} \cdot \mathcal{A})^m \\
\text{with} \quad \mathcal{A} &= e^{-2\frac{4\pi \cdot \kappa}{\lambda} d} \cdot e^{\frac{2nd}{\lambda} \cdot 2\pi} ,
\end{aligned}
\tag{4.9}
$$

where $r_{ij}$ and $t_{ij}$ are reflection and transmission coefficient at the interface between medium $i$ and $j$, respectively. 0, 1, and 2 denote air, epilayer, and substrate, respectively. $d$ is the thickness of epilayers, $\lambda$ the wavelength.

The intensity reflection coefficient is expressed by $R = |r|^2 + \tilde{R}$, where $\tilde{R}$ accounts for the incoherently reflected light from the backside of substrate.

The complex refractive index $\tilde{n}(\omega) = n + i\kappa$ for the epilayers follows with $\tilde{n}(\omega) = \sqrt{\varepsilon(\omega)}$ from dielectric constant, which can be written for $\omega \approx \omega_j$ by [53]

$$
\varepsilon(\omega) = \varepsilon_b + \sum_{j=A,B} \frac{f_j}{\omega_j - \omega - i\frac{\gamma_j}{2}} \quad \text{(Lorentzian profile).} \tag{4.10}
$$

Here the two homogeneously broadened exciton resonances A and B are considered in combination with the background dielectric constant $\varepsilon_b$ for the contribution of all higher resonances. $f_j$ and $\gamma_j$ are oscillator strength and damping, respectively.

For the two $Zn_{1-x}Mn_xO$ epilayers, the additional disorder-induced broadening [82] is accounted by a combined homogeneous and inhomogeneous broadening using Voigt profiles for the exciton transitions [53]

$$
\begin{aligned}
\varepsilon(\omega) = \varepsilon_b + \sum_{j=A,B} \frac{f_j}{\sqrt{2\pi}\sigma_j} \{ & \int_0^{\infty} \frac{\omega' - \omega}{(\omega' - \omega)^2 + (\frac{\gamma_j}{2})^2} \cdot e^{-\frac{(\omega' - \omega_j)^2}{2\sigma_j^2}} d\omega' \\
& + \int_0^{\infty} \frac{i\frac{\gamma_j}{2}}{(\omega' - \omega)^2 + (\frac{\gamma_j}{2})^2} \cdot e^{-\frac{(\omega' - \omega_j)^2}{2\sigma_j^2}} d\omega' \} .
\end{aligned}
\tag{4.11}
$$

$\sigma_j$ is here the inhomogeneous broadening. Since localized exciton resonances are considered, the spatial dispersion [15] is not regarded here.

A- and B-exciton energies ($E_{X,A}$ and $E_{X,B}$) measured in ZnO ($x = 0$) have values close to those by Thomas [21] as seen in table 4.4.

Dieses Werk ist copyrightgeschützt und darf in keiner Form vervielfältigt werden noch an Dritte weitergegeben werden.
Es gilt nur für den persönlichen Gebrauch.

The Mn-concentration dependence of exciton energies is determined from figure 4.22(a) and drawn in figure 4.22(b). The constant splitting between A- and B-exciton resonance shows that $\Delta_{so}$ is keeping the same sign and value for the studied samples with $x \leq 0.01$.

Table 4.4: Exciton energies (eV) in ZnO

| | $E_{X,A}$ | $E_{X,B}$ | sample structure | measured spectra |
|---|---|---|---|---|
| Thomas [21] | 3.3770 | 3.3845 | single crystal | reflection |
| Reynolds *et al.* [31] | 3.3773 | 3.3895 | single crystal | PL |
| Pacuski *et al.* [15] | 3.3725 | 3.3792 | epilayers | reflection |
| this work | 3.3747 | 3.3824 | epilayers | reflection |

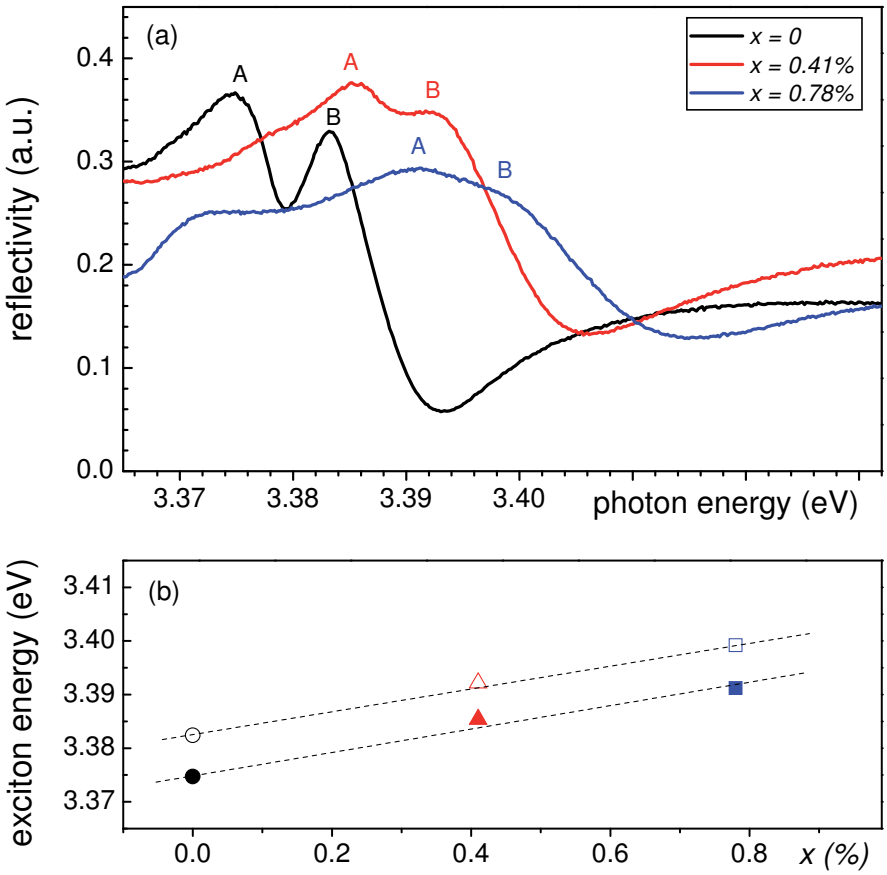


Figure 4.22: (a) Reflectivity spectra in the exciton range of $Zn_{1-x}Mn_xO$ epilayers at 1.5 K for zero magnetic field. Panel (b) presents the Mn concentration dependence of A- and B-exciton energies.

Dieses Werk ist copyrightgeschützt und darf in keiner Form vervielfältigt werden noch an Dritte weitergegeben werden.
Es gilt nur für den persönlichen Gebrauch.

### 4.5.2 Determination of s,p-d exchange constants of $Zn_{1-x}Mn_xO$

To determine the exchange interaction constants $N_0\alpha$ and $N_0\beta$ (or $N_0|\alpha - \beta|$) from reflectivity spectra, the $Zn_{1-x}Mn_xO$ epilayer with $x = 0.41\%$ is measured in magnetic field in Faraday geometry. The epilayer with $x = 0.78\%$ has already too large inhomogeneous broadening for this purpose. The field induced shift of $E_{X,A}$ and $E_{X,B}$ for $\sigma^-$ and $\sigma^+$ is marked with arrows schematically in figure 4.23(a). The magnetic-field dependent splitting of excitons is drawn in the panel of 4.23(b).

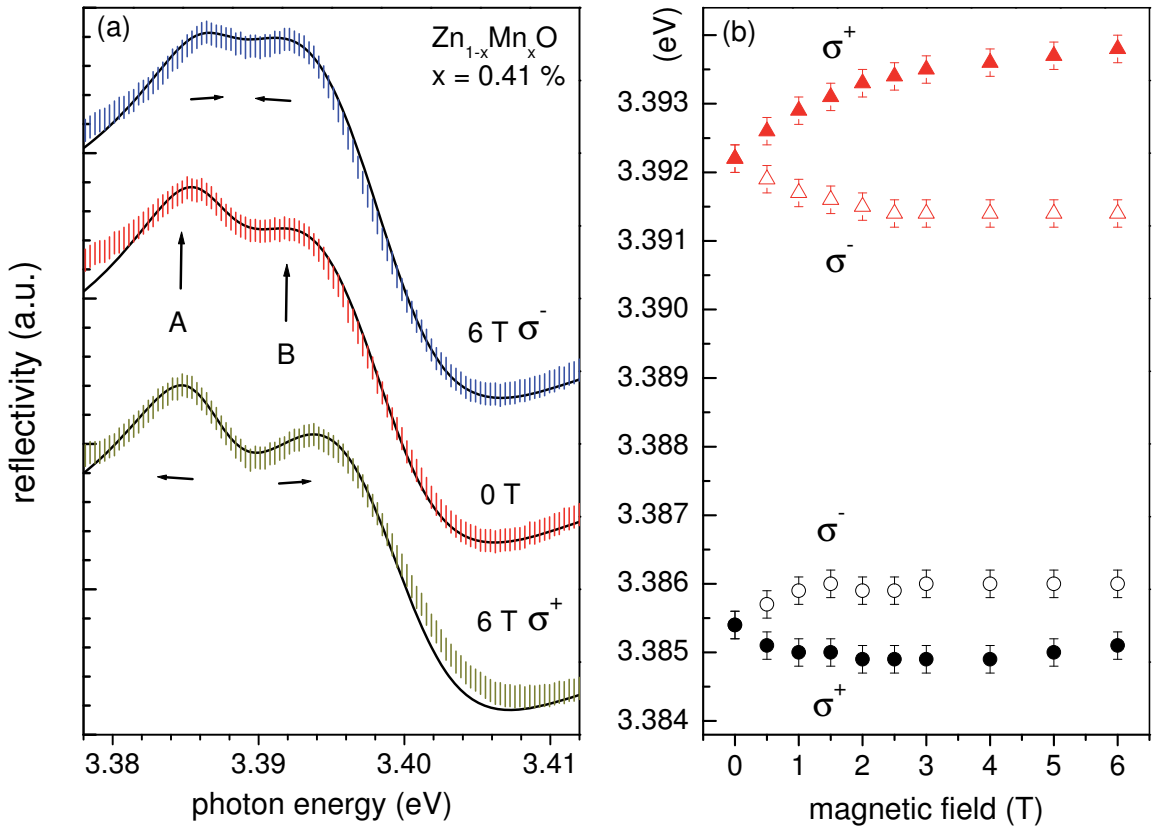


Figure 4.23: (a) Circularly polarized reflectivity spectra and fits (black solid curves) for epilayers at 0 and 6 T around A- and B-exciton transitions. (b) Derived A- (circle) and B-exciton (triangle) energies versus magnetic field for both polarizations.

According to figure 4.23(b), the splitting amounts only to 1 . . . 2 meV at 6 T. This splitting is very small compared with the observed giant Zeeman splitting of (Zn,Cd,Mn)Se/ZnSe QW samples. Therefore, it is necessary to include the usual Zeeman effect in the analysis here.

Dieses Werk ist copyrightgeschützt und darf in keiner Form vervielfältigt werden noch an Dritte weitergegeben werden.
Es gilt nur für den persönlichen Gebrauch.

The polarization of the A- and B-exciton components is opposite to the prediction in figure 2.10. This indicates that $N_0(\alpha-\beta)>0$ is not fulfilled in ZnMnO. The other possibility, that the sequence of $\Gamma_{7v}$ and $\Gamma_{9v}$ is reversed to the assumption in figure 2.10, is very improbable according to more recent studies on ZnO [28, 83] and the observation in figure 4.23(b). Furthermore, splitting of B-exciton is up to twice larger than that of A-exciton which contradicts also figure 2.10. A different splitting for A- and B-excitons could be possibly assigned to the electron-hole exchange interaction [15] $\Delta_{ehx} = (\Delta_{so}/2)\,\vec{\sigma_e}\cdot\vec{\sigma_h}$, which gives a mixing between the excitons coupling to the same circular polarization.

The giant Zeeman splitting can be calculated with the expressions

$$G_e = \pm\frac{x}{2}N_0\alpha S\mathcal{B}_S(\frac{\mu_B g_{Mn}SB}{k_B T_s}) \tag{4.12}$$

and

$$G_h = \pm\frac{x}{2}N_0\beta S\mathcal{B}_S(\frac{\mu_B g_{Mn}SB}{k_B T_s})\,, \tag{4.13}$$

where $G_e$ and $G_h$ are the shifts for electron (s-d interaction in CB) and hole (p-d interaction in VB), respectively. The signs "+" and "-" denote spin up and spin down for band electrons, respectively.

The usual Zeeman shift is given by

$$Z_{z,j} = \langle\sigma_{z,j}\rangle g_j\mu_B B\,, \tag{4.14}$$

where $j$ denotes $e$ (electron), $ah$ (A-hole), and $bh$ (B-hole), $\langle\sigma_{z,j}\rangle$ projection of total angular momentum in $z$-direction.

The diamagnetic shift can be neglected due to the small Bohr radius of ZnO [84]. At low temperature ($\approx 2K$), $\mathcal{B}_{5/2}(B)$ behaves linearly at $B \leq 1$ T and reaches saturation at $B = 6$ T.

Including electron-hole exchange interaction, the Hamiltonian $\mathbf{H_X}$ for the $\sigma^-$ and $\sigma^+$ polarized exciton components of A and B with bases $\begin{pmatrix}\alpha_e p^- \beta_{bh}\\ \beta_e p^- \alpha_{ah}\end{pmatrix}$

Dieses Werk ist copyrightgeschützt und darf in keiner Form vervielfältigt werden noch an Dritte weitergegeben werden.
Es gilt nur für den persönlichen Gebrauch.

and $\begin{pmatrix} \alpha_e p^+ \beta_{bh} \\ \beta_e p^+ \alpha_{ah} \end{pmatrix}$ is given by

$$\begin{bmatrix} E_0 + \Delta_{so} - (G_e - G_h) - (Z_{z,e} + Z_{z,ah}) & \Delta_{ehx} \\ \Delta_{ehx} & E_0 + (G_e - G_h) + (Z_{z,e} - Z_{z,bh}) \end{bmatrix}$$

and

$$\begin{bmatrix} E_0 + \Delta_{so} + (G_e - G_h) + (Z_{z,e} + Z_{z,ah}) & \Delta_{ehx} \\ \Delta_{ehx} & E_0 - (G_e - G_h) - (Z_{z,e} - Z_{z,bh}) \end{bmatrix},$$

respectively. The matrix elements are fitting parameters described by equations 4.12 to 4.14, whose values are listed with two sets in table 4.5. The diagonal part of electron-hole exchange contribution is included in $E_0$.

Table 4.5: The values of two set fitting parameters

| $\Delta_{so}$ | $E_0$ | $\Delta_{ehx}$ | $g_e$ | $g_{ah}$ | $g_{bh}$ | $N_0(\alpha - \beta)$ |
|---|---|---|---|---|---|---|
| -4.8 meV | 3391.2 meV | 2.5 meV | 1.96 | -1.4 | 2.0 | -0.25 eV |
| +4.8 meV | 3386.4 meV | 2.5 meV | 1.96 | 1.2 | 0.4 | +0.25 eV |

In table 4.5, the values of fit for exciton energies of figure 4.23(b) are given with spin-orbit coupling $\Delta_{so}$, the zero field energy of B-exciton $E_0$ with $\Gamma_{9v}$ hole, $g_e$, $g_{ah}$, and $g_{bh}$ effective Landé $g$-factors for electron in CB, A-hole, and B-hole in VB, respectively. The sign of the parameter $\Delta_{so}$ determines the valence band ordering.

For negative $\Delta_{so}$, the eigenvalues of $\mathbf{H_X}$ reveal the valence band ordering from the top with $\Gamma_{7_v}$, $\Gamma_{9_v}$ and $\Gamma_{7_v}$, which agrees with the order in work by Thomas [21]. Values of $g_{ah}$ and $g_{bh}$ derived here are comparable with the values suggested by Ref.[28]. The fitting curves are seen in figure 4.24.

The obtained modulus $N_0 \mid \alpha - \beta \mid = 0.25$ agrees fairly well with PL data measured on ZnMnO obtained from oxidation of $p$-doped ZnMnTe on GaAs substrate [16].

The fits agree fairly for $B = 1$ T but less for higher magnetic fields. The effect of $\Delta_{ehx}$ is seen for $B \geq 3$ T. $\Delta_{ehx}$ repulses mainly the $\sigma^-$-component of A-exciton from that of B-excitons. In higher magnetic field, $\Delta_{ehx}$ and the usual Zeeman splitting become more important.

Dieses Werk ist copyrightgeschützt und darf in keiner Form vervielfältigt werden noch an Dritte weitergegeben werden.
Es gilt nur für den persönlichen Gebrauch.

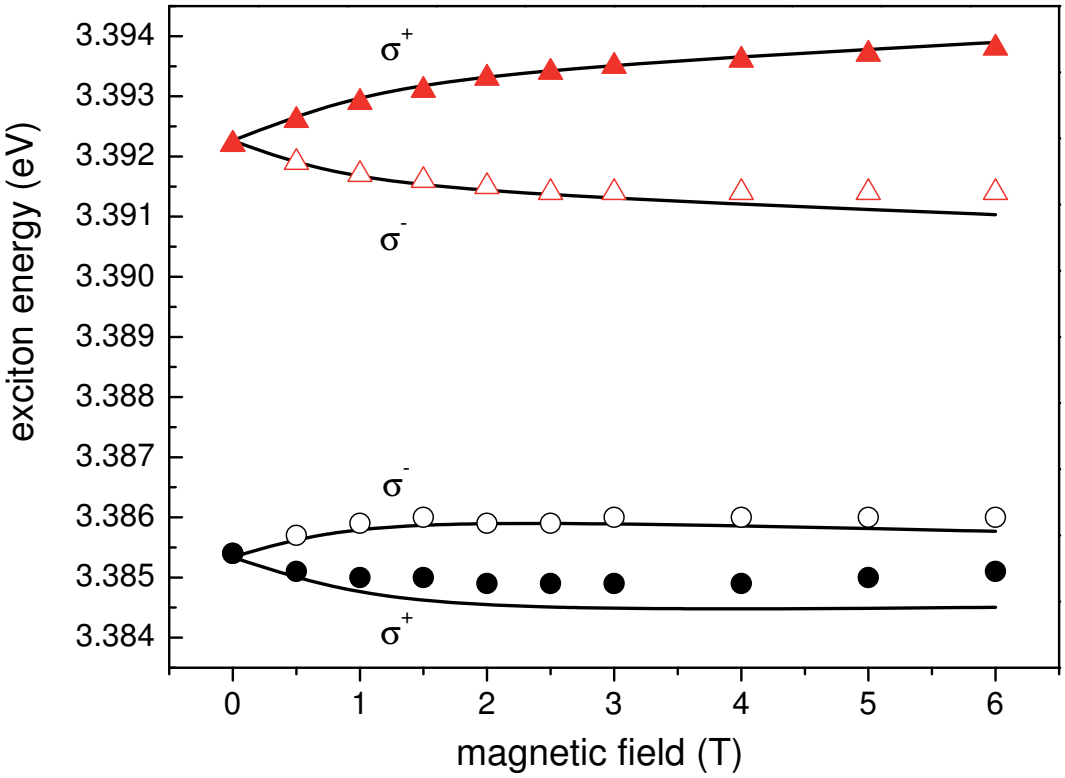


Figure 4.24: Fitting curves (solid lines) with negative $\Delta_{so}$ for excitons presented in figure 4.23(b).

$N_0\alpha$ with a value about 0.25 eV is regarded to have no dependence on host material [47]. $N_0\beta$ is derived then to be approximately 0.50 eV for $\Delta_{so} < 0$.

Considering the unlike case $\Delta_{so} > 0$ with the topmost valence band $\Gamma_{9_v}$, a nearly vanishing p-d interaction would follow ($N_0\beta \approx 0$).

Summarizing, it is found that ZnMnO is not appropriate for hybrid structures.

Dieses Werk ist copyrightgeschützt und darf in keiner Form vervielfältigt werden noch an Dritte weitergegeben werden.
Es gilt nur für den persönlichen Gebrauch.

# Bibliography


[1] Andrew Steane. Quantum computing. *Reports on Progress in Physics*, Volume 61, Number 2:117, 1998.

[2] D. D. Awschalom, D. Loss, and N. Samarth, editors. *Semiconductor Spintronics and Quantum Computation*. Springer, 2002.

[3] J. K. Furdyna and Jacek Kossut, editors. *Diluted Magnetic Semiconductors*. Academic Press, Boston, 1988.

[4] S. A. Wolf, D. D. Awschalom, R. A. Buhrman, J. M. Daughton, S. von Molnar, M. L. Roukes, A. Y. Chtchelkanova, and D. M. Treger. Spintronics: A spin-based electronics vision for the future. *Science*, 294(5546):1488–1495, 2001.

[5] R. Fiederling, M. Keim, G. Reuscher, W. Ossau, G. Schmidt, A. Waag, and L. W. Molenkamp. Injection and detection of a spin-polarized current in a light-emitting diode. *Nature*, 402(6763):787–790, December 1999.

[6] A. T. Hanbicki, B. T. Jonker, G. Itskos, G. Kioseoglou, and A. Petrou. Efficient electrical spin injection from a magnetic metal/tunnel barrier contact into a semiconductor. *Appl. Phys. Lett.*, 80(7):1240–1242, February 2002.

[7] X. Jiang, R. Wang, R. M. Shelby, R. M. Macfarlane, S. R. Bank, J. S. Harris, and S. S. P. Parkin. Highly spin-polarized room-temperature tunnel injector for semiconductor spintronics using MgO(100). *Phys. Rev. Lett.*, 94(5):056601–, February 2005.

[8] S. A. Crooker, M. Furis, X. Lou, C. Adelmann, D. L. Smith, C. J. Palmstrøm, and P. A. Crowell. Imaging spin transport in lateral ferromagnet/semiconductor structures. *Science*, 309(5744):2191–2195, 2005.




Dieses Werk ist copyrightgeschützt und darf in keiner Form vervielfältigt werden noch an Dritte weitergegeben werden.
Es gilt nur für den persönlichen Gebrauch.

[9] R. K. Kawakami, Y. Kato, M. Hanson, I. Malajovich, J. M. Stephens, E. Johnston-Halperin, G. Salis, A. C. Gossard, and D. D. Awschalom. Ferromagnetic imprinting of nuclear spins in semiconductors. *Science*, 294(5540):131–134, 2001.

[10] Gerrit E. W. Bauer, Arne Brataas, Yaroslav Tserkovnyak, Bertrand I. Halperin, Maciej Zwierzycki, and Paul J. Kelly. Dynamic ferromagnetic proximity effect in photoexcited semiconductors. *Phys. Rev. Lett.*, 92(12):126601–, March 2004.

[11] J. K. Furdyna. Diluted magnetic semiconductors. *J. Appl. Phys.*, 64(4):R29–R64, 1988.

[12] Jan A. Gaj, Jacek. Kossut, and SpringerLink (Online service). Introduction to the Physics of Diluted Magnetic Semiconductors, 2010.

[13] T. Dietl, H. Ohno, and F. Matsukura. Hole-mediated ferromagnetism in tetrahedrally coordinated semiconductors. *Phys. Rev. B*, 63(19):195205–, April 2001.

[14] Nicola A. Spaldin. Search for ferromagnetism in transition-metal-doped piezoelectric ZnO. *Phys. Rev. B*, 69(12):125201–, March 2004.

[15] W. Pacuski, D. Ferrand, J. Cibert, C. Deparis, J. A. Gaj, P. Kossacki, and C. Morhain. Effect of the s,p-d exchange interaction on the excitons in $Zn_{1-x}Co_xO$ epilayers. *Phys. Rev. B*, 73(3):035214–, January 2006.

[16] E. Przeździecka, E. Kamińska, M. Kiecana, M. Sawicki, Ł. Kłopotowski, W. Pacuski, and J. Kossut. Magneto-optical properties of the diluted magnetic semiconductor *p*-type ZnMnO. *Solid State Communications*, 139(10):541–544, September 2006.

[17] Arthur S. Nowick. *Crystal Properties via Group Theory*. Cambridge University Press, Cambridge; New York, 1995.

[18] H. Saito. *"ZnSe Semiconductors" in "Wide Bandgap Semiconductors and Related Optoelectronic Devices"*. by Kiyoshi Takahashi, Akihiko Yoshikawa, and Adarsh Sandhu, editors, Springer-Verlag Berlin Heidelberg, [New York], 2007.

[19] Peter Y. Yu and Manuel Cardona. *Fundamentals of Semiconductors : Physics and Materials Properties*. Springer, Berlin; New York, 1996.

Dieses Werk ist copyrightgeschützt und darf in keiner Form vervielfältigt werden noch an Dritte weitergegeben werden.
Es gilt nur für den persönlichen Gebrauch.

[20] Ü. Özgür, Ya. I. Alivov, C. Liu, A. Teke, M. A. Reshchikov, S. Doğan, V. Avrutin, S.-J. Cho, and H. Morkoç. A comprehensive review of ZnO materials and devices. *J. Appl. Phys.*, 98(4):041301–103, August 2005.

[21] D. G. Thomas. The exciton spectrum of zinc oxide. *Journal of Physics and Chemistry of Solids*, 15(1-2):86–96, August 1960.

[22] J. J. Hopfield. Fine structure in the optical absorption edge of anisotropic crystals. *Journal of Physics and Chemistry of Solids*, 15(1-2):97–107, August 1960.

[23] Marius Grundmann. *The Physics of Semiconductors : An introduction Including Devices and Nanophysics*. Springer, Berlin, 2006.

[24] A. Mang, K. Reimann, and St. Rübenacke. Band gaps, crystal-field splitting, spin-orbit coupling, and exciton binding energies in ZnO under hydrostatic pressure. *Solid State Communications*, 94(4):251–254, April 1995.

[25] L. C. Lew Yan Voon, M. Willatzen, M. Cardona, and N. E. Christensen. Terms linear in $k$ in the band structure of wurtzite-type semiconductors. *Physical Review B*, 53:10703–, 1996.

[26] J.E. Rowe, Manuel Cardona, and F.H. Pollak. Valence band symmetry and deformation potentials of ZnO. *Solid State Communications*, 6(4):239–242, April 1968.

[27] W. R. L. Lambrecht, S. Limpijumnong, and Segall B. Theoretical studies of ZnO and related $Mg_xZn_{1-x}O$ alloy band structure. In *MRS Internet J. Nitride Semicond. Res. 4S1, G6.8*, 1999.

[28] Walter R. L. Lambrecht, Anna V. Rodina, Sukit Limpijumnong, B. Segall, and Bruno K. Meyer. Valence-band ordering and magneto-optic exciton fine structure in ZnO. *Phys. Rev. B*, 65(7):075207–, January 2002.

[29] S. Fujita. *"ZnO Semiconductors" in "Wide Bandgap Semiconductors and Related Optoelectronic Devices"*. by Kiyoshi Takahashi, Akihiko Yoshikawa, and Adarsh Sandhu, editors, Springer-Verlag Berlin Heidelberg, [New York], 2007.

[30] D. W. Langer, R. N. Euwema, Koh Era, and Takao Koda. Spin exchange in excitons, the quasicubic model and deformation potentials in II-VI compounds. *Phys. Rev. B*, 2(10):4005–, November 1970.

Dieses Werk ist copyrightgeschützt und darf in keiner Form vervielfältigt werden noch an Dritte weitergegeben werden.
Es gilt nur für den persönlichen Gebrauch.

[31] D. C. Reynolds, D. C. Look, B. Jogai, C. W. Litton, G. Cantwell, and W. C. Harsch. Valence-band ordering in ZnO. *Phys. Rev. B*, 60(4):2340–, July 1999.

[32] Robert Laskowski and Niels Egede Christensen. Ab initio calculation of excitons in ZnO. *Phys. Rev. B*, 73(4):045201–, January 2006.

[33] N. B. Brandt and V. V. Moshchalkov. Semimagnetic semiconductors. *Advances in Physics*, 33(3):193–256, 1984.

[34] A. R. Denton and N. W. Ashcroft. Vegard's law. *Phys. Rev. A*, 43(6):3161–, March 1991.

[35] L. O. Lokot. Strain effect on the valence band structure, optical transitions, and light gain spectra in zinc-blende GaN quantum wells. *Semiconductor Physics, Quantum Electronics & Optoelectronics*, 11:364–369, 2008.

[36] H. J. Lozykowski and V. K. Shastri. Excitonic and Raman properties of ZnSe/$Zn_{1-x}Cd_xSe$ strained-layer quantum wells. *J. Appl. Phys.*, 69(5):3235–3242, March 1991.

[37] B. E. Larson, K. C. Hass, H. Ehrenreich, and A. E. Carlsson. Theory of exchange interactions and chemical trends in diluted magnetic semiconductors. *Phys. Rev. B*, 37(8):4137–, March 1988.

[38] B.E. Larson, K.C. Hass, H. Ehrenreich, and A.E. Carlsson. Exchange mechanisms in diluted magnetic semiconductors. *Solid State Communications*, 56(4):347–350, October 1985.

[39] A. Lewicki, J. Spalek, J. K. Furdyna, and R. R. Galazka. Magnetic susceptibility of diluted magnetic (semimagnetic) semiconductors: Further evidence for superexchange. *Phys. Rev. B*, 37(4):1860–, February 1988.

[40] T. M. Giebultowicz, J. J. Rhyne, and J. K. Furdyna. Mn-Mn exchange constants in zinc-manganese chalcogenides. *J. Appl. Phys.*, 61(8):3537–3539, April 1987.

[41] O. Goede and W. Heimbrodt. Optical properties of (Zn, Mn) and (Cd, Mn) chalcogenide mixed crystals and superlattices. *physica status solidi (b)*, 146(1):11–62, 1988.

[42] A. Twardowski. Magneto-optical study of $Zn_{1-x}Mn_xTe$ mixed crystals. *Physics Letters A*, 94(2):103–105, February 1983.

Dieses Werk ist copyrightgeschützt und darf in keiner Form vervielfältigt werden noch an Dritte weitergegeben werden.
Es gilt nur für den persönlichen Gebrauch.

[43] J. A. Gaj, R. Planel, and G. Fishman. Relation of magneto-optical properties of free excitons to spin alignment of $Mn^{2+}$ ions in $Cd_{1-x}Mn_xTe$. *Solid State Communications*, 29(5):435–438, February 1979.

[44] D. Keller, D. R. Yakovlev, B. König, W. Ossau, Th. Gruber, A. Waag, L. W. Molenkamp, and A. V. Scherbakov. Heating of the magnetic ion system in (Zn, Mn)Se/(Zn, Be)Se semimagnetic quantum wells by means of photoexcitation. *Phys. Rev. B*, 65(3):035313–, December 2001.

[45] M. K. Kneip, D. R. Yakovlev, M. Bayer, A. A. Maksimov, I. I. Tartakovskii, D. Keller, W. Ossau, L. W. Molenkamp, and A. Waag. Direct energy transfer from photocarriers to Mn-ion system in II-VI diluted-magnetic-semiconductor quantum wells. *Phys. Rev. B*, 73(3):035306–, January 2006.

[46] Grosso Giuseppe and Pastori Parravicini Giuseppe. *Solid State Physics*. Academic Press, San Diego, 2000.

[47] S. H. Liu. Exchange interaction between conduction electrons and magnetic shell electrons in rare-earth metals. *Phys. Rev.*, 121(2):451–, January 1961.

[48] A. Twardowski, M. von Ortenberg, M. Demianiuk, and R. Pauthenet. Magnetization and exchange constants in $Zn_{1-x}Mn_xSe$. *Solid State Communications*, 51(11):849–852, September 1984.

[49] Krishan K. Bajaj. Magneto-optical properties of quantum wells with arbitrary potential profiles. Technical Report A730232, ARIZONA STATE UNIV TEMPE, 15 AUG 1990.

[50] D. B. Tran Thoai, R. Zimmermann, M. Grundmann, and D. Bimberg. Image charges in semiconductor quantum wells: Effect on exciton binding energy. *Phys. Rev. B*, 42(9):5906–, September 1990.

[51] P. Peyla, R. Romestain, Y. Merle d'Aubigné, G. Fishman, A. Wasiela, and H. Mariette. Exciton *s* states in semiconductor quantum wells in a magnetic field. *Phys. Rev. B*, 52(16):12026–, October 1995.

[52] B. König, U. Zehnder, D. R. Yakovlev, W. Ossau, T. Gerhard, M. Keim, A. Waag, and G. Landwehr. Magneto-optical properties of $Zn_{0.95}Mn_{0.05}Se/Zn_{0.76}Be_{0.08}Mg_{0.16}Se$ quantum wells and $Zn_{0.91}Mn_{0.09}Se/Zn_{0.972}Be_{0.028}Se$ spin superlattices. *Phys. Rev. B*, 60(4):2653–, July 1999.

Dieses Werk ist copyrightgeschützt und darf in keiner Form vervielfältigt werden noch an Dritte weitergegeben werden.
Es gilt nur für den persönlichen Gebrauch.

[53] Claus Klingshirn. *Semiconductor Optics*. Springer, Berlin, 2nd edition, 2005.

[54] Mark Fox. *Optical Properties of Solids*. Oxford University Press, Oxford; New York, 2001.

[55] Otfried Madelung, editor. *Semiconductors : Data Handbook*. Springer, Berlin; New York, 2004.

[56] W. Van Roy, J. De Boeck, and G. Borghs. Optimization of the magnetic field of perpendicular ferromagnetic thin films for device applications. *Appl. Phys. Lett.*, 61(25):3056–3058, December 1992.

[57] F. Richomme, J. Teillet, A. Fnidiki, P. Auric, and Ph. Houdy. Experimental study of the structural and magnetic properties of Fe/Tb multilayers. *Phys. Rev. B*, 54(1):416–, July 1996.

[58] Katsuyoshi Takano, Miki Furuhata, Satoru Kobayashi, Hiroshi Sakurai, and Fumitake Itoh. Perpendicular magnetic properties of Fe/Tb multilayered films. *Journal of Magnetism and Magnetic Materials*, 240(1-3):565–567, February 2002.

[59] F. Yang and F. Pan. Influence of film structure on the perpendicular magnetic anisotropy in Fe/Tb multilayers. *Physica B: Condensed Matter*, 315(4):227–233, April 2002.

[60] H. Schömig, A. Forchel, S. Halm, G. Bacher, J. Puls, and F. Henneberger. Magnetic imprinting of submicron ferromagnetic wires on a diluted magnetic semiconductor quantum well. *Appl. Phys. Lett.*, 84(15):2826–2828, April 2004.

[61] Christian Brosseau. *Fundamentals of Polarized Light : A statistical Optics Approach*. Wiley, New York, 1998.

[62] Petros N. Argyres. Theory of the Faraday and Kerr effects in ferromagnetics. *Phys. Rev.*, 97(2):334–, January 1955.

[63] S. Hugonnard-Bruyère, C. Buss, F. Vouilloz, R. Frey, and C. Flytzanis. Faraday-rotation spectra of semimagnetic semiconductors. *Phys. Rev. B*, 50(4):2200–, July 1994.

[64] E. L. Ivchenko. *Optical Spectroscopy of Semiconductor Nanostructures*. Alpha Science, Harrow, U.K., 2005.

Dieses Werk ist copyrightgeschützt und darf in keiner Form vervielfältigt werden noch an Dritte weitergegeben werden.
Es gilt nur für den persönlichen Gebrauch.

[65] E. Runge, A. Schülzgen, F. Henneberger, and R. Zimmermann. Relaxation kinetics and photoluminescence lineshape of excitons in II-VI semiconductor quantum wells. *phys. stat. sol. (b)*, 188(1):547–555, 1995.

[66] M. Nawrocki, Yu. G. Rubo, J. P. Lascaray, and D. Coquillat. Suppression of the auger recombination due to spin polarization of excess carriers and $Mn^{2+}$ ions in the semimagnetic semiconductor $Cd_{0.95}Mn_{0.05}S$. *Phys. Rev. B*, 52(4):R2241–, July 1995.

[67] A. V. Chernenko, P. S. Dorozhkin, V. D. Kulakovskii, A. S. Brichkin, S. V. Ivanov, and A. A. Toropov. Auger recombination of excitons in semimagnetic quantum dot structure in a magnetic field. *Phys. Rev. B*, 72(4):045302–, July 2005.

[68] J. Gutowski, N. Presser, and G. Kudlek. Optical properties of ZnSe epilayers and films. *phys. stat. sol. (a)*, 120(1):11–59, 1990.

[69] W. Y. Yu, A. Twardowski, L. P. Fu, A. Petrou, and B. T. Jonker. Magnetoanisotropy in $Zn_{1-x}Mn_xSe$ strained epilayers. *Phys. Rev. B*, 51(15):9722–, April 1995.

[70] A. V. Koudinov, Yu. G. Kusrayev, and I. G. Aksyanov. Light-induced heating effects in semimagnetic quantum wells. *Phys. Rev. B*, 68(8):085315–, August 2003.

[71] A. Hundt, J. Puls, A. V. Akimov, Y. H. Fan, and F. Henneberger. Photocarrier-induced spin heating and spin-lattice relaxation in diluted magnetic Stranski-Krastanov quantum dots. *Phys. Rev. B*, 72(3):033304–, July 2005.

[72] S. Halm, G. Bacher, E. Schuster, W. Keune, M. Sperl, J. Puls, and F. Henneberger. Local spin manipulation in ferromagnet-semiconductor hybrids. *Appl. Phys. Lett.*, 90(5):051916–3, January 2007.

[73] S. Sadofev, S. Blumstengel, and F. Henneberger. Formation of CdSe quantum dots on homoepitaxial ZnSe. *Appl. Phys. Lett.*, 84(18):3678–3680, May 2004.

[74] Kiko Nakamura and Huzio Nakano. Faraday rotation in a DMS quantum well. *J. Phys. Soc. Jpn.*, 59:1154, 1990.

Dieses Werk ist copyrightgeschützt und darf in keiner Form vervielfältigt werden noch an Dritte weitergegeben werden.
Es gilt nur für den persönlichen Gebrauch.

[75] Simon Halm, Patric Erich Hohage, Ekaterina Neshataeva, Frank Seifert, Tilmar Kümmell, Ellen Schuster, Werner Keune, Matthias Sperl, Yang-Hsiung Fan, Joachim Puls, Fritz Henneberger, and Gerd Bacher. Incoherent and coherent spin manipulation in ferromagnet-dilute magnetic semiconductor hybrids. *physica status solidi (a)*, 204(1):191–201, 2007.

[76] Charles Kittel. *Einführung in die Festkörperphysik : mit 60 Tabellen und 134 Aufgaben, 12. Auflage*. R. Oldenbourg Verlag, München [u.a.], 1999.

[77] R. W. Hill, J. Cosier, D. A. Hukin, P. Wells, and P. C. Lanchester. The specific heat of terbium below 4 K. *Physics Letters A*, 49(2):101–102, August 1974.

[78] P. B. Johnson and R. W. Christy. Optical constants of transition metals: Ti, V, Cr, Mn, Fe, Co, Ni, and Pd. *Phys. Rev. B*, 9(12):5056–, Jun 1974.

[79] E. Beaurepaire, J.-C. Merle, A. Daunois, and J.-Y. Bigot. Ultrafast spin dynamics in ferromagnetic nickel. *Phys. Rev. Lett.*, 76(22):4250–, May 1996.

[80] B. Koopmans, M. van Kampen, J. T. Kohlhepp, and W. J. M. de Jonge. Ultrafast magneto-optics in nickel: Magnetism or optics? *Phys. Rev. Lett.*, 85(4):844–, July 2000.

[81] Y. S. Chen, S. Halm, E. Neshataeva, T. Kümmell, G. Bacher, M. Wiater, T. Wojtowicz, and G. Karczewski. Local control of spin polarization in a semiconductor by microscale current loops. *Appl. Phys. Lett.*, 93(14):141902–, October 2008.

[82] R. Zimmermann, F. Große, and E. Runge. Excitons in semiconductor nanostructures with disorder. *Pure Appl. Chem.*, 69:1179–1186, 1997.

[83] A. V. Rodina, M. Strassburg, M. Dworzak, U. Haboeck, A. Hoffmann, A. Zeuner, H. R. Alves, D. M. Hofmann, and B. K. Meyer. Magneto-optical properties of bound excitons in ZnO. *Phys. Rev. B*, 69(12):125206–, March 2004.

[84] G. Blattner, G. Kurtze, G. Schmieder, and C. Klingshirn. Influence of magnetic fields up to 20 T on excitons and polaritons in CdS and ZnO. *Phys. Rev. B*, 25(12):7413–, June 1982.

Dieses Werk ist copyrightgeschützt und darf in keiner Form vervielfältigt werden noch an Dritte weitergegeben werden.
Es gilt nur für den persönlichen Gebrauch.

# Danksagung

Herrn Professor Dr. F. Henneberger danke ich ganz herzlich für die Möglichkeit, in seiner Arbeitsgruppe dieses interessante Thema bearbeiten zu dürfen. Seine stete Unterstützung, Anregungen, Hilfbereitschaft und Verantwortung haben die Erstellung dieser Arbeit ermöglicht.

Insbesondere bedanke ich mich bei meinem Betreuer Herrn Dr. J. Puls für die zahlreichen Diskussionen, Hinweise und das kritische Lesen des Manuskripts.

Mein Dank gilt auch den Mitarbeitern der Arbeitsgruppe „Physikalische Grundlagen der Photonik“, die mir währen dieser Arbeit geholfen haben. Herrn Dr. S. Sadofev danke ich sehr für die Herstellung der Proben und die Zusammenarbeit in der gemeinsamen Zeit. Dr. I. Dudeck und Frau D. Fahnauer danke ich für die Hilfe in Elektronik-Rechenbereich und Feinmechanik. Auf administrativer Seite danke ich Frau B. Matthes vielmals für die Hilfe. Den ehemaligen Kollegen, Herrn Dr. A. Hundt und Herrn Dr. I. Akimov bin ich sehr dankbar für die tatkräftige experimentelle Unterstützung.

Weiter bedanke ich mich bei Herrn Dr. U. Preppernau und Herrn V. Misch herzlich für die Versorgung des flüssigen Helium. Ohne die Großzügigkeit von den wäre die Messung nicht glatt verlaufen. Herrn Dr. S. Rogaschewski danke ich für die Röntgenuntersuchung an Proben.

Zum Schluß bin ich meiner Familie für das Verständis und die langjährige Unterstützung sehr dankbar. Speziell danke ich meiner lieben Frau Dr. N.-N. Liu, die mich bei dieser Arbeit ständig bestärkt und motivierend begleitet hat.



Dieses Werk ist copyrightgeschützt und darf in keiner Form vervielfältigt werden noch an Dritte weitergegeben werden.
Es gilt nur für den persönlichen Gebrauch.

Dieses Werk ist copyrightgeschützt und darf in keiner Form vervielfältigt werden noch an Dritte weitergegeben werden.
Es gilt nur für den persönlichen Gebrauch.

# Selbständigkeitserklärung

Hiermit erkläre ich, die vorliegende Arbeit selbständig ohne fremde Hilfe verfasst zu haben und nur die angegebene Literatur und Hilfsmittel verwendet zu haben.

Ich habe mich anderwärts nicht um einen Doktorgrad beworben und besitze einen entsprechenden Doktorgrad nicht.

Ich erkläre die Kenntnisnahme der dem Verfahren zugrunde liegenden Promotionsordnung der Mathematisch-Naturwissenschaftlichen Fakultät I der Humboldt-Universität zu Berlin.

Berlin, den 11. Juli 2011 Yang-Hsiung Fan



Dieses Werk ist copyrightgeschützt und darf in keiner Form vervielfältigt werden noch an Dritte weitergegeben werden.
Es gilt nur für den persönlichen Gebrauch.

Dieses Werk ist copyrightgeschützt und darf in keiner Form vervielfältigt werden noch an Dritte weitergegeben werden.
Es gilt nur für den persönlichen Gebrauch.

Dieses Werk ist copyrightgeschützt und darf in keiner Form vervielfältigt werden noch an Dritte weitergegeben werden.
Es gilt nur für den persönlichen Gebrauch.

Dieses Werk ist copyrightgeschützt und darf in keiner Form vervielfältigt werden noch an Dritte weitergegeben werden.
Es gilt nur für den persönlichen Gebrauch.